UNIVERSITÀ DEGLI STUDI DI ROMA
"TOR VERGATA"

Facoltà di Scienze Matematiche, Fisiche e Naturali

Dipartimento di Fisica

Dottorato in Fisica - XXIV ciclo

# The High Energy Tagger detector for the study of $\gamma\gamma$ physics at KLOE-2

Tutore:
Prof. ROBERTO MESSI

Candidato:
FRANCESCO GONNELLA

Coordinatore:
Prof. PIERGIORGIO PICOZZA

ANNO ACCADEMICO 2010-2011

*ad Agata e Stella*

# Summary

After the recent luminosity upgrade performed on DAΦNE accelerator complex, a new data taking campaign has been approved for the KLOE detector. One of the most significant features, characterising this new project called KLOE-2, is the presence of new small angle tagging detectors, referred to as the Low and the High Energy Tagger, that will allow the study of $\gamma\gamma$ physics.

The main purpose of this thesis is the description of all the work that has been done in order to design and realise the High Energy Tagger detector, together with all the needed electronics. Moreover to illustrate all the significant physics results that can be achieved with such a tagging detector in the framework of the upgraded DAΦNE.

I participated to this project from the very beginning, when nothing more that some preliminary simulation results and some sketches of the detector existed. At the beginning I was committed to simulation work. I implemented a new version of the Courau's Monte Carlo event generator that could be interfaced with the tracking software (`BDSIM`). I compared the results obtained with this code with the ones obtained with other codes, getting a fine agreement. Thanks to this work, the tracking of particles along DAΦNE lattice could be performed, allowing us to find the optimal location for the tagging detector and to properly design it. After the detector design was completed, I concentrated my work on designing all the electronic chain, which is composed of 3 boards: the front-end electronics, the discriminator, and the data acquisition board. At last I carried out all the tests needed in order to check the proper functioning of all the boards, obtaining good results. In particular the acquisition board operates perfectly: it communicates over the VMEbus according to the 2eVME64x standard, and yields the expected time resolution.

In the following an overview of this thesis is given.
The first chapter starts with an essential introduction on two-photon physics, that underlines its more intriguing implications. Then a basic description of DAΦNE accelerator complex and KLOE detector is given, focusing on all those aspects needed to a complete understanding of the tagging system and in particular of the High Energy Tagger. The chapter ends with an overview of all the other upgrades carried out on the KLOE detector, during the phases of the KLOE-2 programme.

The study of two-photon physics at DAΦNE collider is discussed in the second chapter, stressing the importance of having a lepton tagging system to disentangle $\gamma\gamma$ events. Significant physics processes, that can be studied within the upgraded DAΦNE framework, are taken into exam and the results obtained by our feasibility studies are reported.

In order to find the optimal location for the new tagging detectors, a detailed simulation has been performed. The results of this work are described in most of the third chapter. The study of background events on the High Energy Tagger, coming from radiative Bhabha scattering, is finally reported. From the results of this study, it is apparent that alternative trigger strategies, described in the last section, would result very helpful.

Chapter four is a detailed description of the High Energy Tagger detector. Dimensions, positioning and characteristics of scintillators and photomultipliers are reported. At the end of the chapter, the test performed at DAΦNE beam test facility on the sensitive area of the detector is described.

The most demanding part of this work, is doubtless the design and realisation of the whole electronic chain of the High Energy Tagger detector. In the fifth chapter all the electronic boards are described, with particular focus on the *data acquisition board* being the outstanding element of the electronic chain. At the end of the chapter, all the test performed on the boards are discussed in detail.

Finally, the conclusions of this work are drawn.

# Contents

# Chapter 1

# Introduction

## 1.1 Light interacting with light

`When one considers the extreme speed with which light spreads on every side, and how, when it comes from different regions, even from those directly opposite, the rays traverse one another without hindrance, one may well understand that when we see a luminous object, it cannot be by any transport of matter coming to us from this object, in the way in which a shot or an arrow traverses the air.`
*Traité de la lumière - Christiaan Huygens - 1690*

Can light interact with light?
Back in 1690, Huygens stated that the answer to this question was no. He was right, if we take into account classical electrodynamics alone, according to which electromagnetic waves pass through each other without any interference.
Nowadays, we know, from Quantum Electro Dynamics (QED), that photons cannot couple directly to each other, since they don't carry charge, but

they can interact through higher order processes: a photon can, within the bounds of the uncertainty principle, fluctuate into a charged pair of fermion and anti-fermion (lepton or quark), to either of which the other photon can couple.
All this kind of processes are referred to as two-photon physics or $\gamma\gamma$ *physics*. The relative "abundance" of these particles "inside" the photon at different interaction energies is often referred to as the photon *structure*.
According to quantum mechanics, a photon can be expressed as the following linear combination:

$$\mid A\rangle = a_1 \mid \gamma\rangle + a_2 \mid l\bar{l}\rangle + a_3 \mid q\bar{q}\rangle \tag{1.1}$$

What causes a photon to interact with another, described by coefficients $a'_n$, are the terms:

$$a_1 a'_1, \quad a_1 a'_2, \quad a_1 a'_3, \quad \ldots \tag{1.2}$$

The first term accounts for the classical interference of electromagnetic waves, thus it does not give rise to any interaction. The other two terms correspond to the production of leptons and quarks in the final state $X$ (see Fig: 1.1). $\gamma\gamma$ physics is very peculiar with respect to other kind of processes [1] (e.g. $e^+e^-$, $pp$ or $p\bar{p}$), here is presented a list of its main characteristics:

- It is a pure quantum effect i.e. it has no classical analogue. It can be compared with muon or electron anomalous magnetic dipole moment;
- The initial state has a well defined positive $C$-parity[1];
- Masses and the helicities in the initial state are well defined by kinematic variables;
- In contrast to hadron scattering, the initial state is "simple"; on the other hand the region of $Q^2$ in which most of the measurements have been performed is such that vector meson production dominates the initial state and the photon acts as if it were a hadron.

[1]This is true both for virtual and real photons in the initial state. In case of real photons, the angular momentum $J$ is bound to be 0 or 2. Thus for the initial state we have: $J^{PC} = 0^{\pm+}, \quad 2^{\pm+}$.

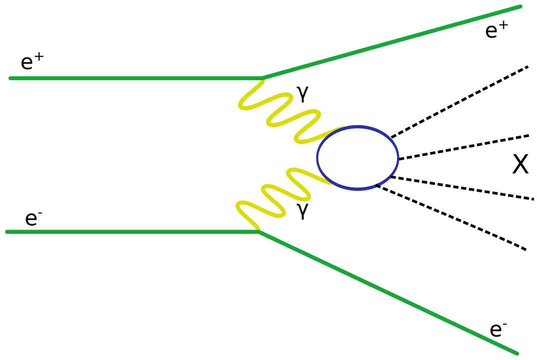


***Figure 1.1:*** *A simple diagram representing a $\gamma\gamma$ interaction at an $e^+e^-$ collider. Both the $e^-$ and the $e^+$ emit a photon. The combination of these photons leads to the creation of particles in a final state X.*

How likely is it to observe such a phenomenon in nature?
The cross-section of photon-photon scattering of visible light is phenomenally small and cannot be measured experimentally. But photons with higher energies can interact with each other more likely.
So where to find high energy photons interacting with each other?

An ideal environment for the study of $\gamma\gamma$ physics are electron-positron ($e^+e^-$) colliders. Although they have not been designed to study these processes, in such machines high energy photons are produced copiously and can very likely interact with each other. The decay products of the particles created in the final state can be studied within the detectors located at the the interaction point.
We said that $\gamma\gamma$ processes are "very likely" but, as a matter of fact, in the MeV energy range they are overwhelmed by the annihilation reaction.
While the cross-section of annihilation decreases as the center-of-mass energy, the cross-section of the photon scattering rises logarithmically. In this way from an energy of the order of GeV on, $\gamma\gamma$ physics starts to dominate.
When such a scattering process takes place, the electrons that emitted the photons get scattered out of their trajectory. The technique of detecting the electrons in the final state, in order to disentangle $\gamma\gamma$ events, is referred to as *tagging*.

## 1.2 DAΦNE collider and KLOE apparatus

In this section, we will briefly describe DAΦNE accelerator complex itself and on the KLOE apparatus, trying to stress as much as possible the aspects that are relevant for the scope of this thesis. In particular we are interested in the DAΦNE magnetic layout because it is critical for the tracking of leptons up to the tagging system, described in chapter 3, and in the structure of particle bunches circulating in the rings, which is critical for the acquisition system described in section 5.2.
As far as the KLOE apparatus is concerned, we are interested in the KLOE electromagnetic calorimeter, because it will detect the photons in the final state of the $\gamma\gamma$ processes we want to study, examined in sections 2.3 and 2.4. Finally we will describe the trigger system, because it affects the measurement we want to perform, which is analysed in chapter 2.
Chapter 2 is entirely dedicated to the description of the study of $\gamma\gamma$ physics that is going to be performed at DAΦNE collider by the KLOE-2 collaboration.

### 1.2.1 Double Annular $\phi$-factory for Nice Experiments

DAΦNE[2] is an accelerator complex (see Fig. 1.2) at Laboratori Nazionali di Frascati INFN, in the pleasant town of Frascati (Rome). It consists of a double ring collider and an injection system.
As suggested by its name, DAΦNE is a factory of $\phi$-mesons, i.e. its energy in the centre of mass is tuned on the value $m_\phi \simeq 1020\,\mathrm{MeV}$.
The original configuration of the collider was made of two independent 97 m rings, sharing two 10 m long interaction regions where several detectors have been installed. A linear accelerator (linac), two 180 m long transfer lines, an accumulator and damping ring, provide fast and high efficiency 510 MeV positron and electron acceleration and injection.
A list of DAΦNE main characteristics is reported in table 1.1.
Back in 2001 DAΦNE began steady operations and provided $4.4\,\mathrm{fb}^{-1}$ total

[2] Double Annular $\phi$-factory for Nice Experiments

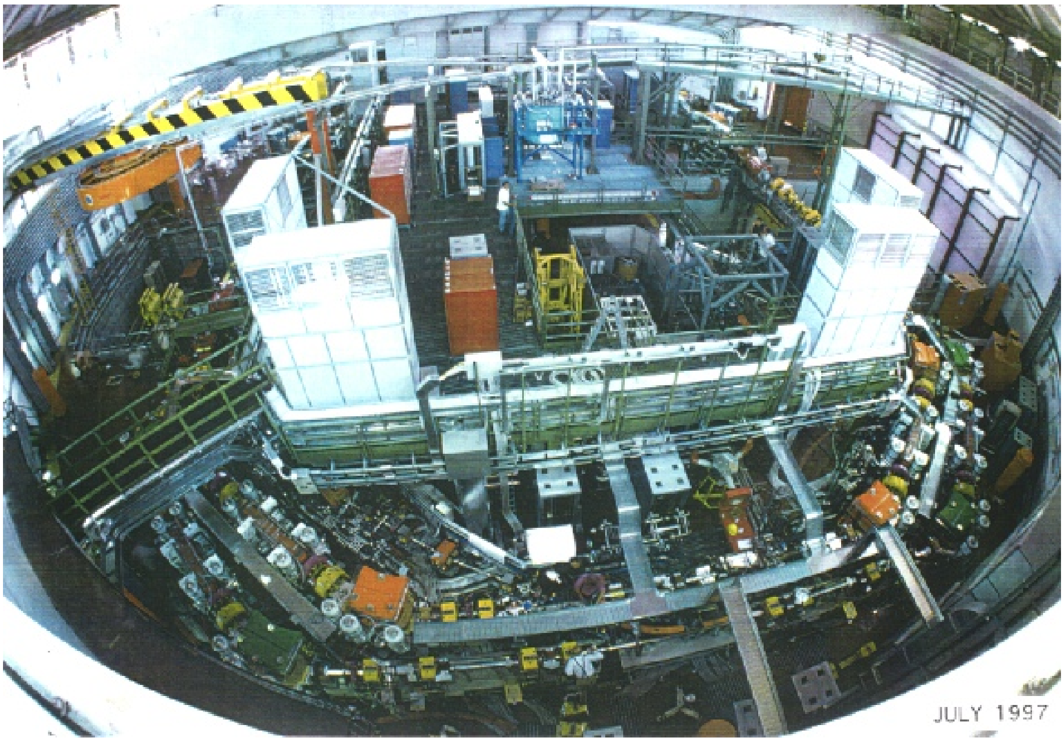


*Figure 1.2:* *A picture of DAΦNE hall.*

| | |
|---|---|
| **Single beam energy** | 510 MeV |
| **Particles per bunch** | $8.9 \times 10^{10}$ |
| **Bunches per ring** | up to 120 |
| **Bunch length** | 30 mm r.m.s. |
| **Horizontal beam size at crossing** | 2.0 mm r.m.s. |
| **Vertical beam size at crossing** | 0.02 mm r.m.s. |
| **Maximum stored current per ring** | 5.2 A |

*Table 1.1:* *Main DAΦNE parameters.*

integrated luminosity in dedicated runs, to the experiments KLOE, FINUDA, and DEAR for the following seven years.

Thanks to the collider performances, the KLOE experimental programme

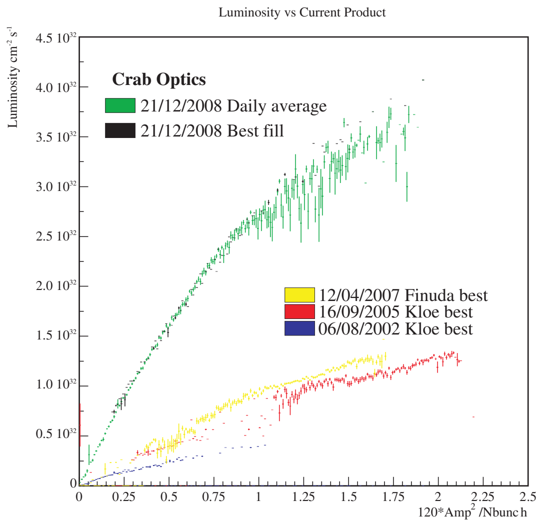


***Figure 1.3:*** *DAΦNE luminosity achievements plotted against the product of the beam currents. An improvement of a factor $\sim 4$ can be observed at the same beam currents as in the past.*

was completed in 2006, collecting about $3.0\,\mathrm{fb}^{-1}$.
At the beginning of 2007, DAΦNE reached a peak luminosity of $1.6 \times 10^{32}\,\mathrm{cm}^{-2}\mathrm{s}^{-1}$ and a daily integrated luminosity of about $10\,\mathrm{pb}^{-1}$.

### DAΦNE luminosity upgrade

In late 2007, a new collision scheme was implemented on DAΦNE[2]. Thanks to smaller beam sizes at the collision point and the suppression of beam-beam resonances, this new scheme is, in principle, capable of boosting the luminosity towards the value of $5 \times 10^{32}\,\mathrm{cm}^{-2}\mathrm{s}^{-1}$.
The constituents of the new configuration are mainly:

- A large crossing angle 50.3 mrad;
- Crab-Waist collisions.

Crab-Waist collisions are achieved by means of two sextupole magnets installed symmetrically with respect to the interaction point. They focus the

| Parameter | KLOE | FINUDA | SIDDHARTA |
|---|---|---|---|
| Date | September 2005 | April 2007 | June 2009 |
| Luminosity ($cm^{-2}s^{-1}$) | $1.53 \times 10^{32}$ | $1.60 \times 10^{32}$ | $4.53 \times 10^{32}$ |
| $e^-$current (A) | 1.38 | 1.50 | 1.52 |
| $e^+$current (A) | 1.18 | 1.10 | 1.00 |
| Number of bunches | 111 | 106 | 105 |
| $\epsilon_x$ (mm mrad) | 0.34 | 0.34 | 0.25 |
| $\beta_x$ (m) | 1.5 | 2.0 | 0.25 |
| $\beta_y$ (cm) | 1.8 | 1.9 | 0.93 |
| Bunch length,$\sigma_z$ (cm) | 1.5-2.0 | 1.5-2.0 | 1.5-2.0 |
| Crossing angle (mrad) | $2 \times 12.5$ | $2 \times 12.5$ | $2 \times 25$ |

***Table 1.2:*** *DAΦNE Luminosity and Interaction Point parameters for the three experiments. For a detailed description see reference [2].*

beam throughout the overlap region and suppress beam-beam resonances. This new scheme has been used to deliver beam-beam events to the SIDDHARTA experiment. The SIDDHARTA apparatus has provided an ideal environment for the Crab-Waist test, without a solenoidal magnetic field.
In this environment, striking results have been obtained (see Table 1.2 and Fig. 1.3). The luminosity grew by a factor 3, and its peak reached the value of $4.53 \times 10^{32}\,cm^{-2}s^{-1}$. In a slight injection regime, suitable for SIDDHARTA, the integrated daily luminosity has been almost 15 $pb^{-1}$. A nearly continuous injection regime, on the other hand, delivered an hourly integrated luminosity of 1.0 $pb^{-1}$. This means that a monthly integrated luminosity would be of a few less than 1.0 $fb^{-1}$ for the upgraded KLOE experiment, called KLOE-2.

### DAΦNE optics

As we said, the configuration of DAΦNE magnets has been changed in order to test Crab-Waist collision within the SIDDHARTA experiment. The same scheme is going to be adopted to deliver events to the KLOE apparatus. In order to do that, the magnetic layout has been slightly modified, especially because of the presence of KLOE magnetic field that needs other compensator to be placed on the machine lattice.

In this section we will briefly describe the present magnetic layout from

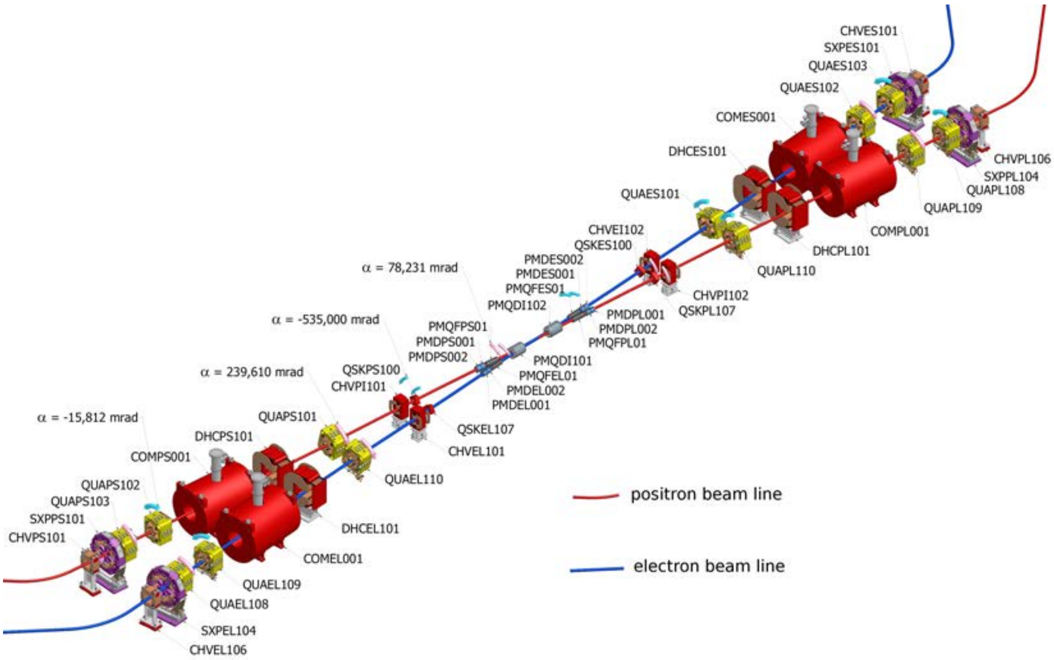


*Figure 1.4: DAΦNE magnets surrounding the interaction point.*

the interaction point (IP) up to the first bending dipole.

In figure 1.4 a drawing of the positron and electron lines is reported.

Magnets are placed simmetrically with respect to the IP, so it is enough to describe only half of one of the two lines, for instance the half of the positron beam-line (bottom left in the figure).

Starting from the IP up to the bending dipole magnet (not reported in figure), particles cross the magnets reported in table 1.3.

| | Magnet ID | Description |
|---|---|---|
| 1 | PMQDI101 | permanent magnet defocusing[3] quadrupole, common for both $e^+$ and $e^-$ lines |
| 2 | PMQFPS01 | permanent magnet focusing quadrupole |
| 3 | PMDPS001 | permanent compensator magnet |
| 4 | PMDPS002 | permanent compensator magnet |
| 5 | QSKPS100 | 45° quadrupole |
| 6 | CHVPI101 | kicker dipole |
| 7 | QUAPS101 | quadrupole |
| 8 | DHCPS101 | kicker dipole |
| 9 | COMPS001 | a cryogenic solenoidal compensator |
| 10 | QUAPS102 | quadrupole |
| 11 | QUAPS103 | quadrupole |
| 12 | SXPPS101 | Crab-Waist sextupole |
| 13 | CHVPS101 | kicker dipole |

***Table 1.3:*** *List of DAΦNE magnets from the interaction point up to the entrance of the first bending dipole.*

Magnets going from item number 1 to item number 3 in Tab. 1.3, are placed inside the volume of the KLOE apparatus, hence inside KLOE magnetic field. For this reason they must be permanent magnets and cannot be tuned during online operations.

The first defocusing quadrupole (1) is used to split horizontally the two beam-lines and send them into the respective beam-pipe. The following focusing quadrupole (2) straightens the previously bent beam trajectory.

Then a set of permanent dipoles (3, 4) is used as a compensator for the KLOE magnetic field that, vertically bends particle trajectories, because of the beam crossing angle.

After this set of permanent magnets, KLOE magnetic field ends pretty sharply. The fringe of the field bends the particle vertically, in the same direction as

the magnets, but in the opposite sense, acting as a sort of compensator.
The following two magnets (a rotated quadrupole (5) and a kicker dipole (6)) are used to slightly move the beam trajectories and finely centre the collision at the IP.
The trajectory of the particle, up to this point, is still out of the orbit plane, because of the vertical bending due to: KLOE magnetic field, compensators and KLOE magnetic field fringe effect. After a simple focusing quadrupole (7), the kicker dipole (8) is used to move the trajectory back to the plane of the orbit.
The cryogenic solenoidal magnet (9) (together with its twin on the other side of KLOE) is used to compensate the longitudinal effect of KLOE magnetic field. If a particle crosses the magnetic field along its axis, the Lorentz force is zero, thus there is no effect to compensate. But bunches are composed of many particles, which are not perfectly aligned. For these particles, the integral of the magnetic field is set to zero, in every revolution, by these solenoidal compensators.
After a set of two quadrupole magnets (10, 11), used to focus the beam, the Crab-Waist sextupole (12) is placed. After that, a kicker magnet (13) is used to push the particles on the proper trajectory before entering the main bending dipole, that was moved slightly because of the new configuration.

### DAΦNE particle bunch structure

For the purpose of this thesis, the time structure of particles stored in the DAΦNE rings is critical is worth to be discussed in detail.
As we have shown before (see Tab. 1.1), up to 120 bunches of electrons and 120 bunches of positrons can be stored in the DAΦNE rings. In the case of a completely filled ring, each bunch travels 2.7 ns apart from the next one.
Often the rings are not completely filled and some bunches are not present. When this happens, the bunches are not equally redistributed in space and in time, and some *slots* remain empty.
In other words, there are always 120 slots in each DAΦNE rings, each of which is 2.7 ns apart from the next one. Each slot can be filled or empty (see the scheme in Fig. 1.5).
In most of the cases, only 100 slots over 120 are filled.

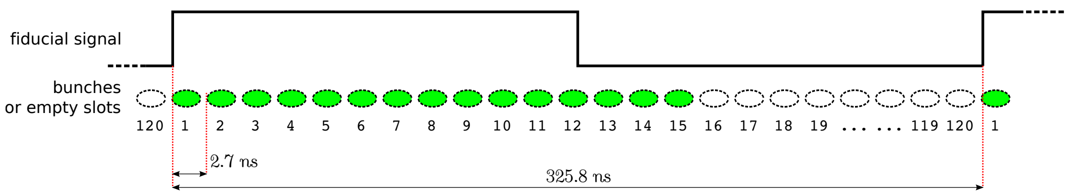


***Figure 1.5:*** *A scheme of DAΦNE particle bunch structure, drawn with respect to the fiducial signal.*

The bunches stored in the two rings are synchronised in such a way that the $n^{th}$ bunch in positron line crosses the IP at the same time of the $n^{th}$ bunch in electron line.
In order to properly number the bunches a signal, referred to as *fiducial*, is provided by DAΦNE machine. The fiducial signal is synchronous with the timing of the first injected bunch in the ring and has a period of 325.8 ns.
The KLOE acquisition system is synchronised with this signal (at the $T1$ trigger level, see section 1.2.3).

### 1.2.2 The KLOE detector

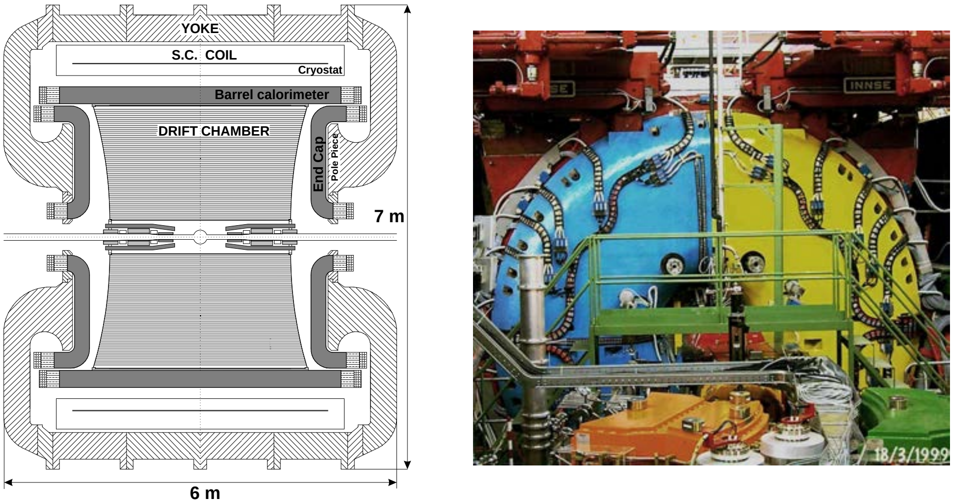


***Figure 1.6:*** *A scheme (left) and picture (right) of the KLOE detector.*

The main task of the KLOE[4] detector is the study of the decay products of $\phi$-mesons, mainly charged and neutral mesons like kaons (to which the experiment owes its name) and pions.
A hermetic electromagnetic calorimeter (EmC) and a magnetic spectrometer are the main elements of the detector. The spectrometer is composed of a large drift chamber (DC), for the tracking of charged particles, and a solenoidal magnetic field of nearly 0.5 T permeating the whole detector, generated by a superconducting coil surrounded by an iron yoke. The KLOE apparatus is sketched in Fig 1.6.
In order to minimise the multiple scattering and the energy loss of the charged particles, at the interaction point (IP), the beam pipe is made of beryllium and shaped as a sphere (radius: 10 cm and thickness: 0.5 mm).
A set of quadrupole magnets is placed inside the inner cylinder of the DC, close to the interaction region. They will be covered by the new QCALT calorimeters, in order to improve the acceptance of photons coming both from the IP and from any location in the volume of the DC. Further upgrades, described in section 1.3.2, are going to be performed in the so-called

[4]KLOE acronym stands for $K_L$ experiment.

"STEP-1" of the KLOE-2 programme.

### The electromagnetic calorimeter

The KLOE electromagnetic calorimeter (EmC) is a very fine sampling lead-scintillating fibre detector. It consists of a barrel and two end-cap calorimeters. The barrel is a cylinder with an inner diameter of 4 m, made of 24 modules, in which the fibres run parallel to the beam line.

Each end-cap is made of 32 C-shaped modules with fibres running perpen-

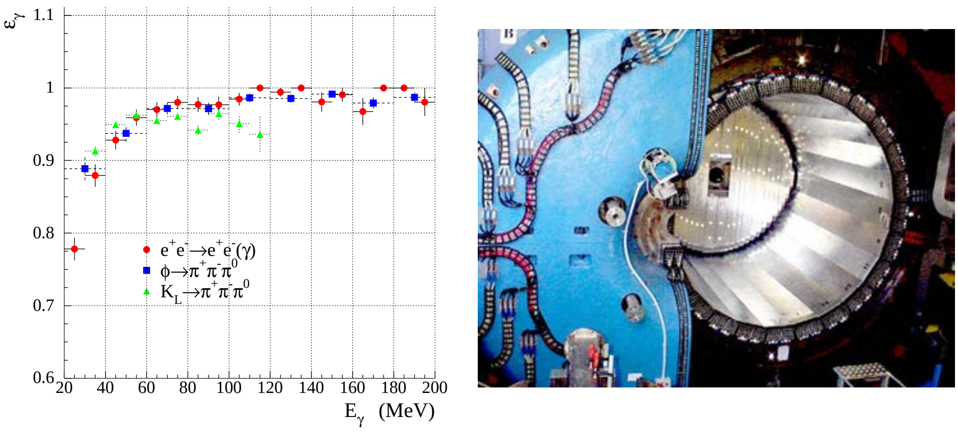


*Figure 1.7: Left panel: the photon detection efficiency of KLOE EmC is plotted against the energy of the photon. Right: a picture of the barrel section of KLOE EmC taken before the insertion of the drift chamber.*

dicular to the beam line. This structure covers 98% of the full solid angle. The composite of each module is a mixture of lead (48% of the volume), scintillating fibres (42%), and glue (10%), for an average density of 5 g/cm$^3$, a radiation length of about 1.5 cm, and an overall thickness of the calorimeter of about 15 radiation lengths. The passive material consists of 0.5 mm thick lead foils, which are alternated to layers of scintillating fibres, the active material. The fibres, each with a diameter of 1 mm, are located in the vertices of nearly equilateral triangles. The modules are read out at both ends by photomultipliers, via light pipes which match the almost square

portions of the end faces to the circular photo-cathodes. The read out subdivides the calorimeter into five planes in depth: 4.4 cm wide, from the first plane to the fourth, and 5.2 cm for the fifth plane. Each plane is subdivided into elements 4.4 cm wide, called *calorimeter cells*. Five cells aligned in $\varphi$ (the azimuthal angle) for the barrel (or in $x$ for the end-cap) form almost projective towers, called *columns*. The energy deposit in each cell is obtained from the charge measured at each side by the ADCs[5]. The cell time is derived by the time intervals measured at each side by the TDCs[6]. The photon detection efficiency (see Fig. 1.7 left) is an important quantity for various physics channels, among which the $\gamma\gamma$ processes we are interested in, containing one ore more $\pi^0$in the final state (see sections 2.3 and 2.4).
A constant value of more than 98% is observed above 100 MeV, while a loss in efficiency is evident below 100 MeV.

### The drift chamber

The tracking sub-detector of KLOE is a cylindrical drift chamber (DC), with a radius of 2 m and a length of 3.3 m, shown in Fig. 1.8.
In order to obtain a high and uniform track and vertex reconstruction efficiency, wires are strung in an all-stereo geometry, with stereo angles varying with the radius, from 50 mrad to 120 mrad going outward. This allows to fill the entire volume with almost square cells.
A helium-based gas mixture has been chosen, in order to minimise the multiple scattering of low momentum particles, between 50 MeV and 300 MeV. The 90% He + 10% $C_4H_{10}$ mixture has a total radiation length of about 900 m, included the contribution of the 52140 wires.
The walls of the DC are also made of very thin low-Z material, the carbon-fibre-epoxy. All the mechanical structures account for less than 10% of the total radiation length.
A spatial resolution in the $r-\varphi$ plane better than 200 $\mu$m over a large part

[5] Analogue to Digital Converter. A circuit which takes as input an analogue voltage value and returns a proportional digital value.
[6] Time to Digital Converter. In analogy to the ADC, a circuit which measures a time interval and returns a proportional digital value.

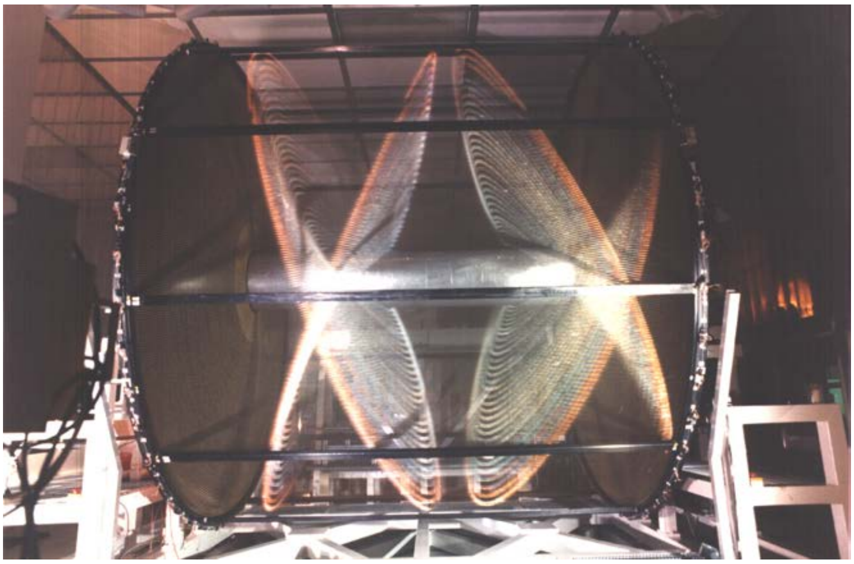

*Figure 1.8: A picture of KLOE drift chamber taken before the installation.*

of the cell is achieved.
The detection efficiency of charged particles is greater than 99%. The measured momentum resolution is of 1.3 MeV/c in the range of polar angles: $50° < \theta < 130°$, corresponding to a relative accuracy in the measurement of the transverse momentum of about 0.3%. The track reconstruction efficiency for pions coming from the interaction point has been measured to be as high as 97% for the angular range: $40° < \theta < 140°$.

### 1.2.3 The trigger system

Besides triggering with the highest possible efficiency on physics events, the trigger system has to cope with a huge rate of background, mainly due to interactions of the beams with the residual gas in the pipe or to Touschek effect. It has to reduce the rate of machine-background events (about 3 kHz), Bhabha scattering events (about 20 kHz), and cosmic-ray events (about 1 kHz) to few kHz. A downscaled fraction of Bhabha and cosmic-ray events is acquired and used for calibration purposes.
Since bunch crossings occur at DAΦNE every 2.7 ns (see Sec. 1.2.1), the

KLOE trigger must operate in continuous mode.
The trigger system is composed of two levels referred to as $T1$ and $T2$. The fast trigger ($T1$) provides a first response about 200 ns after the time zero of the event. The $T1$ signal is synchronised with the DAΦNE *fiducial* signal and distributed to the digitizing electronics of the EmC, acting as *common start* for ADCs and TDCs. The validation trigger ($T2$) confirms the first level about 1.5 $\mu$s after $T1$. The $T2$ signal is distributed to the drift chamber TDCs, acting as a *common stop* and allowing the measurement of drift times, it gives the *start* to the data acquisition system. $T1$ and $T2$ triggers are based on the topology of energy deposits in the EmC and on the number and on the spatial distribution of the DC hits. The EmC and the DC trigger conditions are described as follows.

#### Electromagnetic calorimeter trigger

For trigger purposes, a granularity lower than the one of the EmC is needed; for this reason signals coming from defined groups of cells are summed separately at each side, discriminated, and shaped. From the 5000 photomultipliers, a total of about 200 *trigger sectors* are so defined.

The logic scheme of the discrimination applied for each trigger sector is sketched in Fig. 1.9. Two different threshold values are applied for each side. The first one (H in Fig. 1.9) corresponds to an energy at the side of about 30 MeV, the second one (L) to an energy of about 20 MeV. The double-threshold scheme is applied in order to obtain a response as uniform as possible as a function of the coordinate of the energy deposit along the fibres, and reduce the effect of light attenuation along the fibres.
The resulting effective threshold profile is shown in Fig. 1.10, as a function of the coordinate along the fibres.
Because of the high rate of accidental clusters in the end-cap regions close to the beam, which are due to the machine, the profiles for those end-cap modules have been set differently. Four different threshold values have been applied for the two sides, resulting in an asymmetric shape of the effective

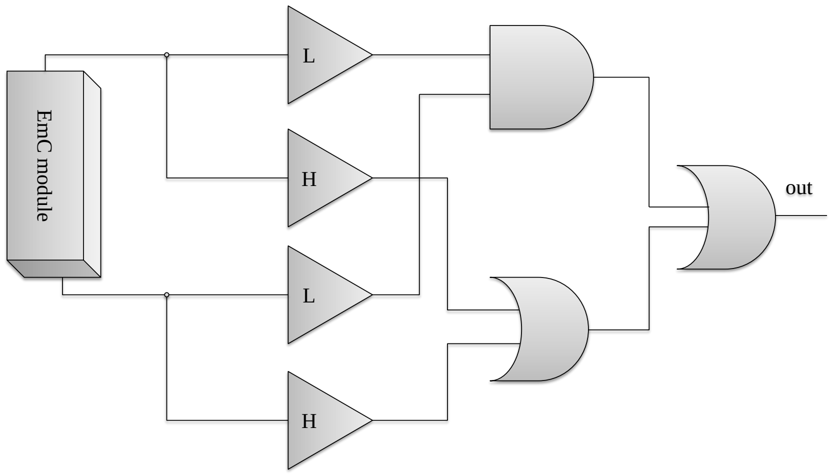


***Figure 1.9:*** *Scheme of the trigger logic applied to a module of the KLOE calorimeter.*

threshold, higher for the region which is closer to the beam axis (*hot* and *warm* trigger regions). For the end-cap modules far from the beam, the thresholds are similar to those of the barrel (*cold* trigger regions).

The EmC condition is said to be satisfied if at least two trigger sectors are fired, less than about 70 ns apart in time, in the following topologies: both on the barrel, or one on the barrel and one on an endcap.

### Cosmic and Bhabha trigger vetoes

In order to identify and reject Bhabha events, two higher threshold values are also applied for each trigger sector, corresponding to an average effective threshold over the module of about 300 MeV (*Bhabha threshold*). In a similar way, signals from the 5th EmC plane at both sides are used to reject cosmic-ray events. The applied effective threshold is again dependent on the coordinate along the fibres and its average value is around 30 MeV (*cosmic threshold*). Events with two sectors above the cosmic threshold or with two sectors above the Bhabha threshold are vetoed by the trigger system. A fraction of about 80% of the cosmic-ray events are identified and rejected

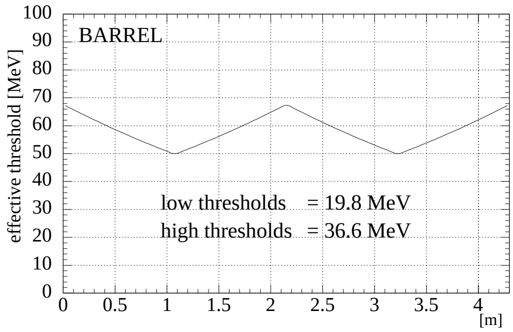


***Figure 1.10:*** *Electromagnetic calorimeter threshold profile as a function of the coordinate along the fibres.*

at the trigger level with this technique. The surviving background events are mainly due to cosmic rays entering (or leaving) the detector through the intersection between the barrel and end-cap calorimeters. A fraction about 4% of Bhabha events survives the Bhabha veto.

### Drift chamber trigger

The drift chamber (DC) hits are grouped into 9 concentric ring sections, the *superlayers*. Different conditions are applied to generate the first and second level triggers:

- The sum of the DC hits within 250 ns is first done at the super-layer level. All the sums are then clipped to a given threshold, and finally they are added to give a total number of hits $N_c$. If $N_c > 15$, a $T1$ signal is generated ($T1D$ condition). This procedure automatically limits the contribution to $N_c$ from low transverse momentum particles coming from the quadrupole magnets, induced by the machine. On the contrary, charged particles produced by decays within the DC volume are favoured, giving a more uniform hit distribution over the super-layers.

- The total number $N_2$ of hits in a time interval of about 1 $\mu$s after the $T1$ is integrated. If $N_2 \geq 155$, the $T2$ is generated ($T2D$ condition).

The logic scheme of the trigger (as represented in Fig. 1.11) is the following: for the first level, the logical OR of the EmC and $T1D$ conditions are required. If at the first level the EmC condition has been satisfied, the $T2$ signal is automatically generated about 1.5 $\mu$s after $T1$; if $T1D$ has generated the first level, the logical OR of the EmC and $T2D$ conditions are required to generate the $T2$.

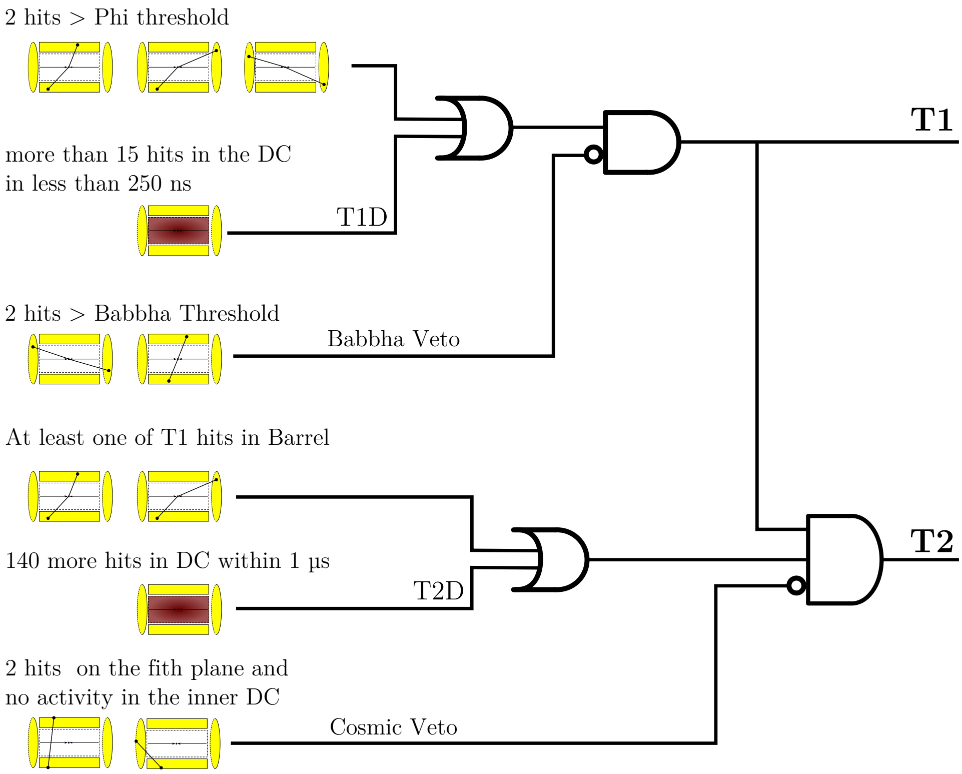


***Figure 1.11:*** *A logic scheme of the KLOE trigger system.*

## 1.3 From KLOE to KLOE-2

With the upgraded DAΦNE a new data campaign has been approved, together with several detector upgrades that are currently made or in progress. In this section we will briefly describe these upgrades. For a more detailed description of detectors and of the KLOE-2 scientific programme, see reference [3].

We stand now in the end of the first phase, referred to as STEP-0. In this phase two different detectors, namely the Low Energy Tagger (LET) and High Energy Tagger (HET) are installed along the beam line to detect the scattered $e^+e^-$from $\gamma\gamma$ interactions.

In a second phase, referred to as STEP-1, a light-material internal tracker (IT) will be installed in the region between the beam pipe and the drift chamber, in order to improve charged vertex reconstruction and to increase the acceptance for low transverse momentum particles.
A Crystal calorimeter (CCALT) will cover the low $\theta$ region, aiming at increasing acceptance for very forward electrons/photons down to 8°.
A new tile calorimeter (QCALT) will be used to instrument the DAΦNE focusing system for the detection of photons coming from decays within the drift volume chamber.
The integrated luminosity planned for the two phases will be 5 fb$^{-1}$ and 20 fb$^{-1}$, respectively.

### 1.3.1 STEP-0 upgrades

In the STEP-0 phase, new data will be taken with the new DAΦNE configuration and the old KLOE detector plus the lepton tagging system.
We give here only a brief overview of this system, which is the main topic of this thesis.
The results of our simulations (see chapter 3) show that we need to place

new detectors in two different regions on both sides of the IP:

- The Low Energy Tagger (LET) region where we can detect leptons with an energy between 50 and 450 MeV;
- and the High Energy Tagger (HET) region, where we detect leptons having an energy greater than 420 MeV.

We found that in the LET region, the energy of the leptons is uncorrelated to the position of the hitting point. For this reason the LET detector has to be a calorimeter (see Sec. 3.3.1).
The HET detector is located just at the exit of the dipole magnets, where leptons show a clear correlation between energy and deviation from nominal orbit (see Sec. 3.3.2). For this reason, in this case a position detector is used. It measures these deviations, allowing one to infer the energies of the particles.
The description of the HET detector is the main purpose of this thesis and will be deeply discussed in chapter 4. All the other detectors of the KLOE-2 upgrade will be briefly analysed in this section.

#### The low energy tagger detector: LET

The LET detector [4] consists of a calorimeter detecting electrons and positrons within an energy range between 50 and 450 MeV.
Inside the KLOE detector (1.5 m away from the IP), the environmental conditions require radiation-tolerant devices, insensitive to magnetic fields. Moreover this detector has to provide a good energy resolution in the measurement of the $\gamma\gamma$ invariant mass, a good time resolution to associate the detected events with the proper bunch crossing, and a must have small size. A right choice to fulfil these requirements is a high-$Z$ scintillator with high light yield and fast emission. Furthermore the readout devices must be radiation hard photo-detector insensitive to magnetic field. To this purpose the new Cerium doped Lutetium Yttrium Orthosilicate (LYSO) crystal scintillators were chosen, coupled to silicon photomultipliers (SiPM).

*Figure 1.12: A drawing of the KLOE inner tracker inserted at the interaction point.*

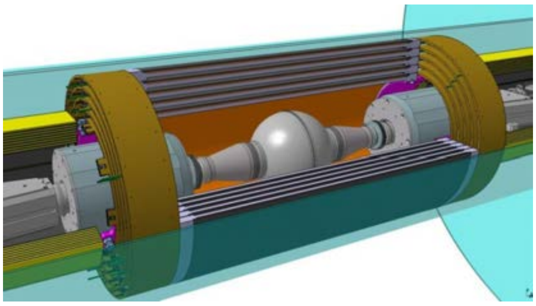

### 1.3.2 STEP-1 upgrades

#### The inner tracker

An inner tracker (IT) detector will be installed to improve vertex reconstruction.
The requirements for this kind of detector are:

- Good space resolution: $\sigma_{r\phi} \sim 200\ \mu$m and $\sigma_z \sim 500\ \mu$m;
- Low-Z material: < 2% of a radiation length;
- High rate capability: 5 kHz/cm$^2$.

In order to build the inner tracker we have chosen to use the GEM[7] technology.
The IT will be composed of 4 cylindrical concentric GEM layers (see Fig.1.12) with radii from 13 to 23 cm from the interaction point and before the drift chamber inner wall. It will have a 700 mm long active area and will be read out with XV strip-pads (40° stereo angle).
In order to place as few material as possible between the IP and the DC, the detector will have only a 1.5% of total radiation length in the active region, thanks to the use of mechanical supports made of carbon fibre.

[7] GEM acronym stands for Gas Electron Multiplier.

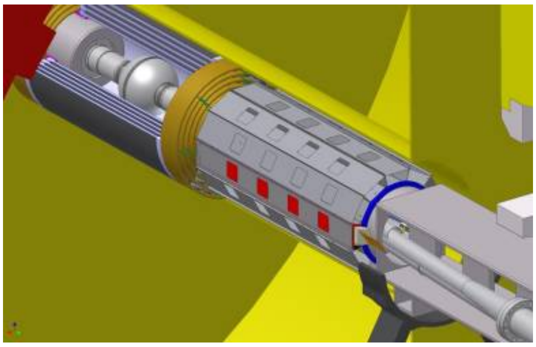

*Figure 1.13:* *A drawing of the KLOE QCALT.*

### The quadrupole calorimeter with time (QCALT)

Particles coming from secondary vertex, inside the drift chamber volume, can hit one of the quadrupole magnets and not be detected. For this reason, a calorimeter was installed around the quadrupole in the past: the QCAL detector. The new QCALT calorimeter will provide much better performances.
The rare decay $K_L \to 2\,\pi^0$ is an example of the physics channels whose measurement will benefit of the QCALT insertion. In fact the most important background source in this measurement is $K_L \to 3\,\pi^0$.
The old QCAL detector worked very well on rejecting background losing only 1% of the signal. The QCALT will increase the detection efficiency and the high granularity will help on reducing accidental losses. The measurement of some rare decays, e.g. $K_L \to 2\,\pi^0$ will greatly benefit from the improved QCALT performance, rejecting the most important background sources in the measurement as $K_L \to 3\,\pi^0$. The QCALT detector, shown in Fig. 1.13, will be composed of two tile calorimeters, a wavelength shifter and SiPM readout. It will have a dodecagonal structure (1 m length) made of 5 layers of tungsten (3.5 mm) + tiles (5 mm) + air gap (1 mm), for a total of 4.75 cm (corresponding to 5.5 $X_0$); 20 cells/layer (100 SIPM/module) for a total of 2400 readout channels. The QCALT will be located just outside the inner tracker, it will have a granularity of 5×5÷5×7.7 cm$^2$ (tiles). Its time resolution will be less than 1 ns, 10 times faster than the old QCAL.

### The crystal calorimeter with time (CCALT)

In order to increase the angular efficiency of the KLOE electromagnetic calorimeter, an additional small detector will be placed as shown in Fig. 1.14. The present electromagnetic calorimeter (see section 1.2.2) covers the polar angle down to 21°; the CCALT will cover the polar angle down to 8°. With such a detector we can improve the measurement of the branching ratio of the reaction $K_S \to \gamma\gamma$, together with the measurement of the transition form factor of the $\pi^0$. The latter will be performed by means of the $\gamma\gamma$ reaction $e^+e^- \to e^+e^-\pi^0$ discussed in section 2.4.
The major background for this process is the decay channel $K_S \to \pi^0\pi^0 \to 4\gamma$, with two photons lost in the beam pipe or due to the EmC inefficiency. With the CCALT calorimeter we will increase the efficiency on small angle photon detection, thus improving the precision on this measurement.
The CCALT will be made of 2 small barrels of 48 LYSO crystals each, with a length of 8-9 cm and transversal area of 1.5×1.5 cm$^2$.

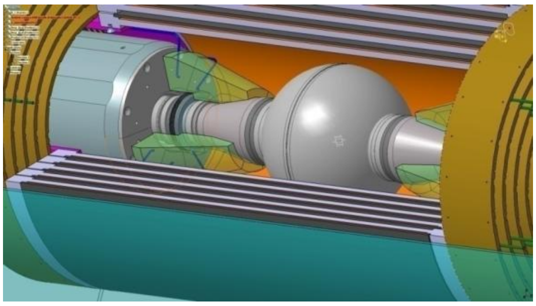

***Figure 1.14:*** *A drawing of the KLOE CCALT.*

# Chapter 2

# Two-photon physics at DAΦNE

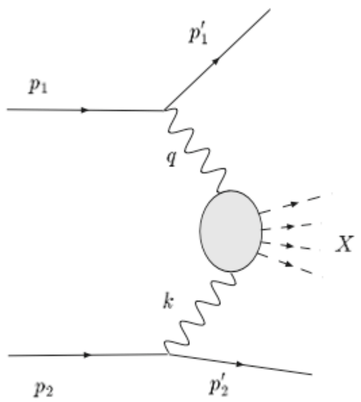


***Figure 2.1:*** *A diagram of two-photon particle production in a $e^+e^-$ collider.*

The term "two-photon physics", or "$\gamma\gamma$ physics", at an $e^+e^-$ collider, stands for the reaction (see Fig. 2.1):

$$e^+e^- \to e^+e^-\gamma^*\gamma^* \to e^+e^- X$$

where $X$ is an arbitrary final state, allowed by conservation laws.
The two photons are in a $C = +1$ state. At the energy of DAΦNE, photons are

quasi-real, so the value $J = 1$ is excluded (Landau-Yang theorem), photon-photon scattering [5] at the $e^+e^-$ colliders gives access to $J^{PC} = 0^{\pm+}, 2^{\pm+}$ final states. This kind of states are not directly coupled to one photon having $J^{PC} = 1^{--}$.

Moreover, the cross section of these processes, of $\mathcal{O}(\alpha^4)$, grows with the logarithm of the energy in the centre of mass $E$. On the other hand, one photon processes are $\mathcal{O}(\alpha^2)$, but their cross section is inversely proportional to $E$. Consequently, for $E$ greater than a few GeV, $\gamma\gamma$ physics dominates hadronic production at $e^+e^-$ colliders.

For quasi-real photons, the number of produced events can be estimated from the expression:

$$N = L_{ee} \int \mathrm{d}W_{\gamma\gamma} \frac{\mathrm{d}L}{\mathrm{d}W_{\gamma\gamma}} \sigma(\gamma\gamma \to X) \tag{2.1}$$

where $L_{ee}$ is the machine luminosity, $W_{\gamma\gamma}$ is the photon-photon energy in the centre of mass ($W_{\gamma\gamma} = M_X$), $\mathrm{d}L/\mathrm{d}W_{\gamma\gamma}$ is the photon-photon flux and $\sigma(\gamma\gamma \to X)$ is the cross section of the production of a given final state $X$.

The photon flux at DAΦNE ($\sqrt{s} = 1.02\,\mathrm{GeV}$) is shown in Fig. 2.2, where accessible final states are also indicated.

Over the years, the cross section $\sigma(\gamma\gamma \to X)$ was studied at all the $e^+e^-$colliders, like PETRA [1], CESR [2] and LEP[3]. In the low-energy region, $m_\pi \leq W_{\gamma\gamma} \leq 700$ MeV, the experimental situation [6] is unsatisfactory for several reasons:

- large statistical and systematic uncertainties due to small data samples and large background contributions;

- very small detection efficiency and particle identification ambiguities

[1]PETRA acronym stands for Positron-Elektron-Tandem-Ring-Anlage, "positron-electron tandem-ring facility". PETRA is an $e^+e^-$ collider capable of accelerating leptons up to 19 GeV at the German facility of DESY (Deutsches Elektronen Synchrotron, "German Electron Synchrotron") in Hamburg.

[2]The Cornell Electron Storage Ring (CESR) is an $e^+e^-$ collider at Cornell University (Ithaca, NY, U.S.A.) with an energy in the centre of mass up to 12 GeV.

[3]The Large Electron-Positron Collider (LEP) was one of the largest particle accelerators ever constructed. It operated from 1989 up to 2000, reaching an energy in the centre of mass of 209 GeV.

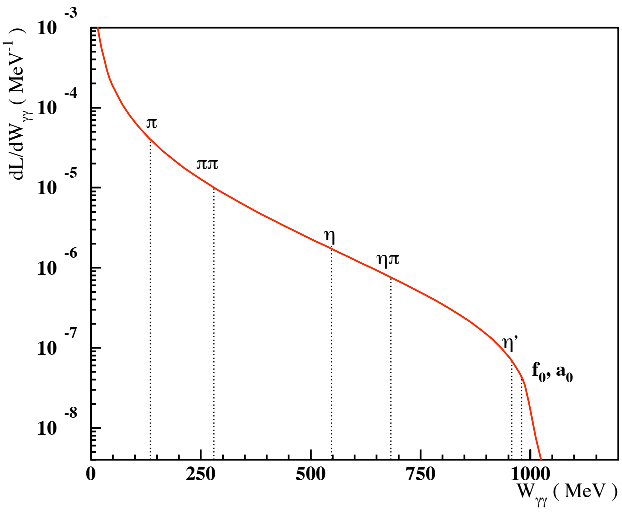


*Figure 2.2:* *Photon-photon flux at DAΦNE as function of $W_{\gamma\gamma}$ for a machine integrated luminosity $L_{ee}$ of* 1 fb$^{-1}$.

for low-mass hadronic systems.

Thanks to its high luminosity, DAΦNE will give the opportunity for precision measurements of low-mass hadronic systems with KLOE-2.

## 2.1 Two-photon processes versus $\phi$-meson decays

As we have seen in section 1.2.1, the energy in the centre of mass of DAΦNE is tuned on the value of 1020 MeV, the mass of the $\phi$-resonance. In such a configuration, $\phi$-particles are produced copiously and the number of their decay products overwhelms the tiny amount of $\gamma\gamma$ events.
Let us take as an example the reaction:

$$e^+e^- \to e^+e^-\gamma\gamma \to e^+e^-\pi^0\pi^0. \tag{2.2}$$

In most of the cases, leptons in the final state are scattered at small angle, therefore they are not detected by KLOE. In the final state there will be two

| Channel | Events | $\phi$-decay | Miss | BG events | Ratio |
|---|---|---|---|---|---|
| $e^+e^- \to e^+e^-\pi^0\pi^0$ | $2\times10^4$ | $K_S(\pi^0\pi^0)K_L$ | $K_L$ | $\sim 10^9$ | $\sim 2\times10^{-5}$ |
| $e^+e^- \to e^+e^-\pi^+\pi^-$ | $2\times10^6$ | $K_S(\pi^+\pi^-)K_L$ | $K_L$ | $\sim 2\times10^9$ | $\sim 1\times10^{-3}$ |
| | | $\pi^+\pi^-\pi^0$ | $\pi^0$ | $\sim 1\times10^9$ | $\sim 2\times10^{-3}$ |
| $e^+e^- \to e^+e^-\eta$ | $1\times10^6$ | $\eta(\gamma\gamma)\gamma$ | $\gamma$ | $\sim 10^8$ | $\sim 1\times10^{-2}$ |
| $e^+e^- \to e^+e^-\pi^0$ | $4\times10^6$ | $\pi^0(\gamma\gamma)\gamma$ | $\gamma$ | $\sim 5\times10^8$ | $\sim 8\times10^{-3}$ |

***Table 2.1:*** *Background processes for $\gamma\gamma$ physics coming from $\phi$-decays. Numbers of events are estimated supposing an integrated luminosity of* $1\ \mathrm{fb}^{-1}$.

$\pi^0$ plus some missing energy.
On the other hand, let us suppose that a $\phi$-particle, produced at the interaction point, decays into $K_SK_L$ (branching ratio of ∼34%). Afterwards the $K_S$ decays as following (B.R. ∼31%):

$$K_S \to \pi^0\pi^0. \tag{2.3}$$

The overall process that takes place is:

$$e^+e^- \to \Phi \to K_SK_L \to \pi^0\pi^0K_L. \tag{2.4}$$

Let us suppose that the $K_L$ manages to escape the KLOE electromagnetic calorimeter. In this case, the detected final state would be: two $\pi^0$ plus some missing energy, exactly the same as in the $\gamma\gamma$ case.
In table 2.1 a list of interesting $\gamma\gamma$ physics channels is presented. For each of them, there is at least one $\phi$-decay which could produce an identical final state in the detector and fake the signal. From the last column of table 2.1 and figure 2.3 it is apparent that background processes are dominant[4].

[4] We refer to $\phi$-decays as "background processes", because we are interested in $\gamma\gamma$ processes. Although they are interesting physics channels and, on top of that, they are the processes DAΦNE and KLOE are meant to study.

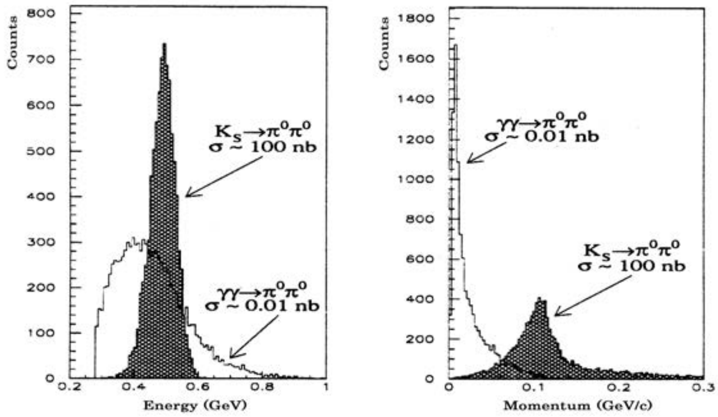


*Figure 2.3:* *Comparison of invariant mass (left) and transverse momentum (right) between an example of signal ($\gamma\gamma \to \pi^0\pi^0$) and background ($K_S \to \pi^0\pi^0$). The amplitude of the $\gamma\gamma$ process is magnified by a factor $10^4$ in order to make the plots readable.*

## 2.2 Tagging the off-energy leptons

The $\gamma\gamma$ processes differ from the $\phi$-decay because of the presence of the $e^+e^-$ in the final state. If we detect those leptons and measure their energy, we can disentangle $\gamma\gamma$ from other processes and close the kinematics. In order to achieve this result, the so called *lepton tagging system* has been designed and built. According to the machine layout (see chapter 3), two positions were found to install new detectors, one next to the interaction point and one after the dipole magnet. So the tagging system is composed of 2 pairs of detectors per arm (positron and electron): the Low Energy Tagger (LET) and the High Energy Tagger (HET). The former is placed inside the KLOE apparatus and catches lower energy leptons, i.e. leptons which emitted a high energy photon. The latter is placed 11 m away from the interaction point and from the KLOE detector, after the bending dipole magnet. It detects those leptons which have lost such a tiny amount of energy that they manage to reach the exit of the dipole magnet. The exact location and the working principles of these detectors will be discussed in sections 3.3.1 and 3.3.2, after having analysed the tracking of the off-energy leptons along the machine lattice.

Moreover, the design and building of the High Energy Tagger detector and its electronic system are the main topics of this thesis and will be deeply discussed in chapters 4 and 5.

## 2.3 The process $\gamma\gamma \to \pi^0\pi^0$: the $\sigma$ case

The existence of the scalar $\sigma$ meson was suggested for the first time in the frame of the linear sigma model to describe pion-nucleon interactions. However, no clear observation of it was provided by the experiments, so that its existence and nature (i.e. quark substructure) is still controversial.

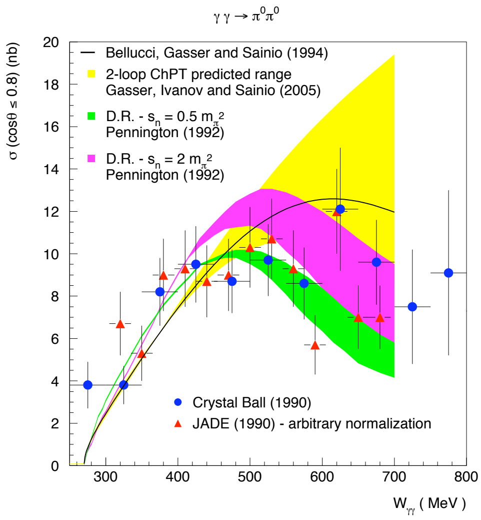


***Figure 2.4:*** *Comparison of all present data from Crystal Ball and JADE (arbitrarily normalised at the Crystal Ball data) to the predictions from ChPT (solid and yellow band) and dispersion relation techniques (green and magenta bands).*

Recently, the situation has changed. In 2006, it was shown [7] that the $\pi\pi$ scattering amplitude contains a pole, with the quantum numbers of vacuum, with a mass of $M_\sigma = 441^{+16}_{-8}$ MeV and a width $\Gamma_\sigma = 544^{+25}_{-18}$ MeV. The $\sigma$ has been looked for also in $D$ decays by the E791 Collaboration at Fermilab[5] [8].

From the $D \to 3\pi$ Dalitz plot analysis, E791 has found that almost 46% of the width is due to $D \to \sigma\pi$ with $M_\sigma = (478 \pm 23 \pm 17)$ MeV and $\Gamma_\sigma = (324 \pm 40 \pm 21)$ MeV. BES[6] [9] has been looking for the $\sigma$ in $J/\psi \to \omega\pi^+\pi^-$ giving a mass value of $M_\sigma = (541 \pm 39)$ MeV and a width of $\Gamma_\sigma = (252 \pm 42)$

[5] E791 is an experiment meant to study the production and the decay of charmed particles produced using a 500 GeV $\pi^-$ beam on platinum and carbon targets at the Fermilab Tagged Particle Spectrometer.

[6] BES acronym stands for Beijing Spectrometer. It is a general-purpose detector located in the interaction region of the Beijing Electron Positron Collider (BEPC).

MeV.

In principle, the $\sigma$ case could be definitively solved by studying the channel $\gamma\gamma \to \pi^0\pi^0$ (i.e. the process $e^+e^- \to e^+e^-\pi^0\pi^0$), in the low energy region (as a matter of fact, for low energy photons, the process $\gamma\gamma \to \pi^+\pi^-$ is dominated by the Born term, due to the photon coupling to the net electric charge of the pions). Theoretical predictions for this process are based on the Chiral Perturbation Theory (ChPT) at the two-loop level [10, 11] and dispersive techniques [12] (see Fig. 2.4).

Again in 2006, an evaluation of the $\gamma\gamma \to \pi^0\pi^0$ process, in presence of the $\sigma$ resonance, has been performed through a special Montecarlo generator [13] developed to this purpose[7]. The line shape of the cross-section appears to be sensitive to the quark structure of the $\sigma$ meson, since the two photons directly couple to the electric charge of the constituent quarks.

From the experimental side, the only available data in the energy region of interest come from the Crystal Ball collaboration [6] [8]. Unfortunately, as figure 2.4 clearly shows, the large uncertainties affecting the data, do not allow one to come to any conclusion about the agreement with either of the theoretical approaches, nor on the possible existence of a resonance-like structure in the region going from 400 MeV to 500 MeV.

The effect of the inclusion of the $\sigma$ resonance, using the NPP MC code, is shown in Fig. 2.5.
The expected production rate can be calculated by inserting the ChPT prediction for $\sigma(\gamma\gamma \to \pi^0\pi^0)$ in Eq. 2.1. In this case the integral runs over the region $W_{\gamma\gamma} = [2m_\pi, 2E]$, i.e. beyond the validity domain of ChPT ($W_{\gamma\gamma} \leq$ 700 MeV). By choosing a conservative extrapolation for the cross section in the region $W_{\gamma\gamma} > 700$ MeV corresponding to the value given by ChPT for

[7]This code, referred to as the "Nguyen-Piccinini-Polosa" (NPP) Monte Carlo code, is the same used in section 3.2.1.

[8]In this energy region there are also not normalised JADE data [14]. Upon an arbitrary scaling, they are consistent with Crystal Ball data.

$W_{\gamma\gamma} = 700\,\mathrm{MeV}$, one gets:

$$\sigma(e^+e^- \to e^+e^-\pi^0\pi^0) \simeq 13\ \mathrm{pb}, \tag{2.5}$$

i.e. 65 000 events for an integrated machine luminosity of $5\,\mathrm{fb}^{-1}$, planned for the STEP-0 of KLOE-2.

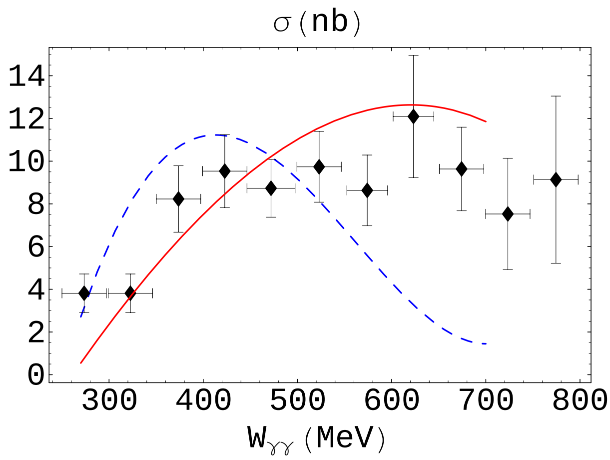


***Figure 2.5:*** *The Crystal Ball data and the two-loop ChPT prediction (red curve) of Fig. 2.4 are compared with the cross section for the process $\gamma\gamma \to \sigma \to \pi^0\pi^0$ calculated with the Nguyen-Piccinini-Polosa MC code (blu curve).*

## 2.4 The process $\gamma\gamma \to \pi^0$

By means of the single $\pi^0$ production, we plan to perform two measurements:

- the $\pi^0 \to \gamma\gamma$ decay width: $\Gamma_{\pi^0\to\gamma\gamma}$;
- the $\gamma^*\gamma \to \pi^0$ transition form factor: $F(Q^2)$.

A complete feasibility study has been performed and is available in Ref. [15]. In this section a brief description is given, trying to put into evidence the importance of the High Energy Tagger for these measurements.

Back in 1960, Francis E. Low proposed to measure the $\pi^0$ lifetime, by means of its production in $e^-e^-$ or $e^+e^-$ collisions. Since then, this measurement has only been done with the Crystal Ball detector at DESY[16] in 1988, with the result $\Gamma_{\pi^0\to\gamma\gamma} = (7.7 \pm 0.5 \pm 0.5)$ eV.
For a precision measurement of $\pi^0$ width through the "$\gamma\gamma$ fusion" ($\gamma\gamma \to \pi^0$) process, it is necessary to improve the original Low's proposal. Namely, instead of a no-tag[9] experiment, one should perform the tagging of both leptons at small angles.
Thanks to the *lepton tagging system* (introduced in Sec. 1.3.1) recently installed at DAΦNE, and the High Energy Tagger (HET) in particular, we are now able to perform a double tagging.

One can extract the value of the partial decay width from data, using the formula

$$\Gamma_{\pi^0\to\gamma\gamma} = \frac{N_{\pi^0}}{\varepsilon\,\mathcal{L}} \cdot \frac{\tilde{\Gamma}_{\pi^0\to\gamma\gamma}}{\tilde{\sigma}_{e^+e^-\to e^+e^-\pi^0}}, \tag{2.6}$$

where $N_{\pi^0}$ is the number of detected pions, $\varepsilon$ accounts for the detection acceptance and efficiency, $\mathcal{L}$ is the integrated luminosity, and $\tilde{\Gamma}_{\pi^0\to\gamma\gamma}$ is the $\pi^0$ width calculated from the model and $\tilde{\sigma}_{e^+e^-\to e^+e^-\pi^0}$ is the cross section obtained with a Monte Carlo simulation using the same model as for the $\tilde{\Gamma}_{\pi^0\to\gamma\gamma}$ calculation.

The form factor $F(Q^2)$ can be evaluated through the relation:

$$\frac{F^2(Q^2)}{F^2(Q^2)_{MC}} = \frac{(\frac{d\sigma}{dQ^2})_{data}}{(\frac{d\sigma}{dQ^2})_{MC}}, \tag{2.7}$$

[9]By the expression no-tag, we refer to experiments which are not capable to detect any of the two leptons in the final state.

where $(\frac{d\sigma}{dQ^2})_{data}$ is the experimental differential cross section, and $(\frac{d\sigma}{dQ^2})_{MC}$ is the Monte Carlo one, obtained with the form factor $F(Q^2)_{MC}$.

The $\pi^0$ production in the process $e^+e^-\pi^0$ is simulated with EKHARA [17] Monte Carlo event generator (see Sec. 3.2.2). The simulated signal is given by the $t$-channel amplitude ($\gamma^*\gamma^* \to \pi^0$).
Further work has been done, in order to simulate DAΦNE optics and tracking leptons up to the HET stations. Details on the tracking procedure are discussed exhaustively in chapter 3. For the time being, we can say that the results obtained through this procedure allowed us to provide a realistic estimate of the HET detector acceptance being about 2%.
In the following, we will refer to the coincidence of both the HET detectors as the HET-HETcoincidence. Requiring this coincidence means requiring that each of the two scattered leptons must be detected by the relative HET detector. This selects leptons in the final state with an energy ranging from 420 MeV to 460 MeV[10].

### 2.4.1 Feasibility of the $\pi^0$ width measurement

Figure 2.6 shows the energy of the emitted $\pi^0$ in the $\gamma\gamma$ process: as can be seen, the request of the HET-HET coincidence allows us to select $\pi^0$ almost at rest (dark region), compared with the case in which at least one lepton is undetected (light-gray). Since the $\pi^0$ decays almost at rest, most of the photons from its decay are emitted back-to-back. As shown in Fig. 2.7, about 95% of the photons are emitted above 25 ° and below 155 °, resulting in a large acceptance for photons reaching the KLOE Electromagnetic Calorimeter[11] (EmC).

By requiring both photons in the barrel of the EmC (between 50° and

[10]This piece of information comes from the tracking procedure analysed in chapter 3. For a quick understanding, see Fig. 3.15 on Pag. 58

[11]For a description of the KLOE Electromagnetic Calorimeter see Sec. 1.2.2.

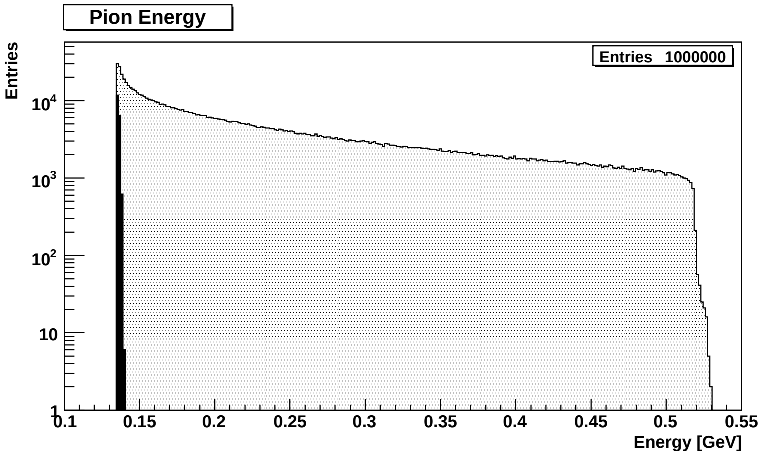


***Figure 2.6:*** *The $\pi^0$ energy (in the laboratory frame) distribution with (dark) and without (light-gray) HET-HET coincidence.*

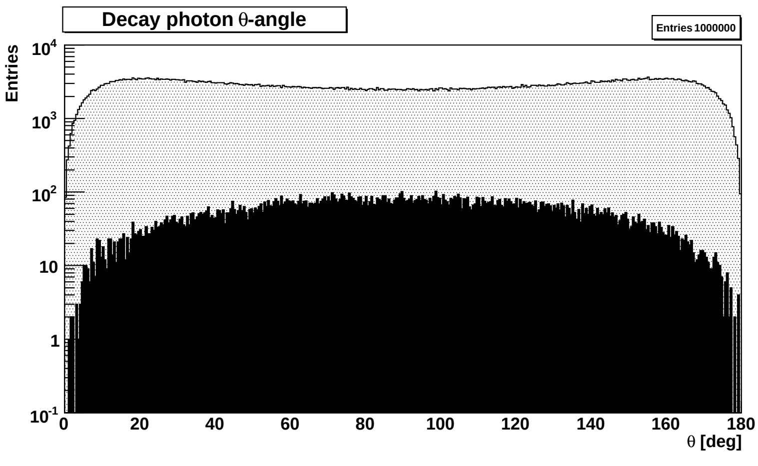


***Figure 2.7:*** *Polar angle (in the laboratory frame) distribution of decay photons from $\pi^0$ with (dark) and without (light-gray) the HET-HET coincidence.*

130°) and the HET-HET coincidence, a value for the acceptance $\epsilon_{acc}$ of 1.2% is obtained. Since the total cross-section of $e^+e^-\pi^0$ at $\sqrt{s}$ = 1020 MeV is $\sigma_{tot} \approx 0.28\,$nb, a cross-section of about 3.4 pb is obtained within the acceptance cuts. The integrated luminosity $\mathcal{L}$ at DAΦNE required to reach a 1% statistical error is:

$$\mathcal{L} = \frac{10000}{\sigma_{tot}\,\epsilon_{acc}\,\epsilon_{det}} \approx \frac{3\,\mathrm{fb}^{-1}}{\epsilon_{det}}, \tag{2.8}$$

where the efficiency $\epsilon_{det}$ due to trigger, reconstruction and analysis criteria is estimated to be about 50%, by means of the KLOE Monte Carlo code (`GEANFI`[18]). Therefore, the required data sample can be obtained during the STEP-0, the first phase (about one year) of data taking.
Our simulation shows that the uncertainty in the measurement of $\Gamma(\pi^0 \to \gamma\gamma)$ due to the form factor parametrisation in the generator is expected to be less than 0.1%.

### 2.4.2 Feasibility of the $\gamma^*\gamma \to \pi^0$ transition form factor measurement

By requiring one lepton inside the KLOE detector[12] and the other lepton in one of the HET detectors[13], one can measure the differential cross section $(d\sigma/dQ^2)_{data}$, where $Q^2 \equiv -q^2$. Using Eq. 2.7, the form factor $|F(Q^2)|$ can be extracted from this cross section.

Figure 2.8 shows the expected experimental uncertainty (statistical) on $F(Q^2)$ achievable at the KLOE-2, with an integrated luminosity of $5\,\mathrm{fb}^{-1}$. In this measurement the detection efficiency is different and is estimated to be about 20%. From our simulation we conclude that a statistical uncertainty of less than 6% for every bin is feasible.

Having measured the form factor, one can evaluate also the slope pa-

[12] corresponding to $20° < \theta < 160°$, and to $0.01\,\mathrm{GeV}^2 < |q^2| < 0.1\,\mathrm{GeV}^2$
[13] corresponding to $|q^2| \lesssim 10^{-4}\,\mathrm{GeV}^2$ for most of the events

rameter $a$ of the form factor at the origin[14]

$$a \equiv m_\pi^2 \frac{1}{\mathcal{F}_{\pi^0\gamma^*\gamma^*}(0,0)} \left. \frac{d\,\mathcal{F}_{\pi^0\gamma^*\gamma^*}(q^2,0)}{d\,q^2} \right|_{q^2=0} . \tag{2.9}$$

From the experimental side, the PDG average value of the slope parameter is quite precise, $a = 0.032 \pm 0.004$ [19], and it is dominated by the CELLO[15] results [20]. In the latter, a simple vector-meson dominance (VMD) form factor parametrization was fitted to the data and then the slope was calculated according to Eq. 2.9. Thus the CELLO procedure for the slope calculation suffers from model dependence not accounted for in the error estimation. The validity of such a procedure has never been verified, because there were no data at $Q^2 < 0.5\,\mathrm{GeV}^2$. Therefore, filling of this gap in $Q^2$ by the KLOE-2 experiment can provide a valuable test of the form factor parametrizations.

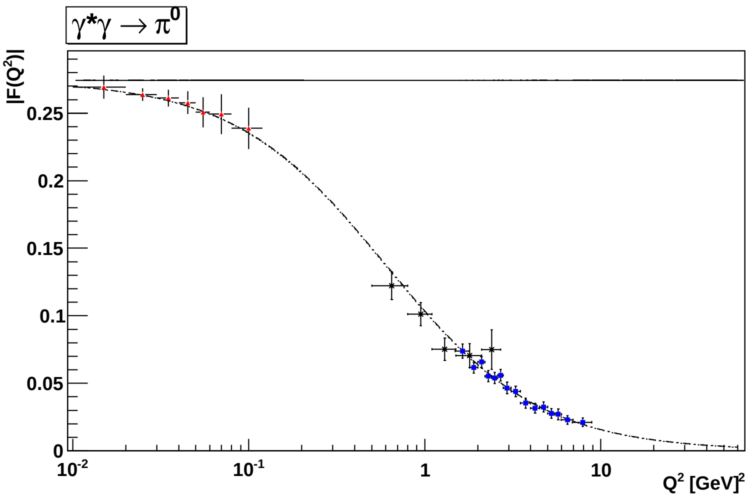


***Figure 2.8:*** *Simulation of KLOE-2 measurement of $F(Q^2)$ (red triangles) with statistical errors for $5\,\mathrm{fb}^{-1}$. Dashed line is the $F(Q^2)$ form factor according to LMD+V model [21], solid line is $F(0)$ given by Wess-Zumino-Witten term. CELLO [20] (black crosses) and CLEO[16] [22] (blue squares) data at high $Q^2$ are also shown for illustration.*

[14] We would like to stress that the $q^2$ range of KLOE-2 measurement is not small enough to use the linear approximation $\mathcal{F}_{\pi^0\gamma^*\gamma^*}(q^2,0) = \mathcal{F}_{\pi^0\gamma^*\gamma^*}(0,0)(1+q^2\,a/m_\pi^2)$ because the higher order terms are not negligible.

[15] CELLO is a large $4\pi$ magnetic detector at the PETRA facility at DESY, Hamburg.

When the normalization of the form factor is fixed to the decay width $\pi^0 \to \gamma\gamma$ or to some effective pion decay constant $F_\pi$, the VMD, as well as the more sophisticated LMD+V model [21], has only one free parameter. It is *a priori* not clear why only one parameter should be sufficient to describe the behaviour of the form factor simultaneously at low momenta (slope at the origin) and at large momenta. Since the available data [20, 22, 23] cover only the relatively high $Q^2 > 0.5\,\mathrm{GeV}^2$ region, a new measurement by KLOE-2 at $Q^2 < 0.1\,\mathrm{GeV}^2$ would help to verify the consistency of the parametrizations of the form factor $F(Q^2)$.

Moreover these measurements can have an impact on the value and precision of the contribution of a neutral pion exchange to the hadronic light-by-light scattering. According to our simulations (see reference [15] for details), this can improve the uncertainty on the value of the anomalous magnetic moment of the muon by a factor $\sim 2$.

# Chapter 3

# Generation and tracking

## 3.1 Preliminary tracking of off-energy leptons in DAΦNE lattice

In order to find a location to properly install each detector of the lepton tagging system, we needed to track the off-energy particles along DAΦNE optics. The region we took into account starts from the interaction point (IP) and ends at the exit of the first bending dipole magnet at the end of the straight section. The simplified magnetic layout of the transfer line[1] of DAΦNE collider which is relevant for our calculations is shown in Fig. 3.1. The lower line in figure is the positron short line and it is the one used for simulations. Here the magnets, which our simulation is more sensitive to, are shown: the defocusing quadrupole QD0 and the focusing one QF1.

The code generally used for optics calculations in accelerator physics is `MAD`[2] [24]. This code approximates all magnetic elements as thin lenses. For

[1] With respect to the actual machine lattice (see Fig. 1.4 and Tab. 1.3 on Pag. 8 and 9), the simplified layout is missing the KLOE solenoidal magnetic field and all the permanent-magnet compensator.

[2] `MAD` acronym stands for Methodical Accelerator Design. It is a software developed at CERN for accelerator design and simulation.

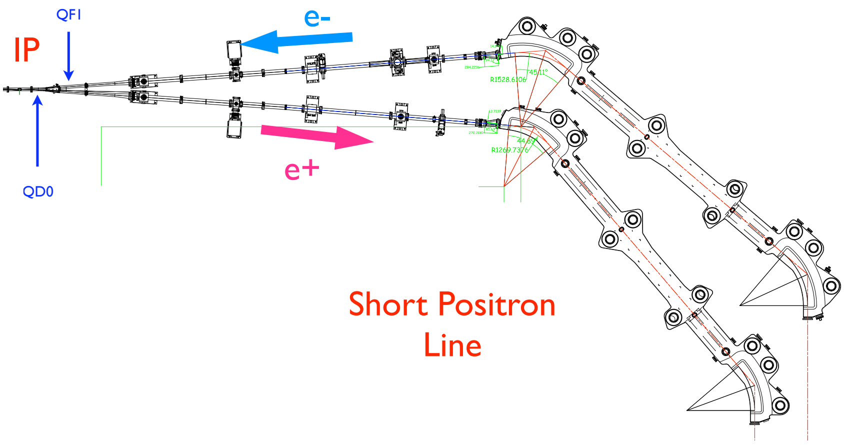


***Figure 3.1:*** *Magnetic layout of one side of DAΦNE main rings, relevant for the $\gamma\gamma$ tagger.*

this reason it is strictly meant to study the optical properties of the nominal beam alone, i.e. the ones which the magnetic elements are set for. The error due to thin lens approximation, becomes more and more important as the particle energy deviates from the nominal one, 510 MeV in the case of DAΦNE.
For our study, we needed a tool that allowed us to calculate both the nominal and the off-energy particle tracks with the same precision. This has determined the choice of using the `BDSIM`[3] [25] code. In `BDSIM`, particle tracks are calculated by solving the equation of motion, taking into account the Lorentz force in presence of a magnetic field. A more detailed description of `BDSIM` structure and functionality can be found in reference [26].

We have firstly calculated the path of a nominal particle (a 510 MeV positron) to check that it fitted exactly with the QF1 line[4]. This check is needed to prove that the transfer line was correctly modelled: proper values of the QD0 quadrupole coefficients were chosen and the centre of all

[3]Beam-line Simulation Toolkit based on Geant4.
[4]We define “QF1 line” the part of transfer line on which QF1 magnet is mounted. This is rotated (about 4 degrees) with respect to the absolute $z$ axis, coincident with the QD0 axis

magnetic elements was correctly set.
The sets of $(x, y, z)$ coordinates, calculated with `BDSIM`, have been successfully superimposed on the technical design of the beam-pipe boundary, to check that the nominal particle track was actually centred.

As a second step, we calculated the trajectories of all particles with energies from 5 MeV up to 510 MeV in steps of 0.5 MeV. Within this preliminary study, particles have been produced at the IP with the same direction of the nominal one, i.e. $-25$ mrad with respect to the $z$ axis. The study of the energy and momentum distributions at the IP was subsequently performed by means of several Monte Carlo codes described in section 3.2.1.

| Energy Range[MeV] | Distance from IP[cm] | Description |
|---|---|---|
| 0-150 | 0-53 | IP - QD0 |
| 155-220 | 53-79 | splitter |
| 225-255 | 79-84 | QF1 |
| 260-325 | 340-760 | quaps100-quaps102 |

***Table 3.1:*** *Summary of the regions where off-momentum particles are lost along the beam line in absence of solenoidal field. Results refer to particles having various energy values but starting at IP with a polar angle of* $-25$ mrad *with respect to the z axis.*

In Tab. 3.1 we report the $z$-coordinate along the beam line for particles of different energies resulting from the preliminary tracking. Particles with an energy lower than 260 MeV impinge on the internal side (with respect to the centre of the machine) of the beam pipe (see Fig. 3.2). Here, the only region outside the magnets is between the end of the QD0 magnet and the beginning of the QF1 one. This region will be referred to as the Low Energy Tagger (LET) region. On the other hand, in the region we will refer to as Medium Energy Tagger (MET) region, particles with energy in the 260-330 MeV range impinge on the external side of the beam-pipe (see Fig. 3.3). Finally, the trajectories of the particles arriving at the entrance of the bending magnet are sketched in Fig. 3.4.

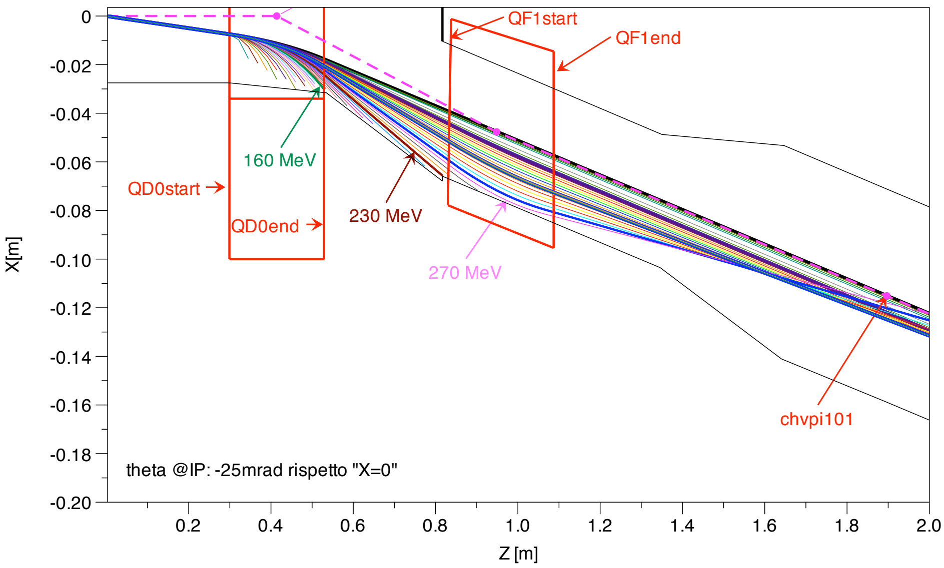


***Figure 3.2:*** *Trajectories of all particles up to* 2 m *away from IP.*

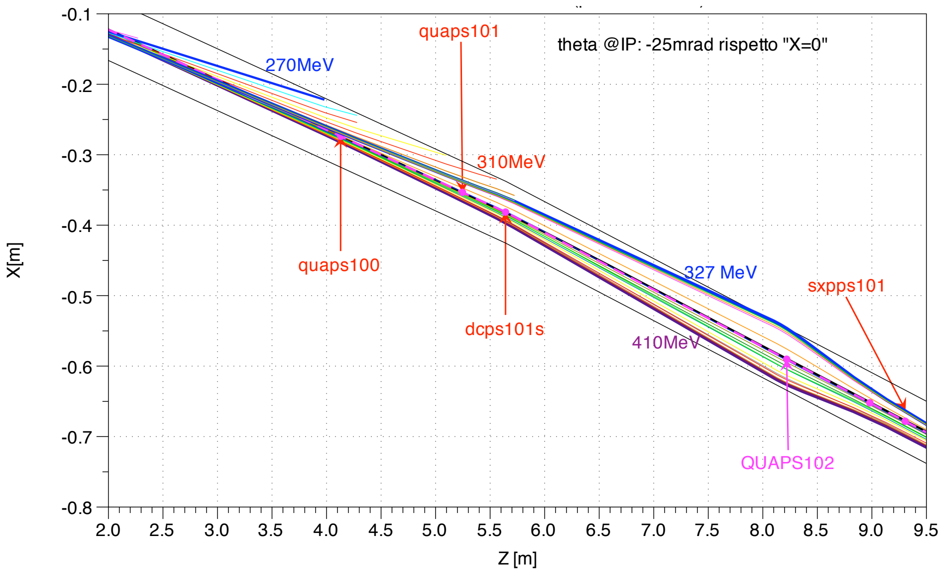


***Figure 3.3:*** *Sketch of the trajectories of particles with energy ranging between 270 MeV and 510 MeV.*

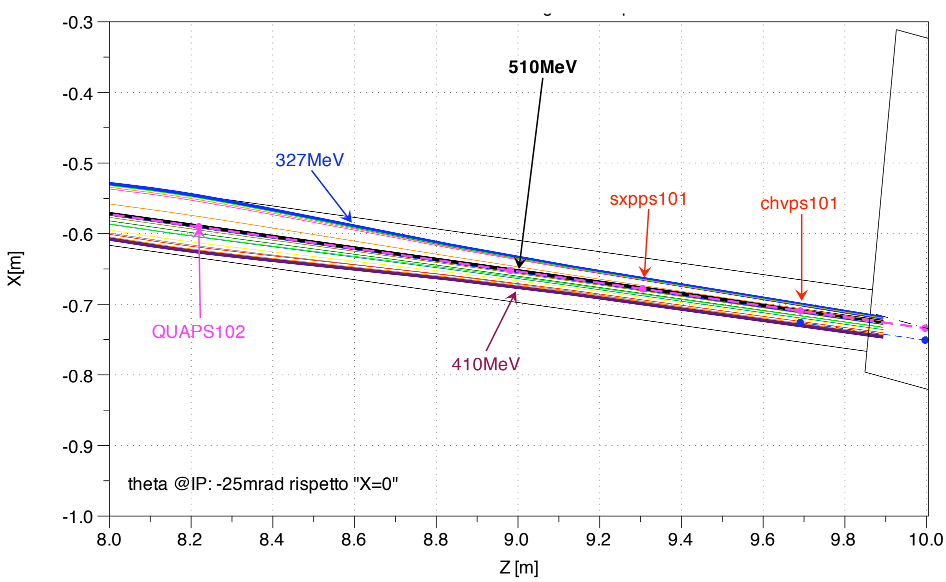


***Figure 3.4:*** *Sketch of the trajectories of particles arriving at the dipole.*

The modelling of the dipole magnet in BDSIM is a critical work, both for the complex geometry of this component and for the fact that BDSIM has been essentially developed to work for linear machines. The main difficulty comes from the positioning of markers inside the dipole (needed for collecting the information to reconstruct the trajectories), due to the fact that the standard plane markers are to be perpendicular to the $z$-axis, while the main geometrical axis of the pipe inside the dipole rotates of $40.5\,^{\circ}$. Two strategies have been followed to realise the dipole magnet model:

- use the standard BDSIM options;
- define a new set of marker elements resulting in a modified version of the code.

The results obtained from the two models are in perfect agreement and this successful comparison allowed us to validate the simulations.
The trajectories of the particles emerging from the dipole are sketched in Fig. (3.5).

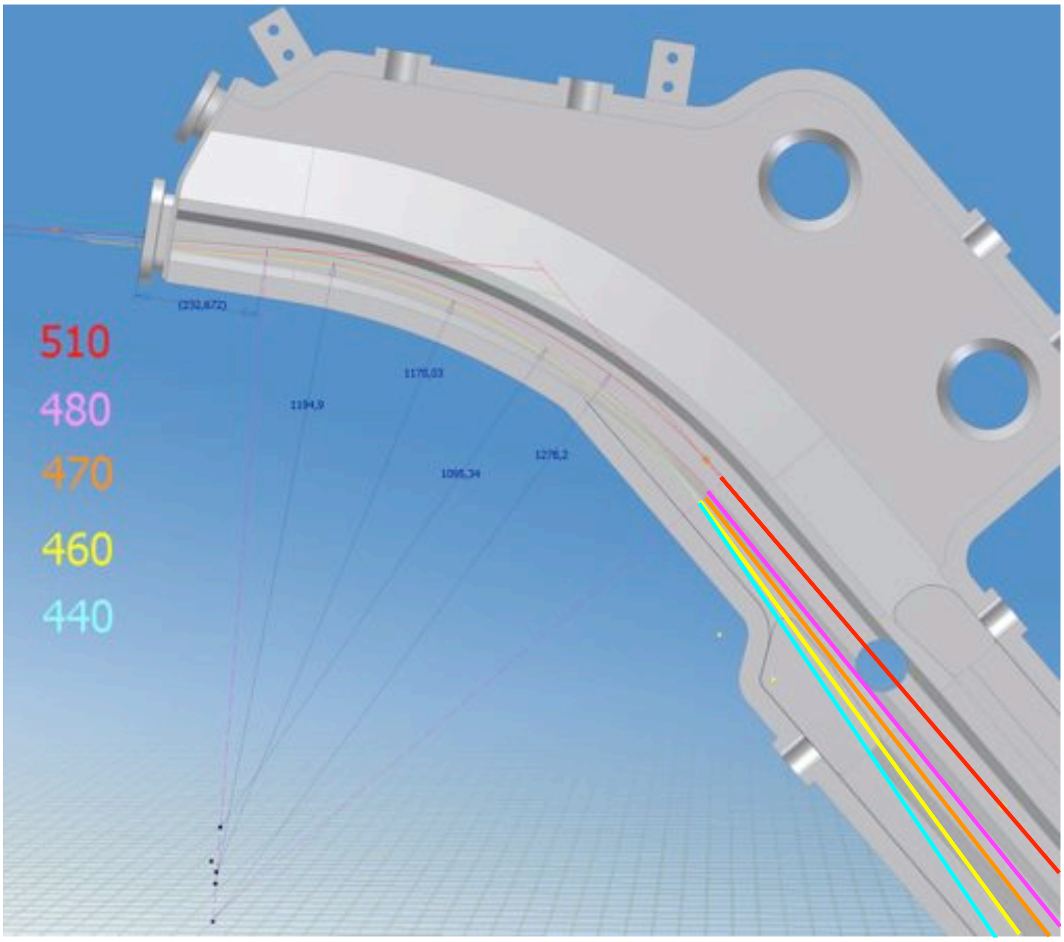


***Figure 3.5:*** *Tracks of off-momentum particles surviving after the dipole (Energy greater than* 430 MeV*).*

In order to build the *lepton tagging system*, we decided to install two detectors per arm (electron and positron): the Low Energy Tagger Detector, placed in the LET region, and the High Energy Tagger detector, placed in the HET region. The task of these devices is to detect off energy leptons and measure their energy.
A Medium Energy Tagger detector could in principle be placed in the MET region, but further studies are necessary both on the physical impact and on the detector hardware itself.

## 3.2 Monte Carlo event generators for $\gamma\gamma$ processes

### 3.2.1 MC event generators for the process: $\gamma\gamma \to \pi^0\pi^0$

In order to generate the signal, we used and compared 3 different Monte Carlo (MC) event generator:

- Courau MC code;
- Nguyen-Piccinini-Polosa (NPP) MC Code;
- TREPS MC code.

In the Courau MC code [27] the reaction is divided into 2 sub-reactions. Firstly each of the two leptons emits a bremsstrahlung photon:

$$e^+e^- \to \gamma\gamma$$

Then the two photons combine together, producing two pions:

$$\gamma\gamma \to \pi^0\pi^0$$

The photon emission is calculated independently for each lepton by an equivalent photon approximation (EPA), in which the intermediate photons are treated as real. For the second sub-reaction we used the two-loop ChPT prediction [10].
In the Nguyen-Piccinini-Polosa MC code [13], the reaction

$$e^+e^- \to e^+e^-\pi^0\pi^0$$

is treated by the 4-body kinematics, with the inclusion of a $\sigma$ particle as a Breit-Wigner resonance.
The last MC code we used is called TREPS [28]. This code is an event generator for two-photon processes at $e^+e^-$ colliders, developed by the Belle collaboration. It uses an EPA in which the virtuality of photons is taken into account.

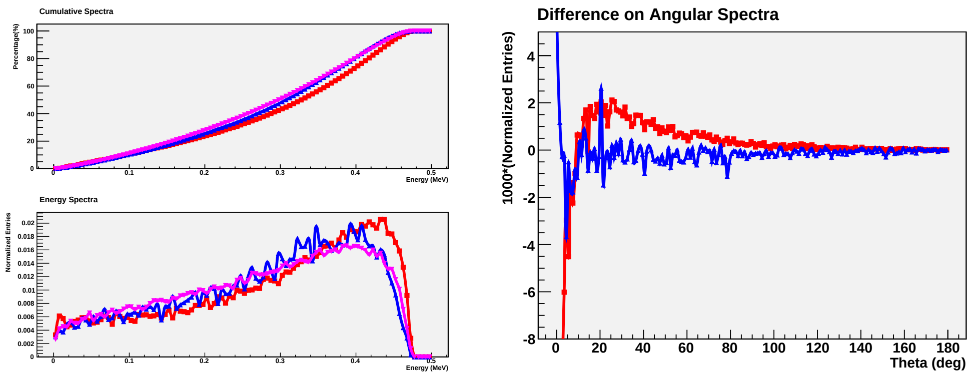


***Figure 3.6:*** *Comparison among the different MC codes used to generate leptons at the IP. On the left the energy (bottom) and cumulative spectra (top) are shown: Courau (red), NPP (blue), TREPS (magenta). The right plot shows with respect to TREPS, the difference in the angular distribution between Courau MC (red) and the NPP MC (blue).*

In Fig. 3.6 the distributions evaluated with the three MC codes are shown. One can notice (left panel) that there is only a slight difference in the energy spectra (bottom) also visible in the cumulative energy spectra (top). The right panel is a vertical zoom of the difference in the angular distribution between the MC codes with respect to TREPS. Although the three MCs use completely different approaches, they disagree, within a few percent, only in the small angle region ($\theta < 1$ deg.).

### 3.2.2 Monte Carlo event generator for the process: $\gamma\gamma \to \pi^0$

In order to study the process $\gamma\gamma \to \pi^0$, the EKHARA[17] Monte Carlo code has been used.
This MC code generates events for two processes:

- $e^+e^- \to e^+e^- + \pi^+\pi^-$
- $e^+e^- \to e^+e^- + \pi^0$

Its main features are the following:

- exact formulae and exact kinematics (in contrast to Equivalent Photon Approximation);

- includes both $s$- and $t$-channel amplitudes and their interference;
- allows user-defined form factors;
- implements specific kinematical cuts;
- accounts for the peaking behaviour of the cross section, in order to have a good Monte Carlo efficiency.

EKHARA is not restricted to the region where the photons are quasi-real, as in the case seen in the previous section for the Courau generator.
The stand-alone EKHARA version works in the centre of mass frame of incident leptons and does not simulate the pion decays. For this reason it had to be modified, to take into account the DAΦNE crossing angle between the incoming beams ($\theta_{e^+e^-} \approx 51.3$ mrad) (see Sec. 1.2.1) and the decay of the $\pi^0$ into two photons.

## 3.3 Preliminary study of leptons reaching the LET and the HET regions

In order to understand what kind of detector was needed in the regions of interest, we performed a more detailed study of lepton energies and momenta:

- we added a particle energy and momentum distribution at the IP using the Courau Monte Carlo generator;
- we tracked particles along DAΦNE lattice using the same simplified layout as before (see Fig. 3.1).

The results of these studies are examined in next subsections.

### 3.3.1 Preliminary study of leptons in the LET region

Considering the results obtained so far, namely particle impinging the beam pipe, shown in figure 3.2 on page 42, one could infer that particles with different energies hit the beam pipe at different positions.
Is this correlation real, or is it due to the simplified initial condition of particle momentum in the tracking procedure?
In order to answer this question, we investigated in more detail the behaviour of the particles by studying the energy and momentum distributions of particles impinging the beam pipe in the LET region. This time, we made use of a momentum distribution at the IP evaluated with the Courau Monte Carlo generator (described in section 3.2.1).

We tracked the generated leptons up to the LET region and studied their energy distribution. We divided the area, onto which leptons hit the wall of the vacuum chamber, in 6 slices along the $z$-axis, each slice being 5 cm long. The results obtained with this procedure are reported in Fig. 3.7. Looking at these plots one can notice that all energy distributions are very wide and do not show any sharp peak. For $z < 80$ cm the distributions are somehow peaked around a value, unfortunately this value is the same for every value of $z$.
In other words, there is essentially no correlation between energy and $z$ coordinate of particles hitting the beam pipe in the LET region.

The reason for this poor correlation can be found by looking at Fig. 3.8, in which we plotted the energy of a lepton versus its polar angle at the interaction point, for particles hitting the vacuum chamber at the same $z$-slices as before.
It is apparent that, also in this case, the two variables are poorly correlated. This results into particles having different energies (thus travelling different paths inside QD0 magnet) ending in the same position in the LET region.

The conclusion drawn from this part of the preliminary tracking, is that this region is well suited for the installation a tagging detector. In order to study $\gamma\gamma$ processes, we need to close the kinematics relations, i.e. we must

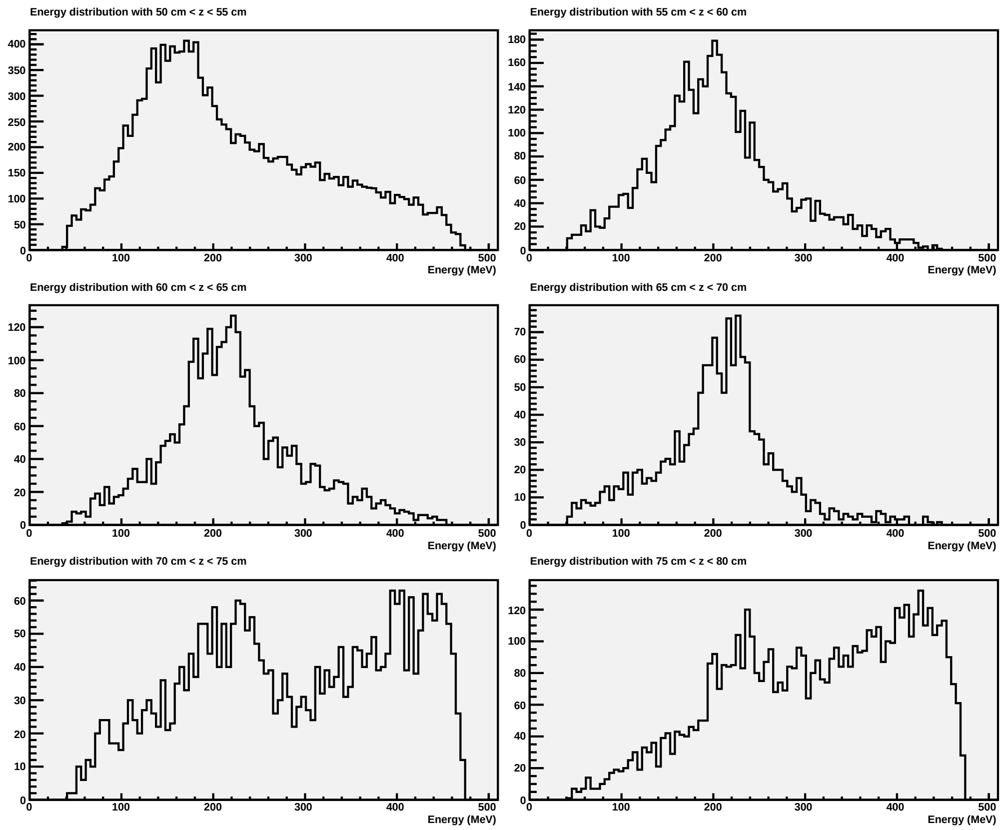


***Figure 3.7:*** *Energy distributions of leptons hitting the beam pipe in the LET region, for different slices along the z-axis.*

know the energy of all the particles participating to the reaction. For this reason, we need to directly measure the energy of detected leptons, therefore the LET detector must be a calorimeter.

Two stations of the LET calorimeter have been built and installed. Details on this detector are beyond the scope of this thesis, nevertheless a general overview has been already given in section 1.3.1.

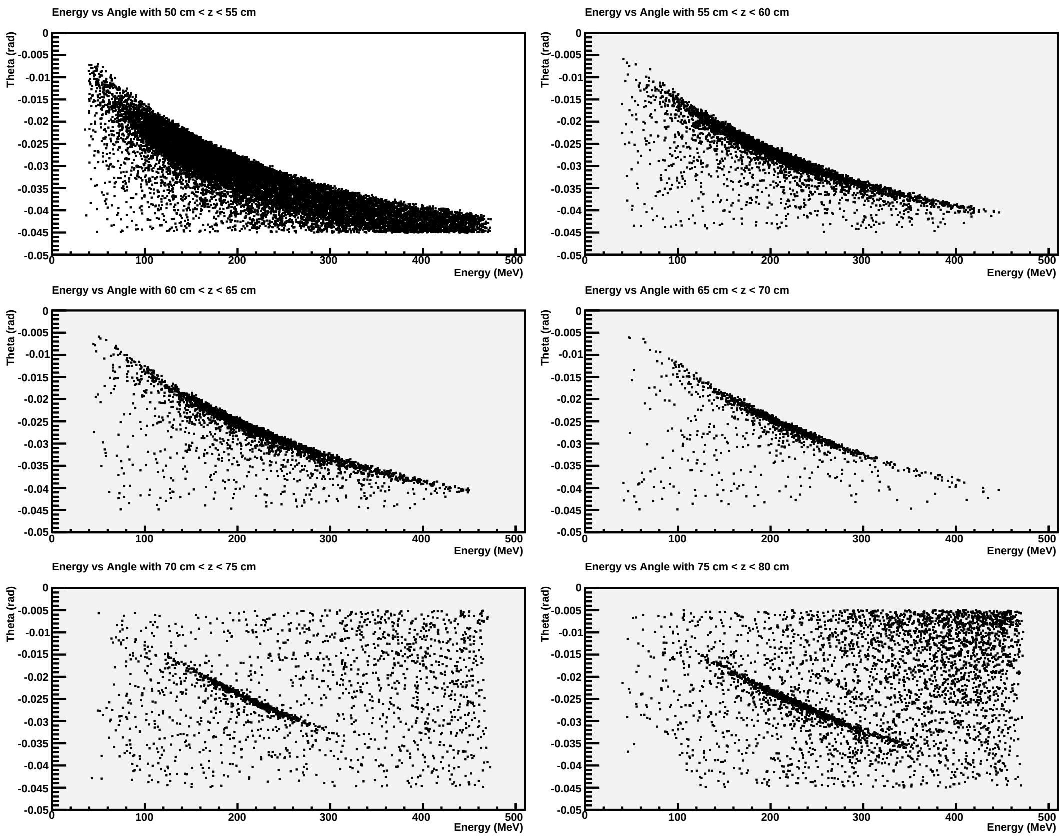


***Figure 3.8:*** *Correlation between the energy of a lepton hitting the beam pipe in the* LET *region and its polar angle $\theta$ at the interaction point (evaluated with Courau MC generator).*

### 3.3.2 Preliminary study of leptons in the HET region

Using the same momentum distribution as in previous section at the IP, we evaluated the tracks of leptons arriving at the exit of the bending dipole magnet, in the HET region.

As previously shown in Fig. 3.5, in this region off-energy leptons do not hit the vacuum chamber wall, but are simply deviated from the main orbit.

Moreover, just at the exit of the dipole magnet, there is a flange through which a position detector can easily access the interior of DAΦNE beam pipe.

In Fig. 3.9 the distance between the tracked lepton and the nominal orbit

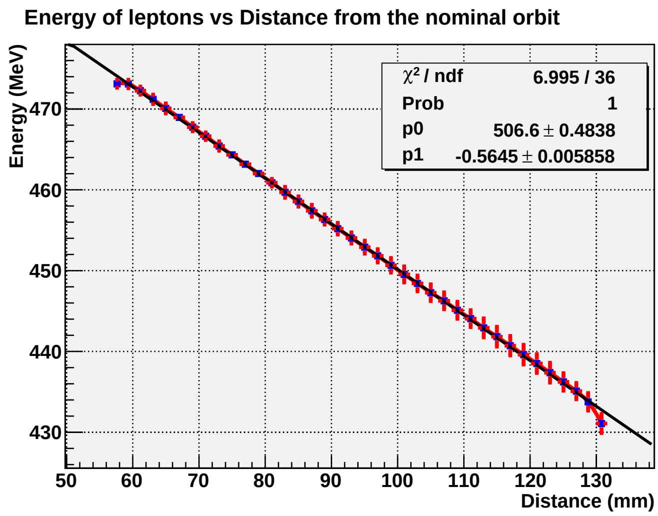


***Figure 3.9:*** *Plot of lepton energy versus their distance from the nominal orbit in the HET region. One can see a strong linear correlation.*

(having an energy of 510 MeV) is plotted as a function of the energy of the particle. Looking at the plot, the linear correlation is striking. Moreover from the fit parameters reported in figure, one can easily calculate that, in order to obtain an energy resolution of about 0.6 MeV, a spatial resolution of 1 mm is sufficient.
What is the cause of this strong correlation between position and energy? The question is more than reasonable, especially if one compares this result to the one obtained in the LET case (see fig. 3.7 on Pag. 49).

In order to answer this question we studied the angular distribution of all leptons generated at the IP (reported in black in Fig. 3.10). Then we selected the leptons reaching the HET region and we plotted their starting angular distribution (same figure in red).
What happens is that, along the path through the vacuum chamber, a copious number of particles gets lost by hitting the beam pipe wall. Those leptons which survive the travel up to the exit of the dipole magnet, are the ones having a narrower angular distribution at the IP. In other words the beam pipe acts as an angular filter, making the situation very propitious for the insertion of a tagging detector in this region.

The presence of the flange just after the dipole, together with the favourable

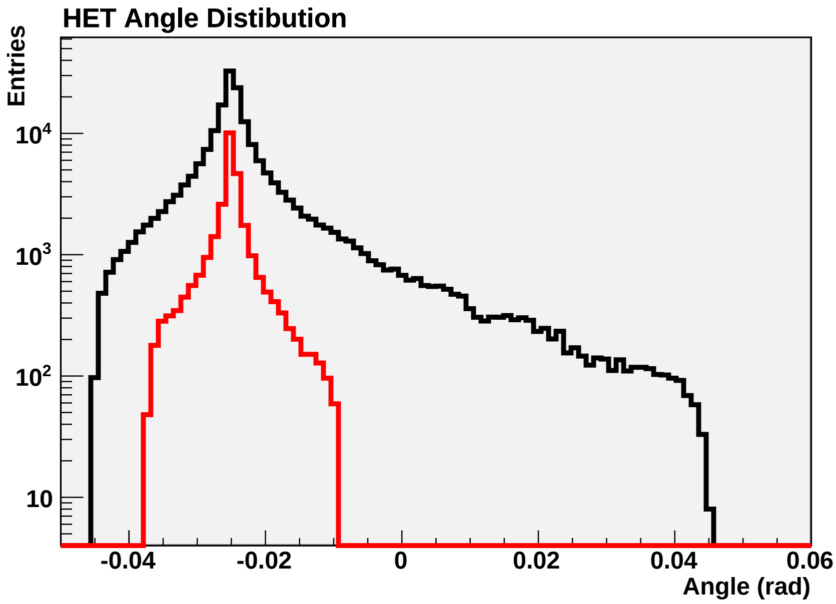


***Figure 3.10:*** *Comparison between lepton angular distribution at the IP (evaluated with Courau MC) for all leptons (black) and leptons arriving at the* HET *region (red). The path through the vacuum chamber narrows the angular distribution of leptons reaching the exit of the dipole magnet.*

lepton displacement in the HET region, made us come to the conclusion that the optimal choice for a second station of the tagging system was to install a position detector here.

A deeper study on particle tracks has been performed with the complete magnetic layout and it is described in next section. The whole chapter 4 is dedicated to the description of HET detector's working principles and design.

## 3.4 Tracking of leptons up to the HET region

The results discussed so far have been obtained in absence of the solenoidal magnetic field of the KLOE detector and compensator permanent magnets. Actually, KLOE detector operates with a magnetic field of nominal central value equal to 0.52 T. The $z$-profile of the field is reported in figure 3.11 as a function of the $z$-coordinate measured in cm.

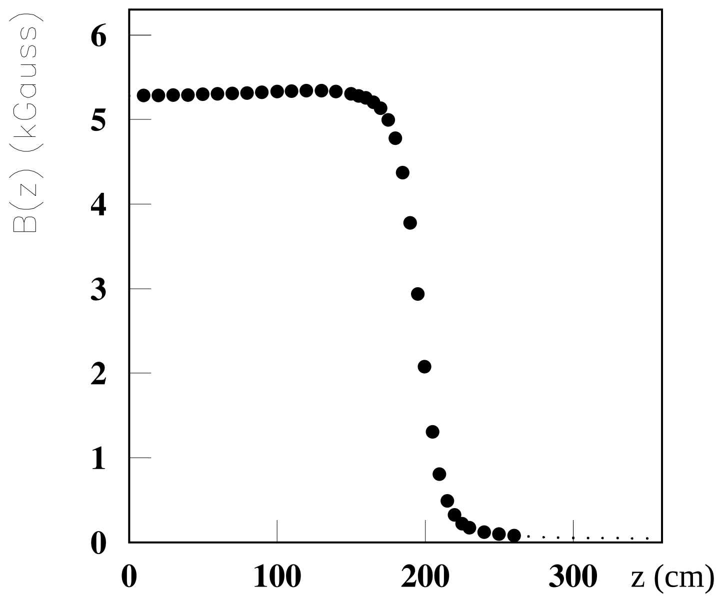


*Figure 3.11: Plot of the z-profile of the magnetic field of KLOE.*

A more detailed tracking of off-energy leptons has been performed, generating particles at the IP by means of the EKHARA code and taking into account the whole present magnetic layout of DAΦNE (see Sec. 1.2.1 for a complete list and description of magnets).
Also in this case, a validation of our tracking procedure was given by the comparison of our results, obtained using BDSIM, with the ones obtained by the accelerator experts using MAD.

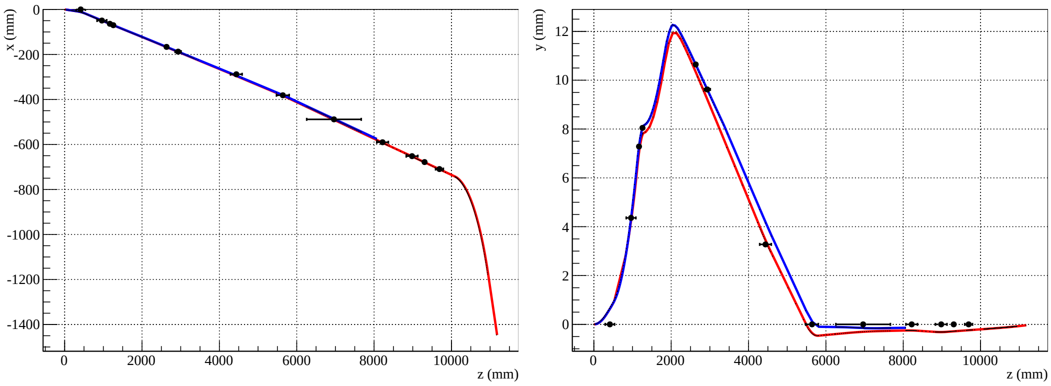


**(a)** Horizontal projection. **(b)** Vertical projection.

***Figure 3.12:*** *Comparison between lepton trajectories calculated with* BDSIM *(red curve) and* MAD *(blue curve). Black dots and horizontal bars respectively represent the centre of DAΦNE magnetic elements (listed in Tab. 1.3 on Pag. 9) and their length.*

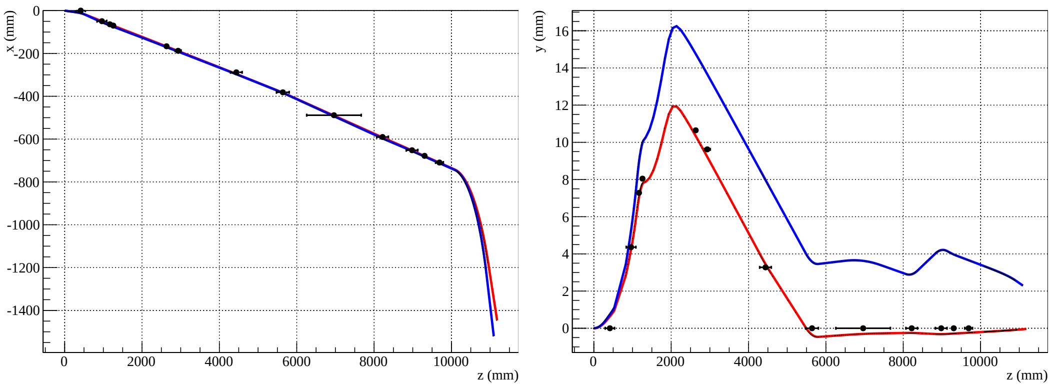


**(a)** Horizontal projection. **(b)** Vertical projection.

***Figure 3.13:*** *Trajectories followed by a* 430 MeV *(blue) and a* 510 MeV *(red) positron, evaluated with* BDSIM. *Black dots and horizontal bars respectively represent the centre of DAΦNE magnetic elements (listed in Tab. 1.3 on Pag. 9) and their length.*

As explained before (Sec. 3.1), this comparison is meaningful only for 510 MeV leptons. The trajectories calculated to this end are reported in Fig. 3.12. MAD trajectories, represented by the blue curves, were provided by accelerator experts and are calculated only for $z < 8$ m, ending just before the focusing quadrupole.

In this figure, one can notice that on the horizontal plane (Fig. 3.12a) the trajectory is mostly straight. On the other hand, on the vertical plane (Fig. 3.12b), the most pronounced curvatures are the ones due to the fringe of the KLOE magnetic field ($z \sim 2.2$ m) and to the kicker magnet ($z \sim 5.7$ m). The difference between the two curves, 0.5 mm at most, is basically due to the thin lens approximation used in MAD. However, accelerator experts agreed on the reliability of our calculation.

After this check, we proceeded to the tracking of off-energy leptons. The energy range taken into account went from 430 MeV up to 510 MeV. Tracking results are reported in Fig. 3.13. Let us examine the lepton displacement for $z \sim 11$ m i.e. in the HET region, in order to understand in detail the dimension needed for the tagging detector.
As far as the vertical projection is concerned (Fig. 3.13b), there is only a difference of about 3 mm between the lowest energy lepton and the nominal one. This means that a detector with a sensitive area 3 mm high is sufficient to contain all the leptons.

The horizontal spread of leptons is, on the contrary critical for the correct functioning of a position detector. From Fig. 3.13a, one can see that the distance between the nominal (red) and the minimum energy lepton (blue) in the HET region is of the order of 10 cm.

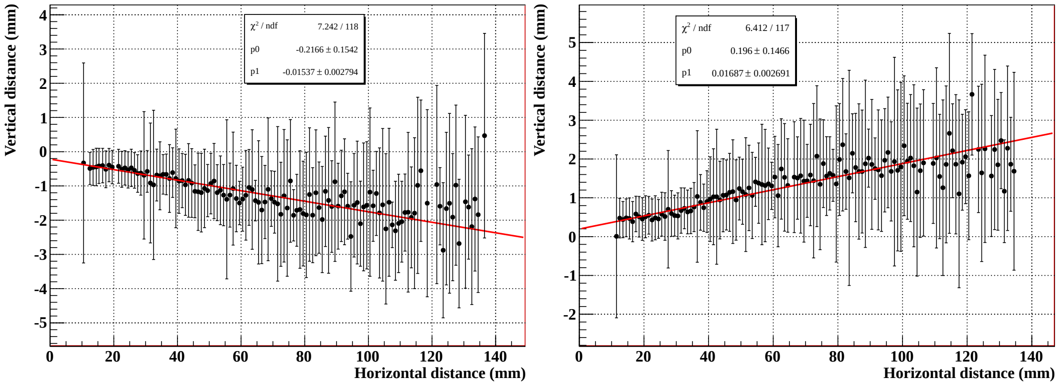


**(a)** Electrons displacement. **(b)** Positrons displacement.

***Figure 3.14:*** *Horizontal and vertical displacement of leptons in the* HET *region, evaluated with* BDSIM *and generated at the IP with* EKHARA. *The error bars are equal to one standard deviation.*

If we fix the $z$-coordinate in the HET region, we can plot the horizontal against the vertical displacement of leptons. In this way, we obtain the distribution of hitting particles on the detector surface. This plot, reported in Fig. 3.14, clearly shows a downward slope for electrons (Fig. 3.14a) and an upward slope for positrons (Fig. 3.14b). By the linear fit parameters $p1$, we know that the slope is around 1.5% in both cases. Thanks to this information, we designed the vertical profile of the HET detector so as to follow the slope of the leptons (see Fig. 4.3 on Pag. 65).

The correlation between lepton energy and distance from the main orbit has also been evaluated and it is reported in Fig. 3.15. These plots confirm the strong correlation we had previously obtained in the preliminary study (see Fig. 3.9 on Pag. 51). From the $p1$ parameter of linear fit performed, we also confirmed the previously obtained energy/distance ratio of about 600 keV/mm.

At last, using the information coming from the tracking of off-energy leptons, we established a procedure to calibrate the HET detector after its installation into DAΦNE. In the following the calibration procedure is ex-

plained.
Leptons have been generated at the IP by means of EKHARA, in the case of single $\pi^0$ production. So the tracked leptons are the ones having participated to the process:

$$e^+e^- \rightarrow e^+e^- + \pi^0.$$

Most of the times (B.R.$\sim$98.8%) the $\pi^0$ decays into two photons which can be detected by the KLOE electromagnetic calorimeter.
We can disentangle processes with a $\pi^0$ in the final state requiring two photons in the EmC with an invariant mass equal to the mass of $\pi^0$ ($m_{\pi^0} \sim 134.9\,\mathrm{MeV}$). If we add the requirement of a coincidence of the two HET stations, we can study the spatial distribution of the leptons hitting the HET detector, obtaining the yellow dots reported in Fig. 3.15.
The minimum value of this distribution is a fixed value because it is bound to the threshold energy of the $\pi^0$ production. In fact, in case of a $\pi^0$ produced at rest, the energy of the two photons (and consequently of the leptons) must be the same. For this reason, this point can be used as a calibration point, corresponding to an energy of about 455 MeV.

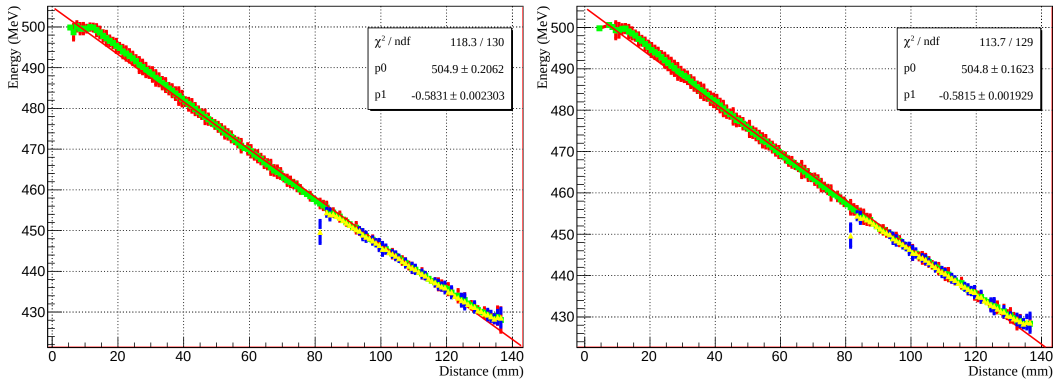


**(a)** Electron calibration line. **(b)** Positron calibration line.

***Figure 3.15:*** *Plot of the* HET *detector energy calibration line for electron and positron stations. Yellow dots (with green error bars) are particles hitting the two* HET *stations in coincidence. Green dots (with red error bars) are all the leptons hitting the detector; The upper tip of the yellow distribution corresponds to the energy threshold of the $\pi^0$ production.*

## 3.5 Study of background events

A process like $e^+e^- \to e^+e^-\gamma$ is referred to as radiative Bhabha scattering and constitutes the main background source for $\gamma\gamma$ physics experiments with tagging facilities, like DAΦNE. Leptons in the initial state emit one photon, thus lose energy and deviate from the nominal orbit. Such an electron or positron is very likely detected by the High Energy Tagger.
Moreover in the case of a double radiative Bhabha scattering ($e^+e^- \to e^+e^-\gamma\gamma$), the two photons in the final state could, in principle, be detected by the KLOE Electromagnetic Calorimeter (EmC) and become a background source for the $\pi^0$ decay. It is worth to remind that the Bhabha scattering cross section, in the angular range under study, is of the order of 100 mb against the ∼100 pb of $\gamma\gamma$ processes.
In order to study these processes we made use of the BabaYaga event generator [29, 30, 31, 32, 33]. This is a Monte Carlo event generator for the processes:

- $e^+e^- \to e^+e^-$ ($\gamma$ or $\gamma\gamma$);

- $e^+e^- \to \mu^+\mu^-$;
- $e^+e^- \to \pi^+\pi^-$;

at flavour factories, i.e. at $e^+e^-$ colliders with an energy in the centre of mass below 12 GeV.

The $\gamma\gamma$ process ($e^+e^- \to e^+e^-\pi^0$) was generated by means of EKHARA and leptons in the final state were tracked up to the HET stations. Background processes, i.e. single and double radiative Bhabha scattering were generated with BabaYaga. In this case as well as tracking $e^+e^-$, the polar angle of photons in the final state was also considered.

Figure 3.16 shows the reconstructed invariant mass of leptons hitting the two station of HET in coincidence[5].

It is apparent that the invariant mass reconstructed from the signal is

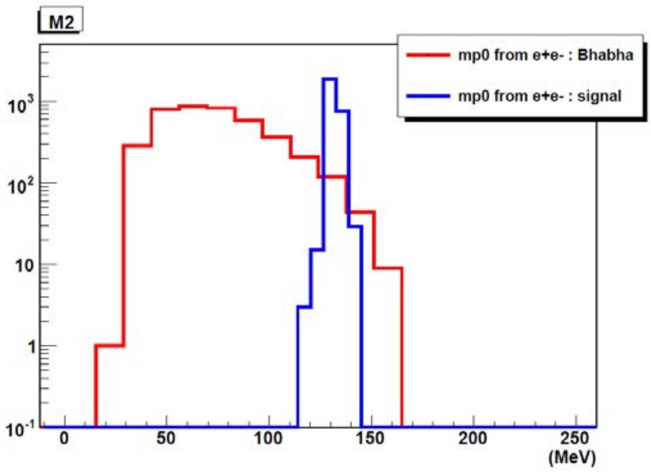


***Figure 3.16:*** *Reconstructed invariant mass of leptons hitting the two HET detectors in coincidence. A $\theta$ = 25 mrad at the IP was assumed. Blue histogram refers to leptons generated by BabaYaga (background), red histogram refers to leptons generated by* EKHARA *(signal). Histograms are not on scale.*

peaked around $m_\pi \simeq 135$ MeV whereas the Bhabha scattering produces a wide distribution at lower values. Nevertheless the tiny signal-to-noise ration (about $6 \times 10^{-7}$), due to the huge difference in the cross sections, prevents the disentanglement of the two processes to be performed with the

[5] Since the HET detector is unable to measure leptons momenta, during the evaluation of the invariant mass, we have assumed a zero angular deviation from the nominal orbit at the IP, i.e. $\theta = \pm 25$ mrad.

information coming from the HET detectors alone.

If we add the requirement of at least one photon in the final state to be detected by KLOE EmC, the disentanglement becomes very simple. In Fig. 3.17, the angular distribution of photons emitted within a Bhabha scattering process is shown in blue. If we require both positron and electron to be detected by the HETS, we obtain the red histogram in the same figure. It is clearly visible that the HET-HET coincidence selects photons almost collinear with the beam ($0° < \theta < 5°$ and $175° < \theta < 180°$) which cannot be detected by the KLOE EmC whose angular acceptance is $25° < \theta < 155°$.

In case of the $\gamma\gamma$ process on the contrary, the two photons coming from

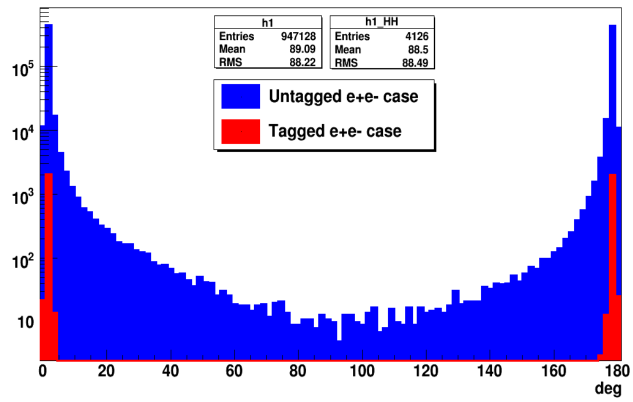


***Figure 3.17:*** *Angular distribution of radiative Bhabha photons with the requirement of both leptons detected by HET (red) and without (blue).*

the decay of the $\pi^0$, produced at rest[6], are emitted back to back almost uniformly in the solid angle (see Fig. 2.7 on Pag. 35).

This difference between the two processes allows us to disentangle signal from background with very high efficiency (almost 100%), simply requiring a photon in the EmC.

[6] As we have seen (see Fig. 2.6 on Pag. 35), the small energy acceptance of the High Energy Taggers, causes the HET-HET coincidence to select pions having very little momentum (less than 30 MeV/c).

## 3.6 Alternative trigger strategies

The KLOE trigger itself requires two energy releases in the EmC in order to assert the first level trigger $T1$ (see Sec. 1.2.3), consequently rejecting a significant percentage of $\gamma\gamma$ events. For this reason, we proposed to modify the trigger strategy by adding the HET-HET coincidence at the $T1$ level.
As an alternative, we planned a strategy that will allow us to acquire $\gamma\gamma \to \pi^0$ events without using the $T1$ signal. In this stand-alone mode, the KLOE acquisition system will provide a new signal $T0$, corresponding to one or more energy releases in the EmC. By means of the HET-HET coincidence plus the new $T0$ signal, we will be able to count out the $\pi^0$ production events, without interfering with regular KLOE data taking.

# Chapter 4

# The High Energy Tagger detector

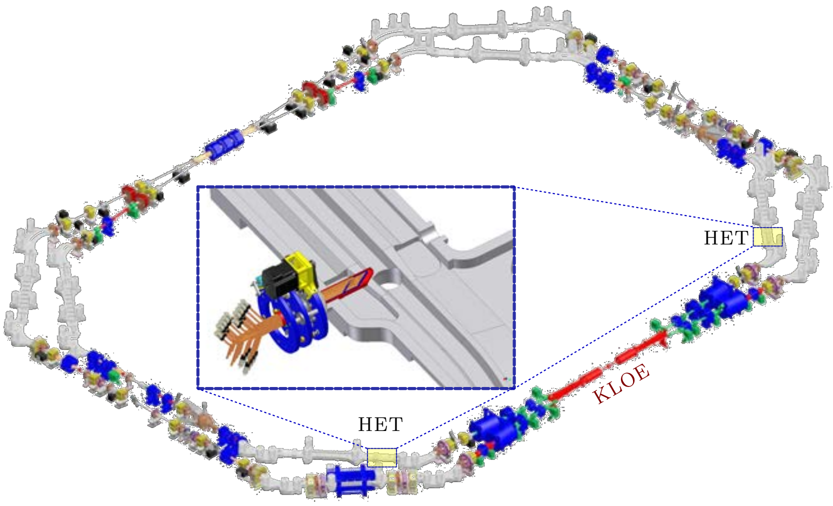


***Figure 4.1:*** *A drawing of the two* HET *detectors placed on DAΦNE lattice.*

The High Energy Tagger (HET) detector is a position detector used for measuring the deviation of leptons from their main orbit. By means of this measurement and of its timing, we are able to disentangle, and therefore to *tag* $\gamma\gamma$ physics events.

Two HET detectors exist on DAΦNE and are placed at the exit of the dipole magnets (see Fig. 4.1), 11 m away from the IP, both on positron and electron arm.
In this chapter the design of the active area, of the light sensor, and of the mechanical structure of the HET detector is discussed.

## 4.1 Design of the HET detector

The sensitive area of the HET detector is made up of a set of 28 plastic scintillators (see picture in Fig. 4.2). The dimensions of each of them are $3\,\mathrm{mm} \times 5\,\mathrm{mm} \times 6\,\mathrm{mm}$.
One additional scintillator, of dimensions: $3\,\mathrm{mm} \times 50\,\mathrm{mm} \times 6\,\mathrm{mm}$ (referred

***Figure 4.2:*** *A picture of the HET plastic scintillators. At the top right there is a set of long scintillators.*

to as *long* scinitillator), is used for coincidence purposes.
A more detailed description of these scintillators is given in section 4.1.1.
The light emitted by each of the 28 scintillators is carried out through a clear plastic light guide.

The 28 scintillators are placed at different distances from the beam-line, in such a way that the measure of the distance, between the hitting particle and the beam, can be performed simply knowing which scintillator has fired.

On the vertical plane (see Fig. 4.3), the scintillators are aligned, with the

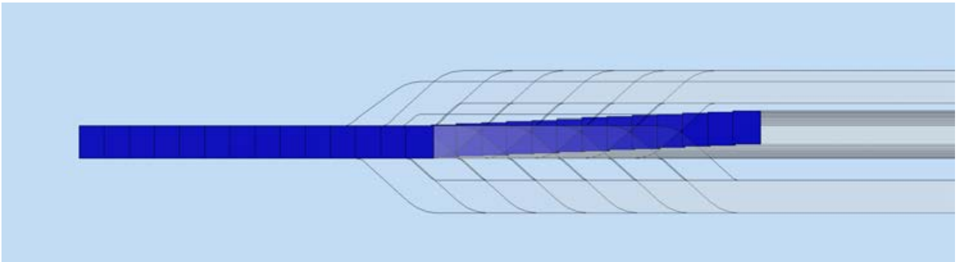

*Figure 4.3: A drawing of the vertical profile of the HET scintillators (blue) with their light guides (transparent). The beam line is on the left of the drawing. One can notice the vertical curvature used to follow the impinging position of the leptons, positrons in this case.*

exception of a slight curvature at big distance from the beam. They show their $5\,\mathrm{mm} \times 6\,\mathrm{mm}$ face to the impinging particles that go through them along the thickness of 3 mm. The scintillators are not placed side by side, on the contrary there is an overlap of 0.5 mm on the 5 mm side.

In the horizontal plane, the scintillators are arranged in a two-staircase

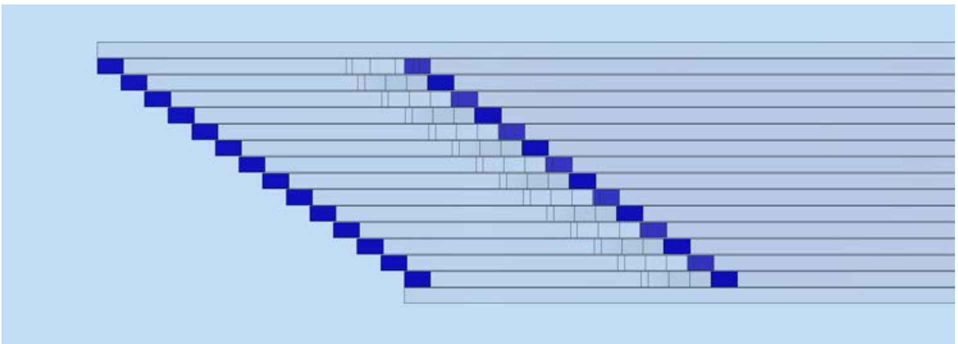

*Figure 4.4: A drawing of the horizontal profile of the HET scintillators (blue) with their light guides (transparent). The beam line is on the left of the drawing.*

fashion, shown in Fig. 4.4. This is done in order to make room for the light

guides connecting every scintillator with the outside. Each light guide is connected to the 3 mm × 6 mm face of a scintillator. The connection is made with an optical glue, with the same refraction index as the guide. Every system of guide and scintillator is wrapped with an aluminium foil about 100 $\mu$m thick, in order to reduce light dispersion and avoid the light emitted by a scintillator to scatter into the surrounding guides and produce a crosstalk signal. While the light guides connected to the internal (far from the beam) staircase of scintillators, run straight, the ones connecting the external set of scintillators are bent. The bending, performed on the vertical plane, allows the guides to dodge the internal scintillators and reach the outside.
Once outside, all the guides are bent and coupled to the light sensors (see Fig. 4.6), the Hamamatsu R9880U-110 SEL Photomultipliers (PMT). A more specific description of these sensors is given in section 4.1.2. These devices are shaped as cylinders of 16.0 mm of radius, and 12.4 mm of height. They have an active area of 50.3 mm$^2$ shaped as a circle of 8.0 mm of diameter (see Fig. 4.5). On the bottom face of the cylinders, there are 12 electrical pins used to connect the device to its socket. The coupling between light

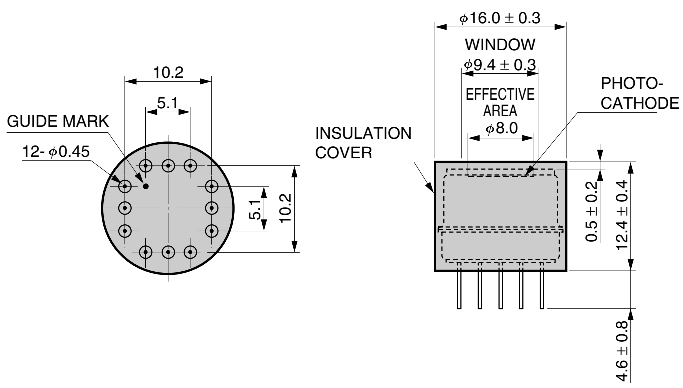


***Figure 4.5:*** *A mechanical drawing with dimensions of a horizontal (left) and vertical (right) section of the Hamamatsu R9880U-110 SEL photomultipliers.*

guide and PMT is performed through an optical pad, i.e. a soft foil, 1 mm thick, having the same refractive index as the light guide. The optical pad is shaped as a circle of 9 mm of diameter, i.e. slightly wider than the active area of the PMT. The latter is pushed toward the optical pad and kept adherent by a spring. On their external face, the PMT are connected to their voltage dividers. These passive devices are sockets for the 12 pins of the photomultipliers. They are shaped as cylinders with a diameter of 17.5 mm and have three connection cables on their external faces: high voltage (HV), output signal, and ground.

All the system (tip of the light guide, optical pad, PMT, socket and spring)

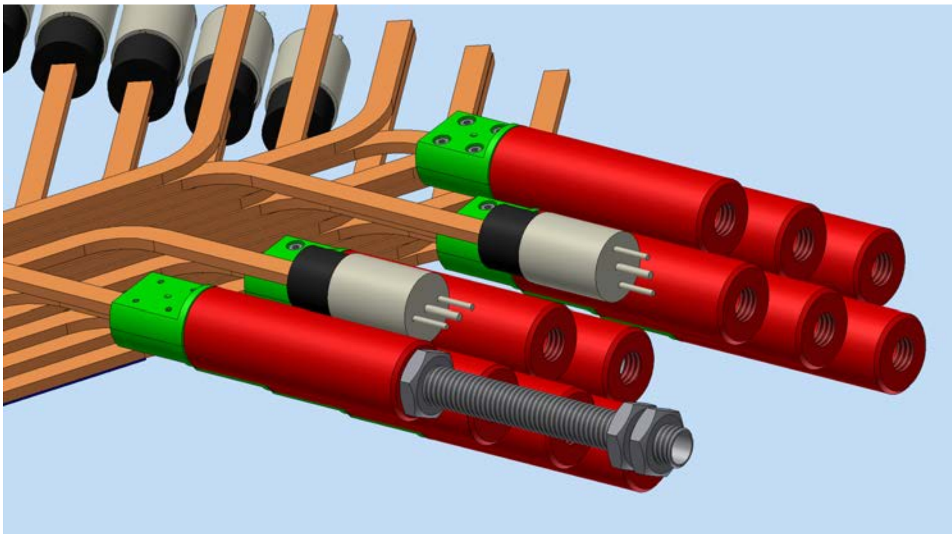

***Figure 4.6:*** *A drawing of the external tip of the HET light guides (orange), photomultipliers (black) coupled with their socket (grey). The whole system is contained in a cylindrical aluminium box (red) fixed to the guide thanks to a plastic holder (green).*

is enclosed in a cylindrical aluminium box, drawn in Fig. 4.6, hold by a hollow screw fixed to an external plate not drawn in figure. On the internal face of the aluminium cylinder, a 100 $\mu$m thick $\mu$-metal foil is placed, in order to shield the PMT from external magnetic field. The plastic holder, drawn in green in figure, also hosts an optical fibre whose tip is adherent to the light guide. Light pulses, generated by a LED during the PMTs calibration procedure (described in Sec. 5.3), reach the PMT travelling through this fibre. The three cables, coming out from the PMT socket, are routed inside the hollow screw, up to the HV system (see sec. 5.3) and to the front-end electronics (described in sec. 5.1.1).

### 4.1.1 EJ-228 plastic scintillators

The EJ-228 is a premium plastic scintillator produced by Eljen Technology. It is intended for use in ultra-fast timing and ultra-fast counting applications and it is recommended for use in small sizes (any dimension less than 100 mm). The EJ-228 scintillator is composed of Polyvinyltoluene and has a density of 1.023 g/cm$^3$ and a refractive index of 1.58.
In table 4.1 a list of its main scintillation parameters is reported.

| Parameter | Value |
|---|---|
| Wavelength of max emission | 391 nm |
| Rise time | 0.5 ns |
| Decay time | 1.4 ns |
| Pulse width | 1.2 ns |

***Table 4.1:*** *Scintillation parameters of the EJ-228 plastic scintillator.*

In Fig. 4.7 light emission spectrum of the scintillator is reported.

***Figure 4.7:*** *In the plot on the left, the light emission spectrum of EJ-228 is reported. In the plot on the right, its particle response is plotted as a function of the particle energy.*

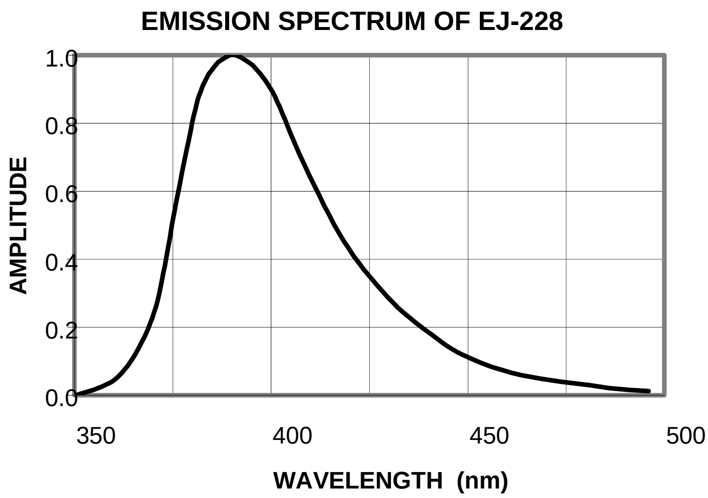

### 4.1.2 Hamamatsu R9880U-110 SEL photomultipliers

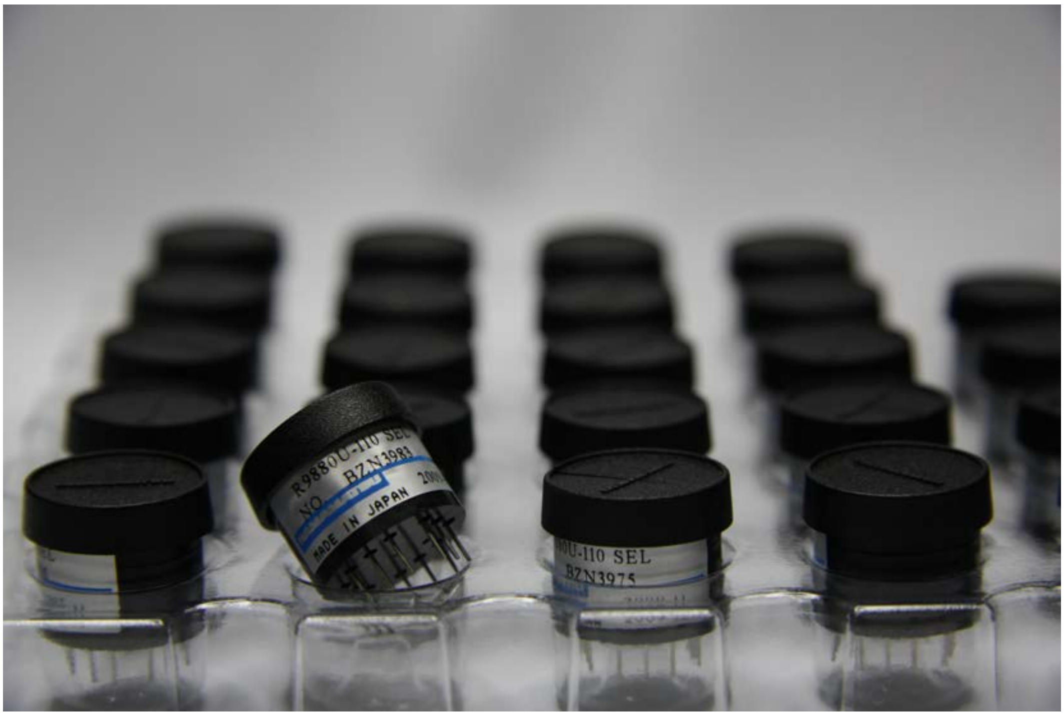


***Figure 4.8:*** *A picture of the HET Hamamatsu R9880U-110 SEL photomultipliers.*

R9880U-110 SEL (Fig. 4.8) is a compact size and high quantum efficiency photomultiplier produced by Hamamatsu Photonics K.K. Its main characteristics are plotted in Fig. 4.9. From the plot on the left, one can see that its quantum efficiency is about 35% for a wavelength going from 300 nm to 400 nm. This value greatly fits EJ-228 emission wavelength that is peaked around 391 nm.
Since the small dimensions of the scintillator in use, the total light yield, due to a crossing electron or positron, is quite small. For this reason, we chose such a high quantum efficiency photomultiplier in order to minimise the probability of a particle, which crosses the scintillator, to go undetected.

A preliminary study of the photomultiplier output signal has been performed. A PMT coupled with a EJ-228 was put under test by means of a $^{90}$Sr

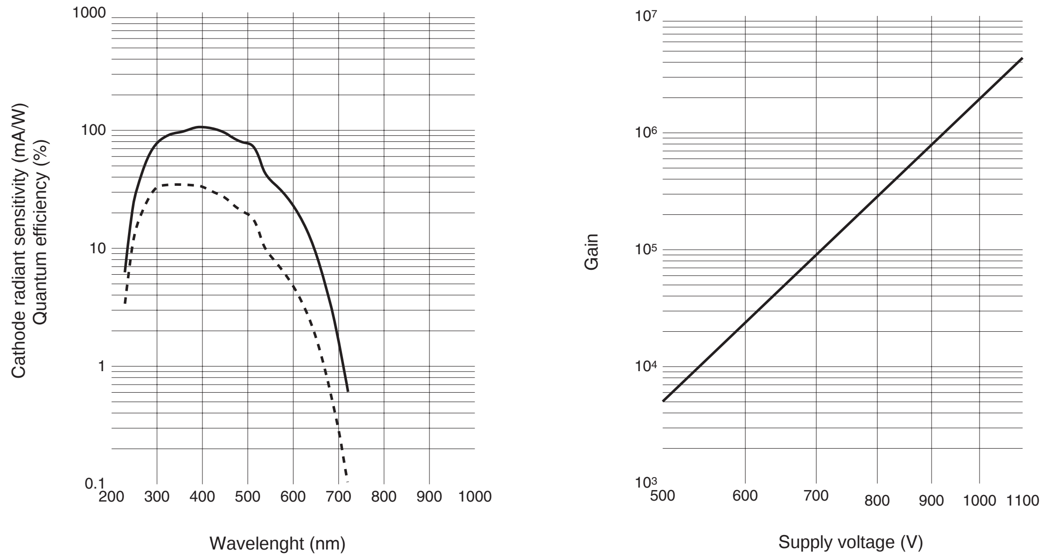


***Figure 4.9:*** *Hamamatsu R9880U-110 SEL photomultiplier characteristics. On the left the quantum efficiency (dashes) and the cathode radiant sensitivity (solid) are plotted as a function of the incoming radiation wavelength. On the right the gain is plotted as a function of the high voltage.*

radioactive source. Strontium decays into Yttrium through the $\beta^-$ process $^{90}\mathrm{Sr} \rightarrow {}^{90}\mathrm{Y}+e^- + \bar{\nu}$, emitting electrons with an energy distribution mostly peaked around 300 keV.

The output signal was acquired by an oscilloscope with and without the radioactive source. The results of this study are shown in Fig. 4.10. In sub-figure 4.10a the output signal waveform is shown. The typical signal amplitude is between 200 mV and 700 mV, its rise time is about 2 ns and the amplitude of after-signal ripples is always less than 100 mV.

The results of the same test performed without any particle source is reported in sub-figure 4.10b. One can notice that the waveform of the signal is very similar while its amplitude rarely exceeds 40 mV. All this information is essential for the design of the HET front-end electronics described in section 5.1.

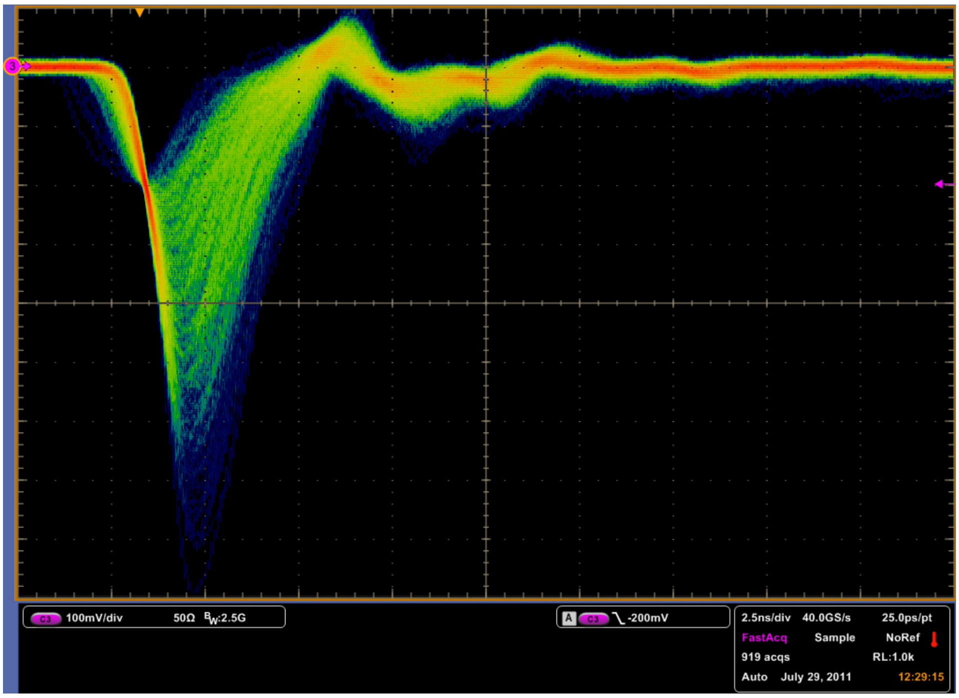


**(a)** PMT signal: horizontal scale 2.5 ns/div, vertical scale 100 mV/div.

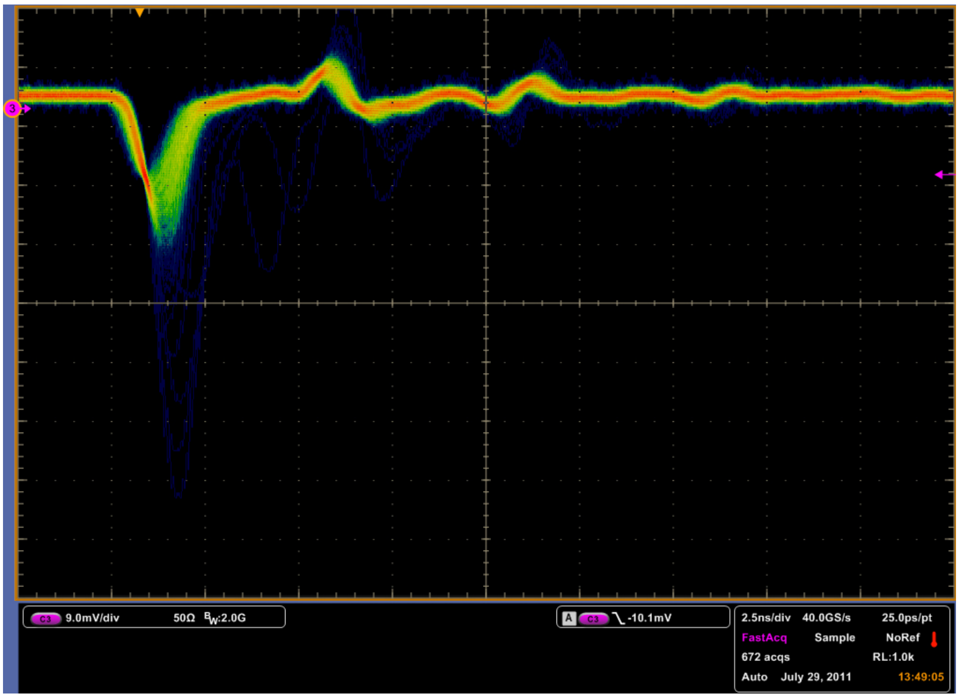


**(b)** PMT noise: horizontal scale 2.5 ns/div, vertical scale 9 mV/div.

***Figure 4.10:*** *Waveforms of R9880U-110 SEL photomultiplier (coupled with scintillator and light guide) signal and noise. Signal is obtained with* ~300 keV *electrons.*

## 4.2 The HET detector assembly

In this section, we will briefly describe the assembly procedure of the HET detector.
The first part of the procedure consisted of bending all the light guides and glueing them to the scintillators. Subsequently, the guides plus the scintillators have been wrapped with aluminium foils.
Then all the guides have been assembled together and kept adherent by means of specific plastic supports. In the picture in figure 4.11, the external edge of the assembled HET detector is visible.

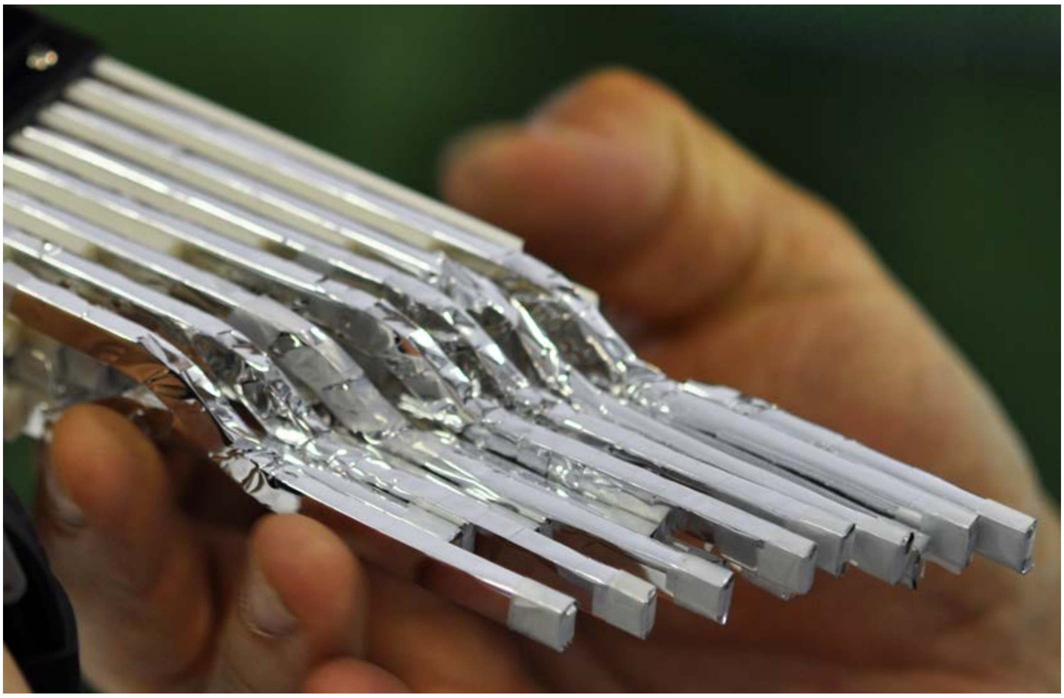

***Figure 4.11:*** *A picture of the sensitive area of the HET detector, taken during assembly. In this picture, scintillators had not been properly aligned yet.*

Afterwards, the photomultipliers were applied to the tip of the guides thanks to the cylindrical aluminium boxes and the plastic holders (described in Sec. 4.1). In figure 4.12, the assembled detector is shown. Once all the cables (signal, HV, optical fibres) were properly connected, the whole external part of the detector was enclosed inside an aluminium case (shown in Fig.

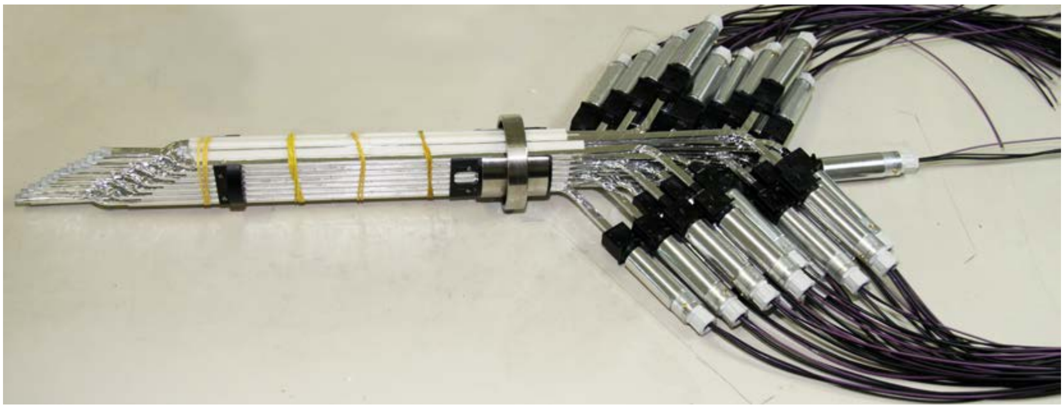

***Figure 4.12:*** *A picture of* HET *detector assembled with the photomultipliers.*

4.13). The case is used both as a shield for external electromagnetic fields and to avoid the external light to be detected by photomultipliers. On the external surface of the aluminium case, one can see two smaller brass cases, which are used to enclose the HET front-end boards (see Sec. 5.1.1). The high voltage connectors are located on the aluminium case. The low voltage connectors, together with all the output-signal SMA and LEMO connectors, are located on the external surface of the brass cases.

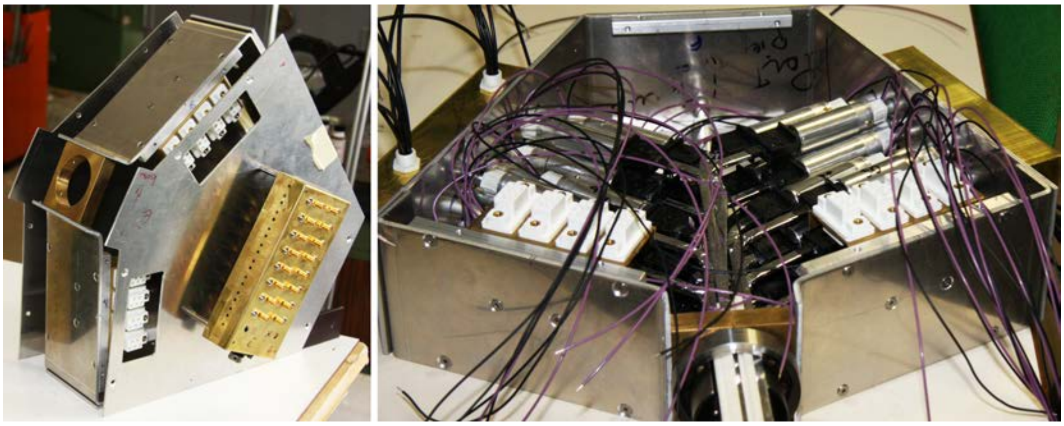

***Figure 4.13:*** *On the left, a picture of the external aluminium case of the* HET *detector. On the right, a picture of the detector assembled with PMTs enclosed in the case.*

## 4.3 The HET mechanical structure

The task of the HET is to detect particles travelling some centimetres away from the beam, just after the dipole magnet. Nevertheless, since it is too difficult to handle a detector placed inside the vacuum chamber, the HET detector is placed in air. For this reason, the beam pipe, just at the exit of the dipole magnet, had to be properly shaped to host the sensitive area of the detector. A mechanical vacuum proof system, made of a steel bellows

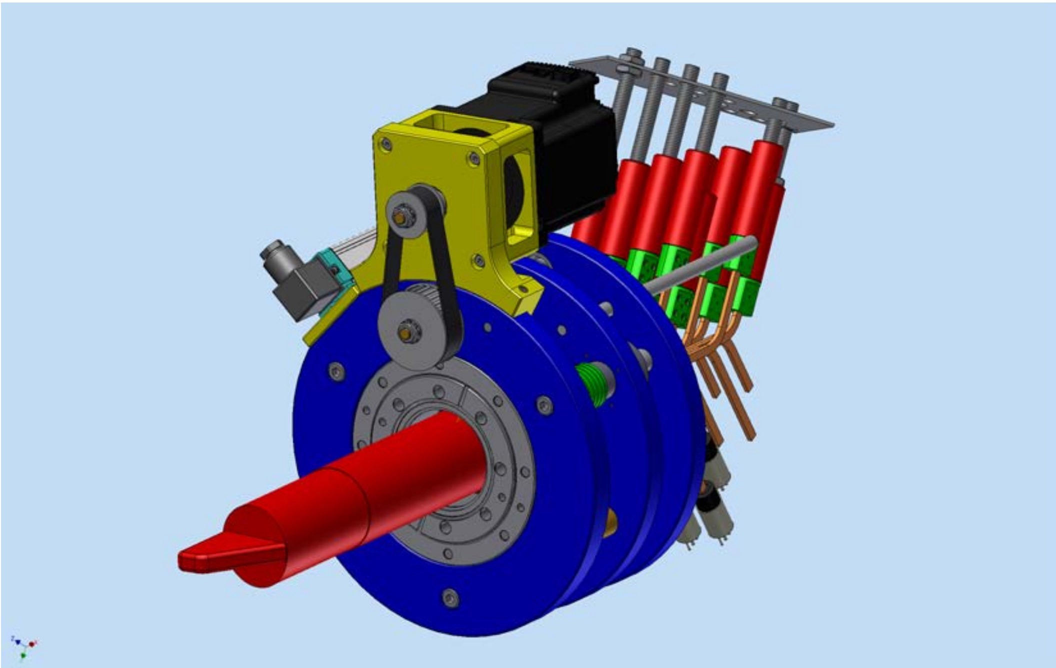

***Figure 4.14:*** *A drawing of the HET mechanical system.*

and Roman pot[1] has been realised. The bellows is secured on one edge to the beam pipe and on the other to the Roman pot. On both edges a vacuum flange is used to seal the bellows. Thanks to the bellows, a step motor is enough to shift the Roman pot back and forth and put it close to the beam or far from it. An approaching of the Roman pot towards the beam can change

[1]The Roman pot is the name of a technique (and of the relevant device) used in accelerator physics to detect particles at very small angle. It was named after its implementation by the CERN Rome group in the early 1970s.

the impedance of the machine. For this reason the detector can be pushed next to the beam only once the beam tuning operations are completed. In any case, according to DAΦNE experts, the distance occurring between the edge of the Roman pot and the beam-line cannot be less than 30 mm.

## 4.4 HET detector insertion into DAΦNE beam-pipe

After the assembly phase, the two HET detectors were moved to DAΦNE hall and inserted into their mechanical system, which had been previously installed onto the beam-pipe. In figure 4.15, three pictures, taken during the insertion are shown.

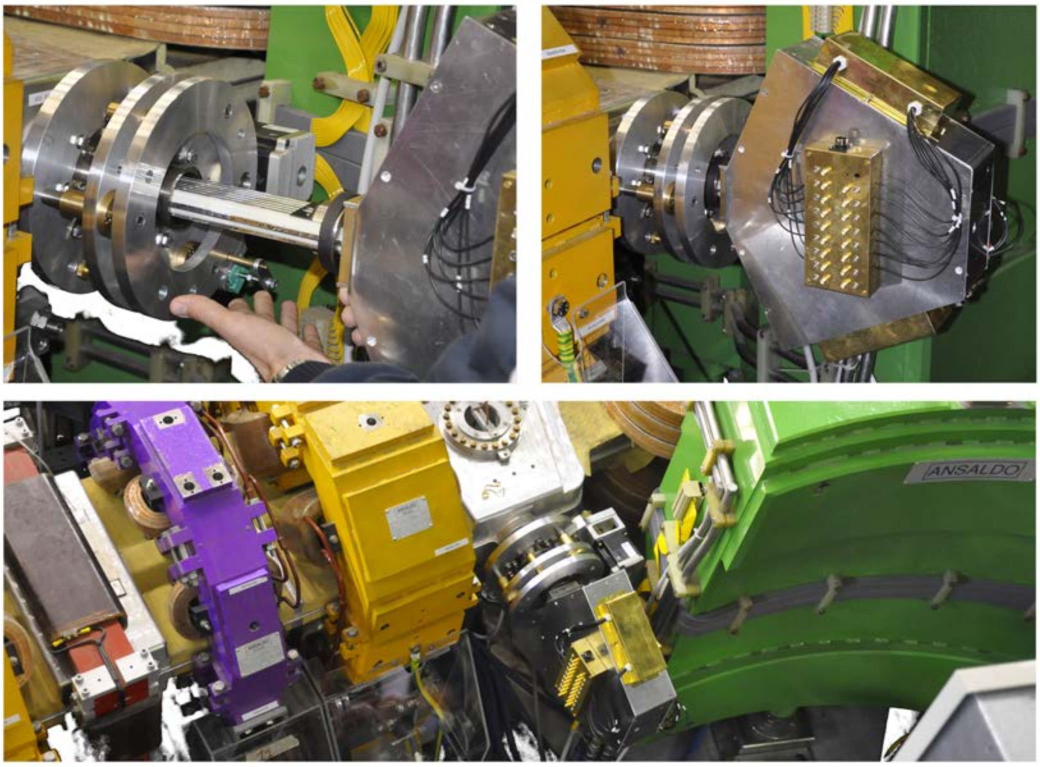


***Figure 4.15:*** *Three pictures taken during the HET detector insertion. In the picture on the bottom, one can see (from right to left): the big bending dipole (green), the plugged HET detector, a quadrupole magnet (yellow) and a crab-waist sextupole magnet (violet).*

## 4.5 HET detector test beam

At the DAΦNE Beam Test Facility (BTF) of Laboratori Nazionali di Frascati, a test of the sensitive area of the HET detector has been performed.
The BTF is capable to provide bunches containing a known number of electrons or positrons. The energy of the leptons provided by the facility is also tunable.
The proper functioning of scintillators coupled with light guides read out trough photomultipliers was tested, thanks to single 500 MeV electrons.
The main purpose of this test was to check the time jitter of the detecting system of scintillators and sensors[2], that is critical for the global time precision of the detector.

### 4.5.1 Test beam setup

We installed, in front of the beam, a set of 3 EJ-228 scintillators (see section 4.1) and a BGO[3] crystal (used for checking the beam energy) in the following order, starting from the beam side (see Fig. 4.16):

1. a normal scintillator $3\,\text{mm} \times 5\,\text{mm} \times 6\,\text{mm}$;
2. a normal scintillator $3\,\text{mm} \times 5\,\text{mm} \times 6\,\text{mm}$;
3. a *long* scintillator ($3\,\text{mm} \times 50\,\text{mm} \times 6\,\text{mm}$);
4. a BGO crystal.

The three EJ-228 scintillators were coupled with a plastic light guide and read out with three `R9880U-110 SEL` photomultipliers. The glue used to couple scintillators and guides, together with the optical pad used to couple guides and PMTs were the same as in the final design of the HET detector.

[2]Namely the variation of delay between the time of arrival of a particle onto the scintillator and the generation of the output signal.

[3]BGO is a bismuth germanate ($Bi_4(GeO_4)_3$) is an inorganic chemical compound used as electromagnetic calorimeter.

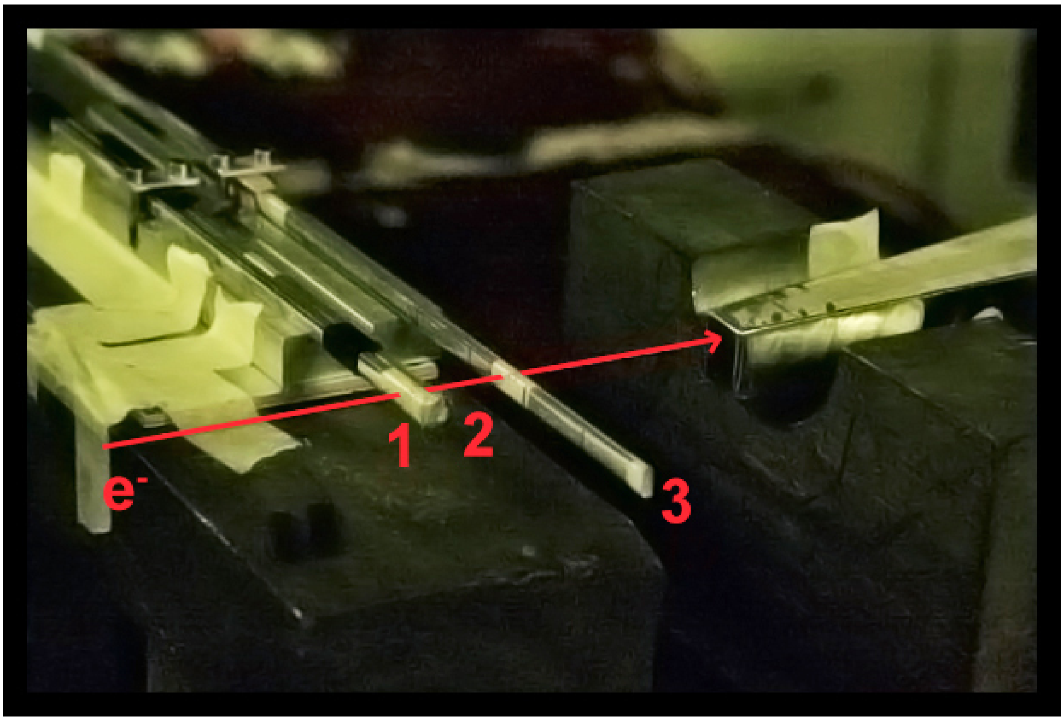


***Figure 4.16:*** *A photograph of the* HET *test beam setup. The red arrow indicates electron beam. Scintillators and light guide are visible, wrapped with an aluminium foil. On the right one can see the edge of the BGO crystal.*

In order to check the time jitter of the system under test, we made use of a CAEN V775N TDC module. All signals coming out from the PMTs were discriminated (with a standard single threshold discriminator) and their digital outputs connected to the TDC. The output of the long scintillator was used as a *start* signal for the TDC, and with respect to it, the times of arrival of the two small scintillator signals ($t_1$ and $t_2$) were stored.
Along the beam direction, the two small scintillators are 3 mm long and are placed one close to the other. In this way, the time jitter due to the change of the length of the path through the scintillators is negligible ($\sim 1$ ps).
The time jitter due to scintillators and PMTs is simply the standard deviation of the distribution of the $t_2 - t_1$ values.

### 4.5.2 Test beam results

As we said, we acquired the distribution of the difference $t_2 - t_1$. In principle, its mean value should be of a few picoseconds, because the scintillators are located at 5 mm one from each other. Nevertheless, as one can see in figures 4.17 and 4.18, the mean value is much greater than that. This is only due to a different length of cables connecting the two scintillators and does not affect our measurement.
We performed the measure described above for different conditions:

1. with a bent light guide;
2. with an external steel box containing the scintillators;
3. with an electronic splitter.

The results of the measurements obtained with the condition 1 and 2 are reported in Fig. 4.17.

In both cases the standard deviation evaluated by the Gaussian fit is:

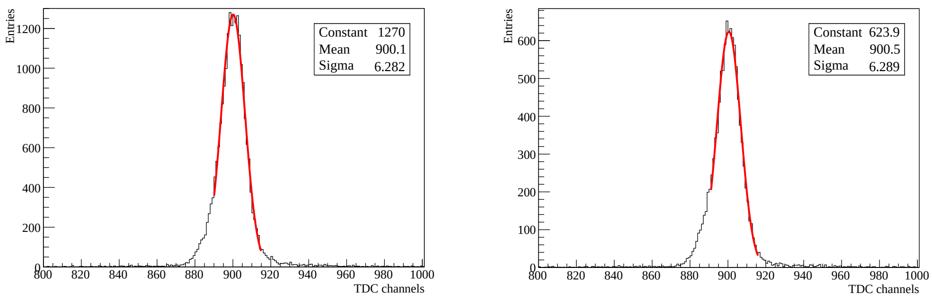


**(a)** TDC spectrum with bent light guide. **(b)** TDC spectrum with steel box.

***Figure 4.17:*** *Time distributions resulting from the measurement of the difference $t_2 - t_1$ with bent light guide and steel box. One TDC channel is equal to 34.2 ps.*

$\sigma_{TDC} \simeq 6.3$ TDC channels, so the introduction of a steel box does not affect the time measurement. We configured the TDC module, in such a way that a channel corresponded to 34.2 ps, so total standard deviation is:

$$\sigma_{TOT} = \sigma_{TDC} \cdot 34.2\,\text{ps} = 215.5\,\text{ps}.$$

The measure was performed with 2 plastic scintillators and PMTs, thus we can write:

$$\sigma_{TOT} = \sqrt{\sigma_1^2 + \sigma_2^2}.$$

Assuming that the two systems are identical, i.e. $\sigma_1 = \sigma_2 = \sigma$:

$$\sigma = \frac{\sigma_{TOT}}{\sqrt{2}}.$$

Therefore the time jitter due to the system, made of scintillator plus PMT, is equal to: $\sigma \simeq 153\,\text{ps}$.
In condition 3, we added an electronic splitter, equipped with the same buffer as the HET front-end board (see section 5.1.1). The insertion of this device caused a slight signal corruption. The time distribution obtained with this configuration is shown in Fig. 4.18. In this case $\sigma_{TDC} = 9.2$ TDC channels, leading to $\sigma \simeq 222\,\text{ps}$.

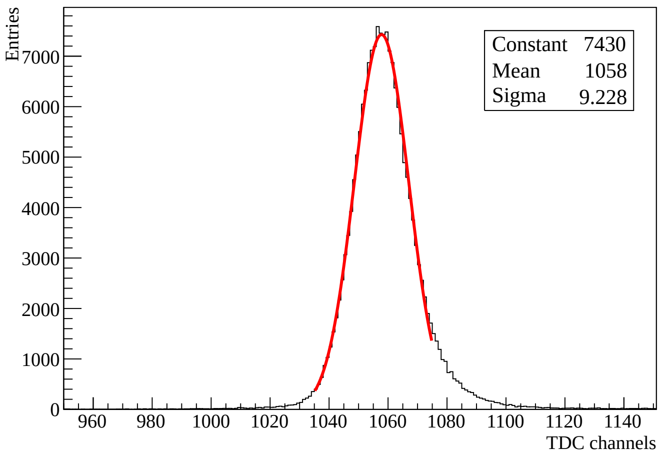


*Figure 4.18: Time distributions resulting from the measurement of the difference $t_2 - t_1$ with electronic splitter. One TDC channel is equal to* 34.2 ps.

Moreover, we studied the amplitude of the output signals, in order to monitor a possible signal degradation in the various configurations listed above.
We amplified the PMT output signals of about a factor 5 and connected

them to a CAEN `V792N` QDC[4] module (the same used in the slow control system, see Sec. 5.3). The acquired QDC spectra are shown in Fig. 4.19.
We were concerned about a possible reduction of the signal amplitude. This would result into a shift of the QDC peak towards left. In figure, condition 1 (bent light guide) and 3 (steel box and electronic splitter) are compared. These cases are the best and worst one respectively and it is apparent that there is no such an effect. We can conclude that the QDC distribution is almost unchanged in all the configurations.

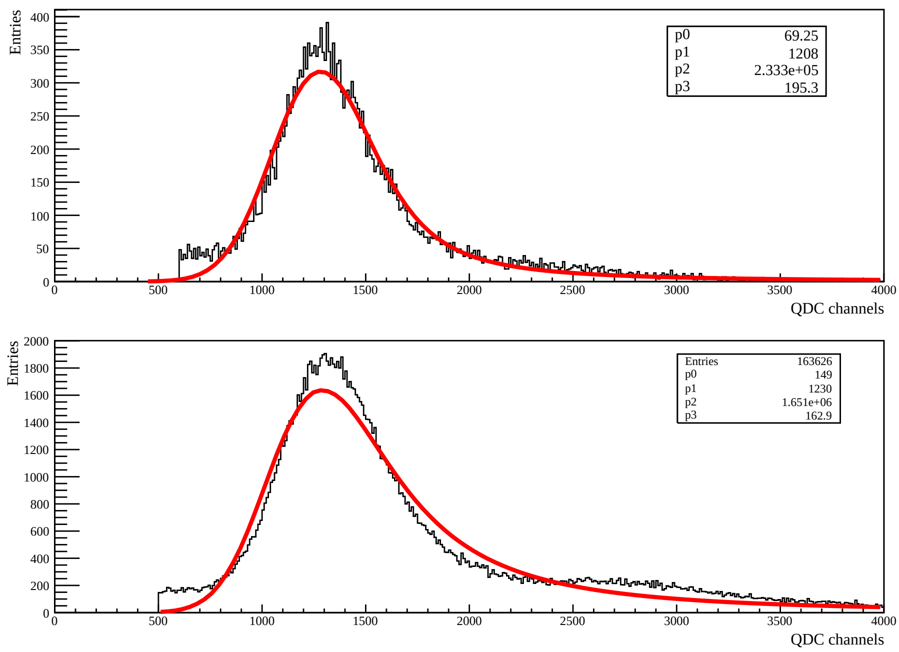


***Figure 4.19:*** *QDC spectra of signals acquired during the* HET *test beam. One QDC channel is equal to* 100 fC.

[4]Charge to Digital Converter. A QDC is a device which integrates an input signal and returns a digital value proportional to the value of the integral.

# Chapter 5

# Front-end electronics and acquisition system

The HET detectors are plugged into the DAΦNE beam pipe after the dipoles, 11 m away from the interaction point. For this reason, signals coming from HET detectors cannot be sent directly to the KLOE acquisition system: they need their own independent acquisition system.
The HET acquisition system, that has been designed and built within the work of this thesis, acquires signals coming from both the positron and the electron HET detectors. To do that, analogue signals coming from PMTs are firstly buffered and successively discriminated, shaping digital signals. In this way a digital string is obtained, representing the pattern of the scintillators that have been hit by a lepton. This pattern is stored only if a physics event has occurred in KLOE, in the correspondent bunch crossing, i.e. if both levels of trigger (see section 1.2.3) have been asserted. The critical task, handled by the acquisition system, is to associate this pattern with the proper event occurred in the KLOE apparatus. All the stored data are finally delivered to the KLOE acquisition system.

The HET acquisition system is composed of a set of three electronic boards,

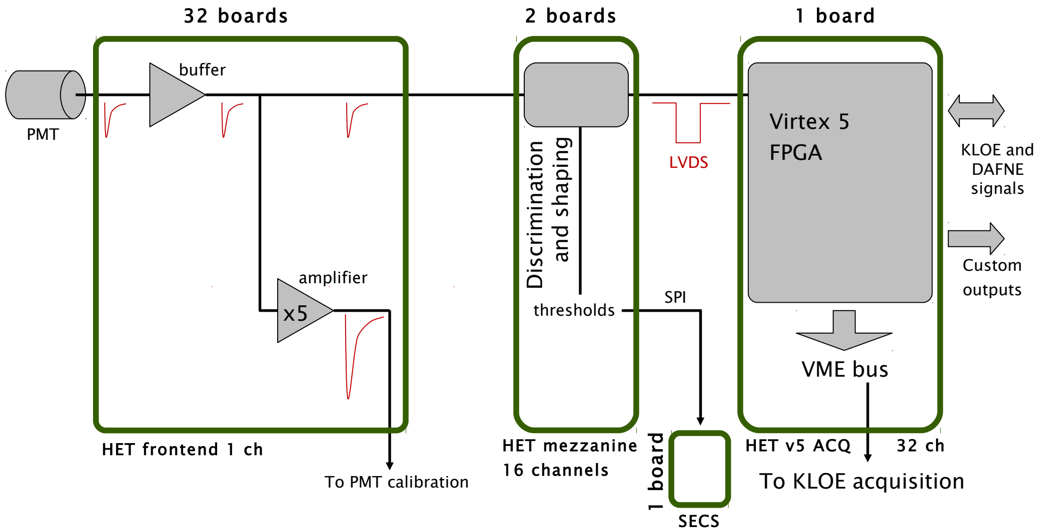


***Figure 5.1:*** *A scheme of the electronic acquisition chain of the* HET *detector.*

plus one slow control board (see the scheme in Fig. 5.1). In the following, this set of boards will be referred to as the HET electronic chain. The first part of the chain, handling PMT analogue signals, is called the front-end electronics and is composed of the HET front-end board and the discrimination and shaping board (also referred to as mezzanine). The second part, which performs the measurements and interact with signals from KLOE and DAΦNE is called HET acquisition system and is composed of the HET data acquisition board.

In the following sections, every board of the chain will be examined in detail. For the sake of simplicity, we will describe a single arm system, although there are 2 HET detectors installed on DAΦNE, one for each arm (positron and electron). Moreover, all the electronic chain has been designed to handle 32 input channels, albeit we have seen that each HET detector is composed of 28 + 1 scintillators (see Chapter 4). This redundancy is meant to have a quick set of spare channels in case of damage of any board within the electronic chain.

## 5.1 Front-end electronics

The first part of the HET electronic chain is the front-end electronics. It is composed of 2 kinds of board:

- 32 photomultiplier front-end boards: 1 channel per board;
- 2 discrimination and shaping boards (mezzanine): 16 channels per board.

Let us analyse these boards into detail.

### 5.1.1 The HET photomultiplier front-end board

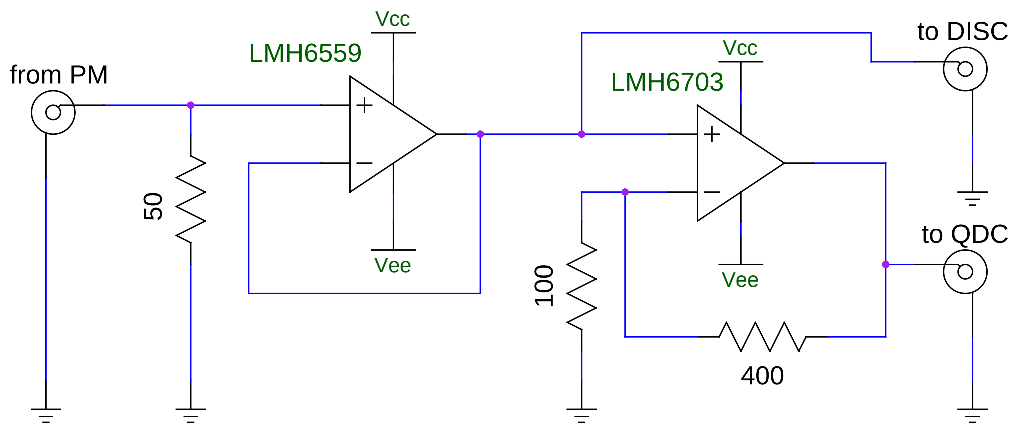


*Figure 5.2: Electronic schematics of the HET front-end board.*

Each photomultiplier of the HET detector is equipped with a front-end board.
The dimensions of this board are: 76.2 mm × 17.78 mm.
The tasks of this board are:

- to buffer the photomultiplier signal with high bandwidth;
- to drive transmission line up to the discrimination board;

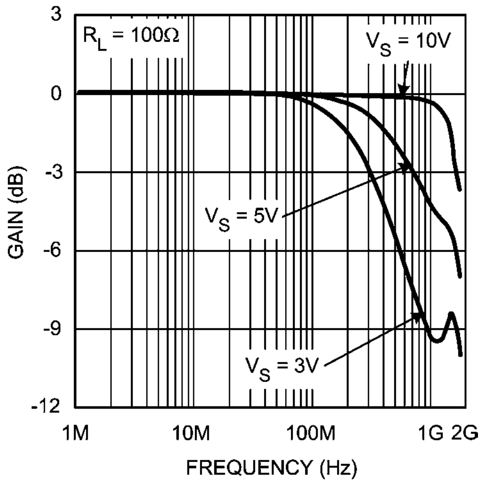


***Figure 5.3:*** *Typical performances of the* `LMH6559` *buffer for several supply voltages $V_S$. In our case $V_S = 10\,\mathrm{V}$ as the buffer is supplied with $\pm 5\,\mathrm{V}$.*

- to send an amplified ($\sim 5x$) signal to the slow control system;
- to measure the environment temperature.

Let us examine in detail how the front-end board handles these tasks. The signal coming from the PMT is first decoupled thanks to a unity gain amplifier, or buffer, (`LMH6559`) and then it is split.
The `LMH6559` has got a 1750 MHz bandwidth that perfectly fits our requirements. The typical performances of the `LMH6559` are shown in Fig. 5.3. After the buffer, one copy of signal is sent directly to the discrimination board (see section 5.1.2). The second copy is amplified and sent to the QDC within the slow control system (see section 5.3). The QDC in use (CAEN `V792AC`) needs higher input signal, for this reason we chose to use an operational amplifier in non-inverting configuration with a gain $\sim 5$. For this signal, we do not have as strict requirements as for the buffer, so our choice went to a less performing operational amplifier: the `LMH6703` (see Fig. 5.4). Additionally the `LMH6703` can be switched off by setting a pin to the ground level. We want to do that when the slow control system is idle (i.e. during regular data acquisition) in order to reduce power consumption, limit the board temperature, and reduce electronic noise.

The front-end board is placed as close as possible to the photomultiplier in order to minimise noise. The signal coming out from the buffer

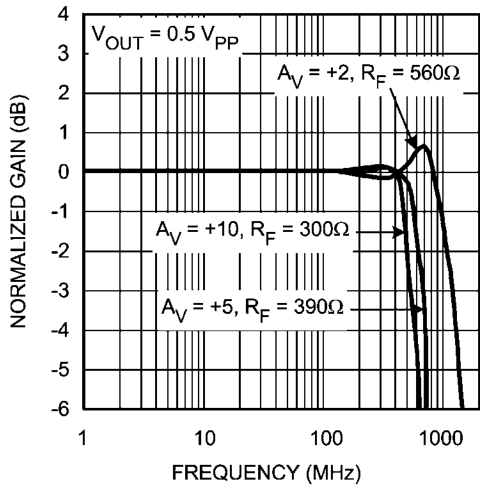


***Figure 5.4:*** *Typical performances of the* `LMH6703` *operational amplifier buffer for several amplifications $A_V$. In our case $A_V = 5$.*

goes through a 5-meter 50 Ω coaxial cable before entering the discrimination board. The `LMH6559` is perfectly suited to drive such a transmission line. In order to reduce the noise coming from power supply, we chose to equip every board with independent voltage regulators. This choice can cause an excessive power dissipation. For this reason we used two low-drop voltage regulators (LDO), with a low quiescent current[1] (less than 1 $\mu$A) and a maximum power dissipation of about 140 mW[2]. The positive voltage (+7 V) is changed into $V_{cc} = +5$ V by means of the `MC78LC50` LDO. $V_{ee} = -5$ V is obtained from the negative supplied voltage (−7 V) through the `MIC5270` LDO. The absorbed current, from both positive and negative power supply, is about 20 mA.

The HET front-end board is capable of measuring environmental temperature (within the range of: −40 °C, +125 °C) by means of the `TC1047A` temperature sensor. This device needs a 5 V power supply and its output is a voltage $V_{OUT}$ varying linearly as a function of the sensed temperature $T$

[1]The quiescent current is the current which flows through the ground when the regulator operates without a load on its output: internal IC operation, bias, etc. When the regulator becomes loaded, it becomes actually the difference between the input current (measured through the regulator input pin) and the output current.

[2]The HET front-end board has a power dissipation of about 100 mW.

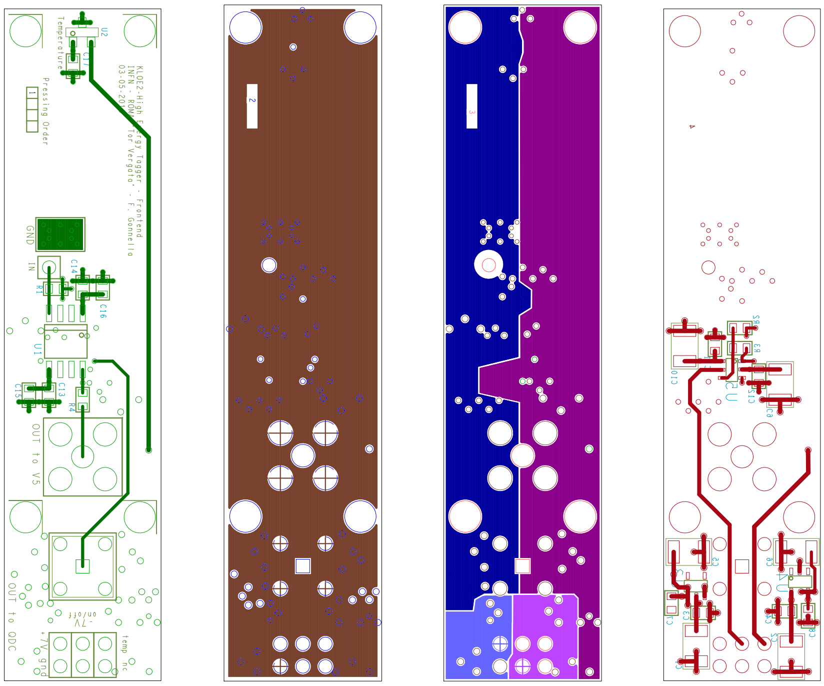

**(a)** Top **(b)** Inner 1 **(c)** Inner 2 **(d)** Bottom.

***Figure 5.5:*** *Layers of the* HET *frontend board.*

(measured in degrees Celsius):

$$V_{OUT} = 10\,\frac{\mathrm{mV}}{^{\circ}\mathrm{C}} \cdot T + 500\,\mathrm{mV}$$

The printed circuit board of the HET front-end has been realised in 4 layers (Fig: 5.5):

- Top: routing layer;
- Inner layer 1: ground shape;
- Inner layer 2: power shapes: $V_{CC}$ (+5 V) and $V_{EE}$ (−5 V);
- Bottom: routing layer.

This number of layers is enough to guarantee a 50 Ω impedance for every routed line on the top and on the bottom layer, together with a small board size (as large as the diameter of the photomultiplier).

Every HET front-end board is equipped with a 2×3-pin (2.54 mm pitch) control connector, whose pin-out is shown in table 5.1.

| | | |
|---|---|---|
| +7 V | Amp. on/off | Temp. |
| Ground | −7 V | NC |

***Table 5.1:*** *Pin-out of the HET front-end board control connector, top view, connector on the bottom edge of the board, like in Fig. 5.5.*

### 5.1.2 The HET discrimination and shaping board

Signals coming from each photomultiplier must be discriminated and digital signals must be shaped and sent to the acquisition system. These tasks are handled by the *discrimination and shaping boards*. These boards must be plugged onto the data acquisition board (HET-DACQ), hence they are often referred to as "mezzanine". One of these boards is made up of 16 channels. Each of the 2 HET detectors (on positron and electron arm) needs 32 channels, therefore 2 mezzanines are connected to each of the two HET-DACQboards. The mezzanines are VME[3] 6U boards, (dimensions: 160 mm × 233 mm), although they only take power supply (+12 V and +5 V) from the VME crate. The main features of the mezzanine board are:

- 16 discrimination and shaping channels;
- Two voltage regulators to supply the needed voltages: −5 V, 2.5 V while the +5 V is taken directly from the crate;
- High speed mezzanine connector to be plugged into the data acquisition board;

[3]VME acronym stands for VERSAbus Module Eurocard. It is a computer bus standard that fixes physical dimensions (denoted 1U, 2U, etc. depending on their height) and communication protocol. For more information see references [34, 35].

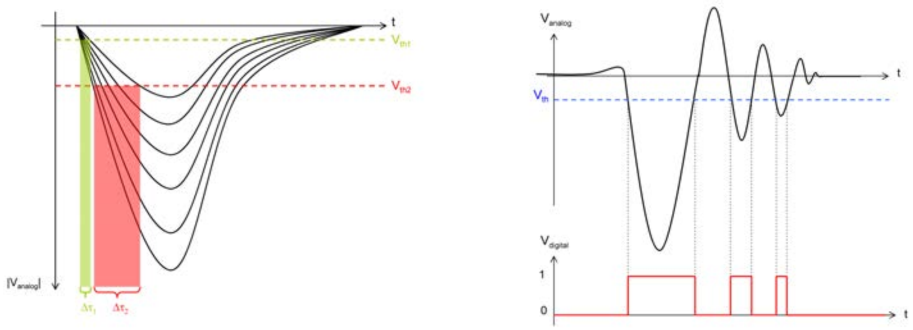


**(a)** Comparison of jitter (due to variation of signal slope) for to 2 different threshold values. One can see the improvement obtained with a lower threshold value.

**(b)** Discrimination of ripples resulting into fake signals, due to a too low threshold value.

***Figure 5.6:*** *Issues of single threshold discrimination.*

- High speed mezzanine socket to host an additional mezzanine board;
- 32 settable thresholds (2 per channel) through the SPI interface.

The single channel of the mezzanine is basically a comparator followed by a pair of D flip-flop used to shape a fixed width digital signal.

In order to get rid of all the problems arising from a single threshold discrimination (see Fig. 5.6), the double threshold discrimination has been chosen. It guarantees the following features:

- reduction of the jitter of the output signal: the signal is triggered on a very low threshold (low dependency from the signal slope and amplitude);
- reduction of background discriminations: small signals coming from noise or ripples are ignored thanks to a higher threshold voltage.

The single discrimination and shaping channel is represented in Fig. 5.7. Let us examine the schematics in detail. The signal coming from the front-end board is sent to the `LMH6559` buffer (the same as in section 5.1.1), which acts both as a 50 Ω impedance receiver and as a signal splitter. Each copy of the signal is delivered to one of the two channels of the `LMH7322` comparator. In order to perform a double threshold discrimination, one of these is

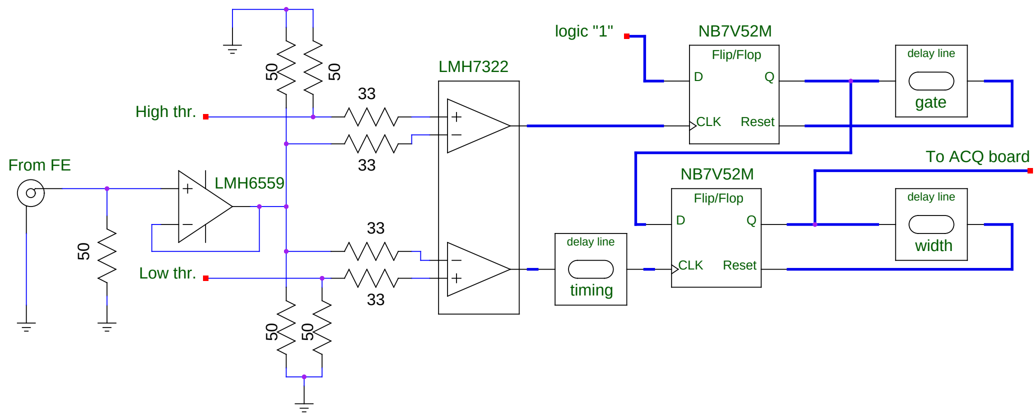


***Figure 5.7:*** *Schematics of the discrimination and shaping channel. Thicker blue line stands for a differential pair.*

compared to a fixed low threshold voltage, the other to a high threshold voltage. If the signal exceeds the high threshold, the clock signal of the upper `NB7V52M` flip-flop becomes high. As its D signal is connected to a logic high value, the flip-flop is triggered and its output becomes high. The lower flip-flop, whose D signal is connected to the output of the upper one, is enabled for a time depending on the *gate* delay line. After this time the upper flip-flop is reset and the lower one is disabled.
The signal having exceeded the high threshold value is surely high enough to exceed the low one, thus the clock of the lower flip-flop rises to a high value after a time depending on the *timing* delay line. If the lengths of these two delay lines are properly tuned, the lower flip-flop will fire a signal with a duration depending only on the *width* delay line.

In order to optimise the discrimination and shaping performance, the length of the *gate* ($\Delta t_g$) and *timing* ($\Delta t_t$) delay lines must be properly chosen. In order understand how to do that, it is necessary to take into account some features of `NB7V52M` flip-flops. First of all they are triggered only on the rising edge of the clock signal. This means that if the input signal becomes high and then low without any change in the clock signal, the output does not change. As far as the reset signal is concerned, one thing must be

noticed: the output signal is low as long as the reset signal is high plus an additional reset time $\Delta t_r$ lasting something between 500 ps and 600 ps.
The requirements of the discrimination system are basically:

- no discrimination on ripples;
- a shaped output signal lasting 2 ns;
- a dead time less than 2.7 ns, in order to be able to detect signals produced by leptons belonging to two consecutive bunches;
- a proper timing of the two output signals of the comparator (high and low threshold signals).

A simple study of the photomultiplier (see Fig. 4.10a on Pag. 71) signal tells us how to fulfil the first requirement: the first ripple happens after 2.5 ns, so:

$$2\Delta t_g + \Delta t_r < 2.5\,\text{ns}. \tag{5.1}$$

Considering the worst condition $\Delta t_r = 0.6\,\text{ns}$, we easily obtain:

$$\Delta t_g < 0.95\,\text{ns}. \tag{5.2}$$

The second and the third requirements are constraints almost only for the *width* delay line length $\Delta t_w$. Considering $\Delta t_r = 0.6\,\text{ns}$ we obtain: $\Delta t_w = 1.4\,\text{ns}$. The last requirement means that we want the low threshold signal to rise just in the middle of the gate. This is not an easy task, because it depends on several things: the delay between the low and high threshold crossing (hence on the threshold voltage values), the height and the slope of the photomultiplier signal and finally the value chosen for $\Delta t_g$.
Tests performed in laboratory (see section 5.4.2) tell us that the right choice is: $\Delta t_t = 620\,\text{ps}$ and $\Delta t_g = 480\,\text{ps}$.

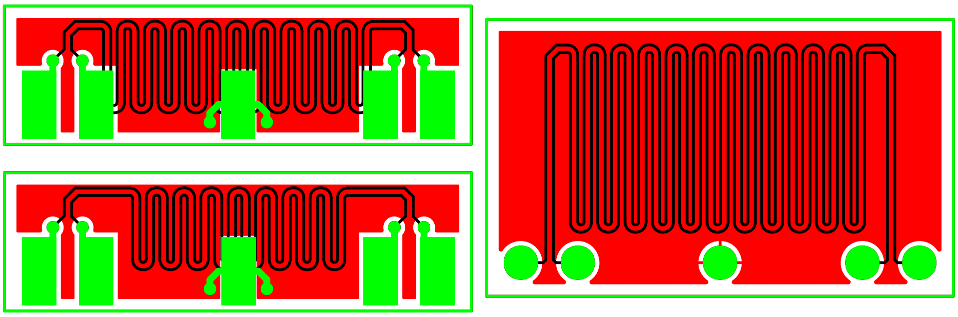

***Figure 5.8:*** *PCB[4] layout of the delay lines.*

We need a great number of delay lines: 3 per channel, $3 \cdot 16 = 48$ lines per board, for a total of 4 boards (two HET detectors) and 192 delay lines. Moreover, their parameters (impedance and delay time) must be kept under control and a big dispersion cannot be tolerated. For this reason we have to discard the hypothesis of delay lines realised on cable. Moreover, cable delay lines, having a length of the order of 10 cm, would cause the board to become awkward and hardly fit into the VME crate without hindrance. On the other hand, commercial delay lines exist realised as integrated circuit on ceramic support. Unfortunately, these devices are far too expensive (∼ €15 for each delay line).
The solution we chose to adopt is to design and realise all the needed delay lines, as small printed circuit boards which can be soldered on top of the mezzanine boards (see Fig. 5.8 and Fig. 5.9).
The dimension of the printed circuit boards are: 20.83 mm×6.17 mm for the 480 ps and 620 ps delay line, and 20.83 mm × 12.34 mm for the 1.4 ns delay line. Tests performed on these line, confirm a perfectly uniform impedance, stable within the percent level. The differential impedance is 100 Ω and the single-ended is 50 Ω. The delay time differs from the nominal of few tens of picoseconds.

Let us spend some words on the hardware specifications. The `LMH7322` is a 2-channel comparator, having a very short rise and fall time (160 ps) in the output signal. On the other hand, the `NB7V52M` flip-flop has a very small random jitter: less than 800 fs RMS.
The outputs of comparator, as well as all the signals of flip-flops, follow the

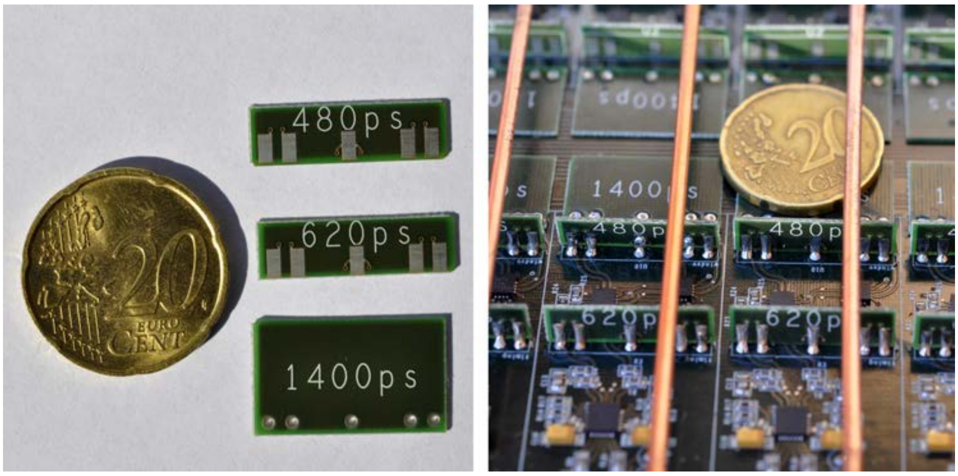


***Figure 5.9:*** *On the left, a picture of the delay lines realised for the* HET *discriminator. On the right, the same delays soldered onto the board.*

LVDS[5] standards, and are represented in Fig. 5.7 with a thick blue line.
This kind of standard is made of a differential pair, with logic levels settling around 1.2 V: HIGH=1.4 V, LOW=1.0 V.
This standard reduces the noise coupling and allows very steep slopes in signal transitions.
The power supplies of the board are handled as following:

- +5 V from VME crate ($i \simeq 2.7$ A);
- +12 V from VME crate ($i \simeq 0.9$ A);
- −5 V obtained from +12 V through the `PTN78060` voltage regulator;
- +2.5 V obtained from +5 V through the `PTH04T240` voltage regulator.

The 16 pairs of threshold voltages are set by the `AD5382BST` multichannel DAC[6]. This device has 32 analogue output voltages which can be set via SPI[7] by the slow control system (see section 5.3). For each channel, one `LM358` dual operational amplifier is used to invert the polarity of high and low thresholds.

[5] LVDS acronym stands for: Low Voltage Differential Signalling
[6] DAC acronym stands for Digital to Analogue converter.
[7] SPI acronym stands for Serial Peripheral Interface.

| | |
|---|---|
| Not Connected | Ground |
| $\overline{\text{busy}}$ | $\overline{\text{sync}}$ |
| Data out | Data in |
| Clock | $\overline{\text{load dac}}$ |

***Table 5.2:*** *Pin-out of the SPI control connector of the discrimination and shaping board, top view, board with the connector in the upper left corner (as in Fig. 5.11).*

The SPI control connector is a 8-pin 2.54 mm pitch through hole 90-degree connector located in the front panel of the board. Its pin-out is reported in table 5.2. In addition, on the QTH90 connector, the SPI interface, used to program the DAC, is also available. By soldering a set of six 0 Ω resistors, one can choose to connect the SPI interface to the control connector on-board or to the HET-DACQ. In our case we chose to program the threshold values by means of the SECS board (described in Sec. 5.3) through an external flat cable plugged into the control connector.

The printed circuit of the discrimination and shaping board is a stack of 4 layers (in Fig: 5.10 the top and bottom routing layers are drawn):

- Top: routing layer;
- Inner layer 1: analogue and digital ground shapes (connected with several 0 Ω resistors, or inductors);
- Inner layer 2: power shapes: $V_{2.5} = 2.5\,\text{V}$, $V_{CC} = +5\,\text{V}$ and $V_{EE} = -5\,\text{V}$;
- Bottom: routing layer.

This number of layers is enough to guarantee a 50 Ω impedance for every routed line on the top and on the bottom layer, together with a proper board size to fit VME 6U standard dimensions.
As one can see in the figure, all the output signals of the channels are routed up to a connector placed on the top centre of the board.

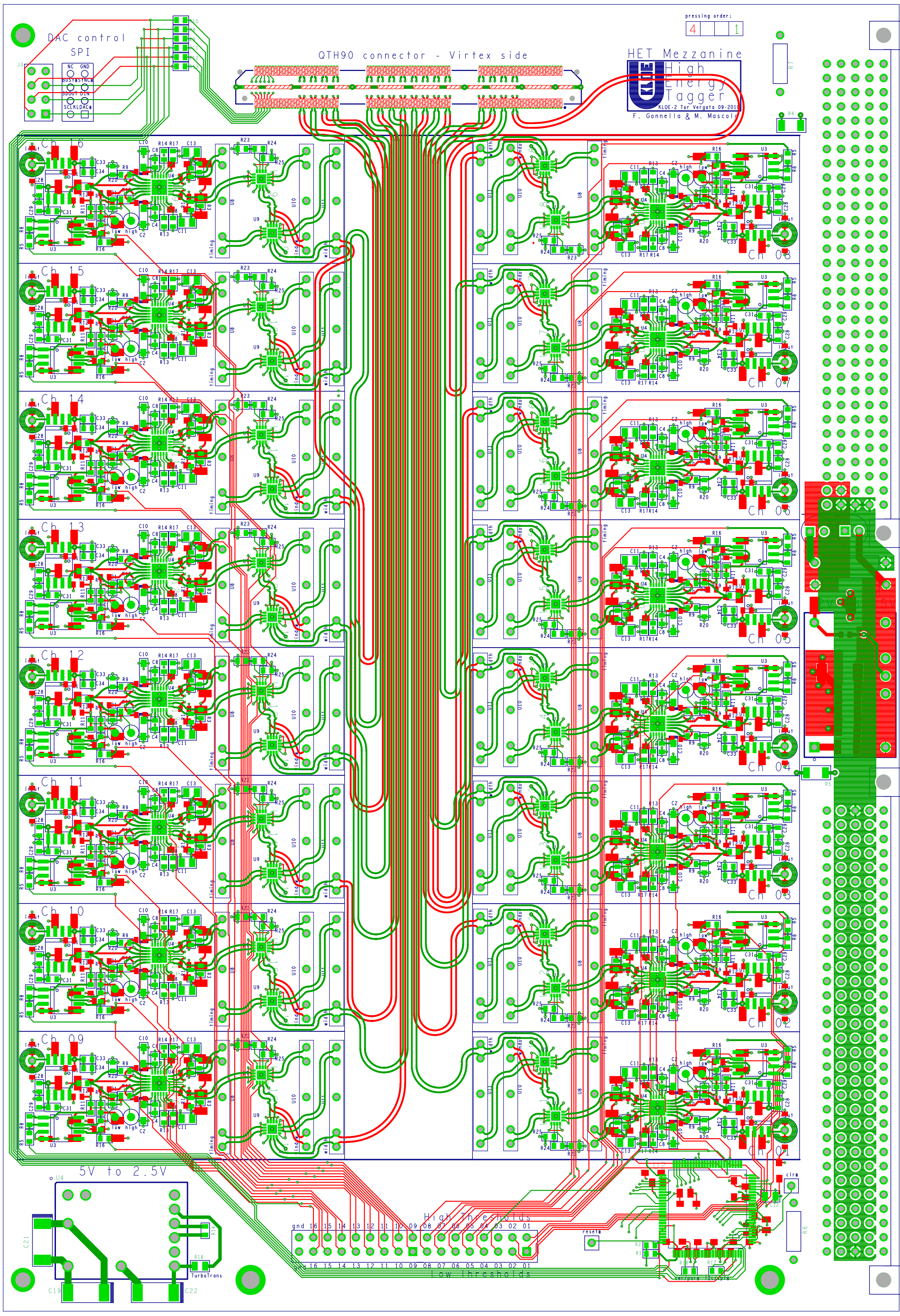


***Figure 5.10:*** *Routing layout of the discrimination and shaping board. For the sake of simplicity, only the top (green) and bottom (red) layers are shown.*

This connector is a high speed mezzanine connector (SAMTEC QTH90) and it is used to plug this board on top of the HET-DACQ board.
On the bottom layer, a high speed connector socket (SAMTEC QTS90) is placed, which another mezzanine can be plugged into.
The boards (that are perfectly alike) are designed in such a way that all the 32 output signals result connected on the free QTH90, simply by plugging the two boards one on top of the other. In fact the QTS90 connects all the signals coming from the additional board to the remaining pins of the QTH90 on the same board. In this way all of the 32 channels are connected to the HET-DACQ board.
The input SMA[8] connectors, placed on the front panel, are connected to the channels of the board by means of hard copper shielded cables, clearly visible in the photograph in Fig. 5.11.

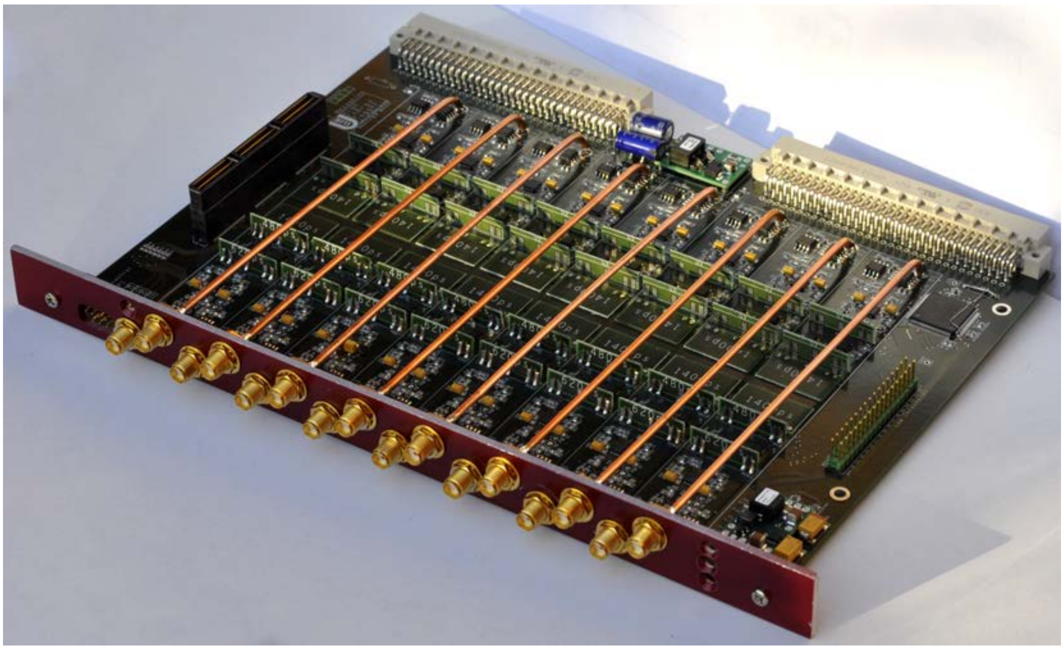

***Figure 5.11:*** *A picture of the* HET *discrimination and shaping board.*

[8]SMA (SubMiniature version A) connectors are coaxial RF connectors developed in the 1960s as a minimal connector interface for coaxial cables, with a screw type coupling mechanism. The connector has a 50 Ω impedance and offers excellent electrical performance up to 18 GHz.

## 5.2 The HET acquisition system

The HET acquisition system has to fulfil the following requirements:

- measure the deviation of $e^+e^-$ from the main orbit;
- associate each measure with the proper bunch;
- acquire data continuously with storage on T1 and T2 trigger signals;
- transfer data to the acquisition CPU through the KLOE specific protocol.

To this end the so called HET *data acquisition board*, equipped with a Xilinx Virtex5 (V5) FPGA[9] has been designed and built. A detailed description of the board design is given in 5.2.3, here we discuss its working principles. The strategy chosen to perform the association is to measure the time of arrival of the hit on the detector with respect to a reference signal. In order to do that, a TDC has been implemented onto the V5. The time is measured with respect to the rising edge of the DAΦNE *fiducial* signal, a digital signal synchronous with the first injected bunch of leptons (see Fig. 1.5 on Pag. 11). By means of this time measurement, one can tell which bunch (from 1 to 120) the lepton, having hit the HET detector, belongs to. Through this piece of information, it is possible to perform the association between the physics event occurred in the KLOE apparatus and the lepton deviation from the nominal orbit after the dipole magnets.

### 5.2.1 Time to Digital Converter on the Virtex 5 FPGA

Since the bunch crossing occurs in DAΦNE each $T_{bc} = 2.7\,\mathrm{ns}$, in order to properly disentangle leptons coming from two consecutive bunch crossings, the TDC time resolution must be less than $T_{bc}$. On the other hand, its range (i.e. the highest measurable value) must be at least of 324 ns, corresponding

[9] FPGA stands for Field Programmable Gate Array.

to the time interval between to consecutive rising edges of the *fiducial* signal. The TDC implemented onto the V5 FPGA widely fulfil these requirements with a time resolution of 625 ps and a range of 640 ns.

In order to get such a high resolution and a wide range, we made use of the Nutt's Linear Interpolation [36] TDC technique. It consists of performing a set of one coarse measurement plus two high-resolution ones. All the 3 measures are performed with respect to the positive edges of an internal clock reference signal. In Fig. 5.12 the working principles of Nutt's tech-

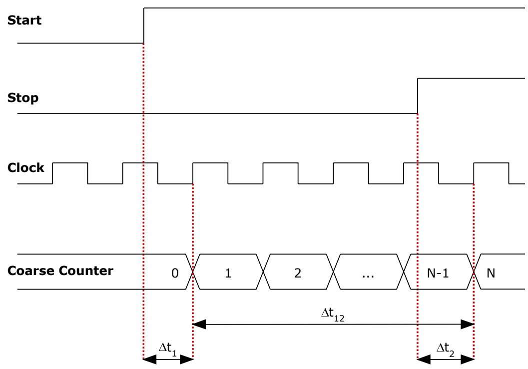


***Figure 5.12:*** *A scheme of Nutt's linear interpolation TDC technique.*

nique are sketched. The low resolution measurement $\Delta t_{12}$ is carried out by a digital counter. This device counts out the number of clock cycles occurring between the first rising edge after the *start* pulse, and the first rising edge after the *stop* pulse. This measurement is affected by two uncertainties: $\Delta t_1$ and $\Delta t_2$ represented in figure. Measuring these two quantities, we obtain the overall time measurement:

$$t = \Delta t_{12} + \Delta t_1 - \Delta t_2. \tag{5.3}$$

The time intervals $\Delta t_1$ and $\Delta t_2$ last less than one clock cycle, so they can be measured with higher resolution techniques, with no further concern about having a wide range.

The technique used to measure these time intervals with high resolution is the 4x-oversampling. The V5 FPGA has a set of embedded devices called Digital Clock Manager, or DCM (see Tab. 5.3 on Pag. 103). These devices al-

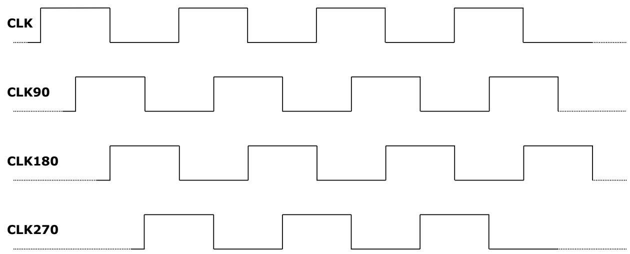


***Figure 5.13:*** *A representation of the four clock signals (clk, clk90, clk180, clk270) generated by the DCM.*

low to generate 4 clock signals having the same frequency but with different time relations. In particular, if we call $clk$ the system clock of period $T$, the DCM provides the following signals (see Fig. 5.13): $clk90$ (delayed by $\frac{T}{4}$), $clk180$ (delayed by $\frac{T}{2}$), $clk270$ (delayed by $\frac{3T}{4}$). The 4x-oversampling technique consists basically of sampling the input signal by means of 4 flip-flops synchronised with each of the 4 clock signals generated by the DCM. In this way, the time resolution improves by a factor 4, with respect to the one that would result by sampling the signal with the $clk$ signal alone. Clearly, the 4 samples obtained in this way are synchronised with 4 different clock signals, and cannot be used. In order to resynchronise them to the $clk$ signal, we implemented the circuit shown in Fig. 5.14. There are 4 stages of flip-

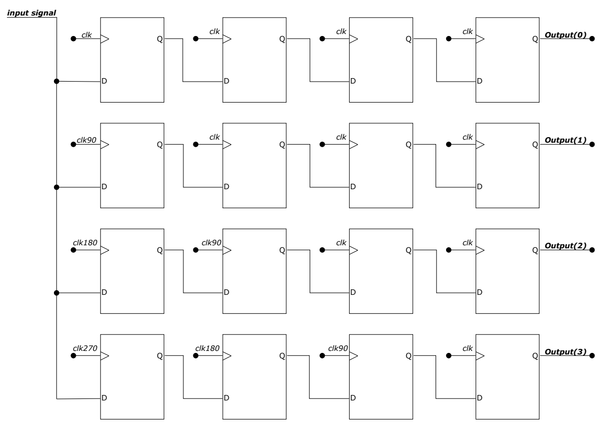


***Figure 5.14:*** *Synchronisation circuit used for the oversampling TDC technique.*

flops, represented as columns in figure. After the first stage has sampled the input signal, the remaining 3 stages are used to resynchronise the 4 signals in such a way that the minimum time occurring between two consecutive samples is $\frac{3}{4}T$. This is done in order to assure that the data on the outputs of any of the stages is ready before the following stage starts to sample.

### 5.2.2 Data storage and $T1$, $T2$ trigger signal handling

The TDC performs measurements continuously, producing a big amount of data out of which only a little part carries relevant information. In order to select and store only relevant data, the KLOE trigger signals $T1$ and $T2$ (see Sec. 1.2.3 for a detailed description of the KLOE trigger system) are exploited. The data selection procedure is the following:

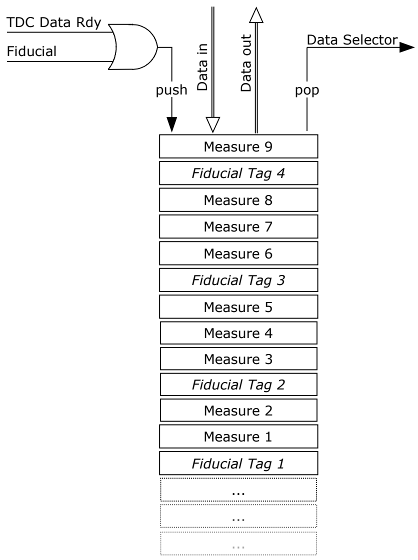


***Figure 5.15:*** *A scheme of the stack and an example of its content. In writing mode, time measurements are stored as well as fiducial tag. In reading mode, data are popped out of the stack until a specified number of fiducial tags are read.*

1. data are continuously stored into a LIFO[10] memory or *stack* buffer (shown in Fig. 5.15);

2. rising edges of the fiducial signal are stored into the stack in the same fashion as regular data, but using a peculiar word, called *fiducial tag*, which cannot be confused with any other datum;

[10]LIFO acronym stands for Last In First Out.

3. the rising edge of the $T1$ signal starts the reading procedure of the stack. The reading is stopped as soon as a specified number, $N_{fid}$, of fiducial tags are read out.

The LIFO memory assures to read out only most recent data, more specifically the selected data is always relative to the last $N_{fid}$ cycles.

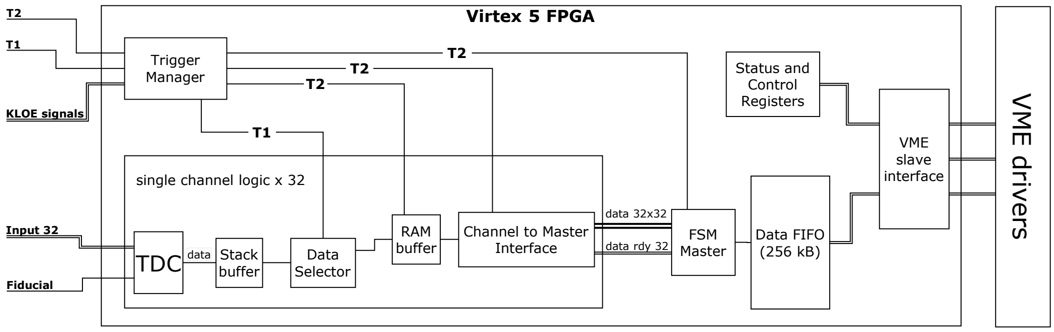


***Figure 5.16:*** *A simplified scheme of the acquisition system implemented onto the V5 FPGA on the* HET *data acquisition board. Please note that the TDC (and the surrounding logic) is replicated for each of the 32 channels.*

In figure 5.16 a simplified scheme of the whole acquisition system is represented. The TDC and the surrounding logic (*Stack Buffer*, *Data Selector*, *RAM Buffer*, *Ch. to Master Interface*) are replicated for all the 32 channels. The first recording stage is performed onto the *Stack Buffer* described before, and it is handled by the state machine *Data Selector*. Data read out from the *stack* is temporarily stored on the *RAM Buffer*, when a positive edge of the $T1$ signal is detected. If the $T1$ signal was generated by a physics event in KLOE, then a $T2$ signal is about to be asserted. When this happens, data previously stored in the RAM buffer is “protected” by increasing the RAM pointer to the next memory location. If no $T2$ signal follows the $T1$, the RAM pointer is not increased and data will be overwritten, on the positive edge of next $T1$ signal. The positive edge of the $T2$ signal also triggers the state machine *Channel to Master Interface* that delivers to the *FSM*[11] *Master* only data corresponding to a $T2$ assertion. At last, the *FSM Master* on every $T2$ positive edge, checks all the channels, retrieves all the data (ignoring all

[11]Finite State Machine.

those channels which contain fiducial tags only), and writes data onto the *DATA FIFO*, formatted according to the KLOE-2 standard. The *DATA FIFO* used for storing formatted data is a 256 kByte memory containing 64 bit words. Each word is composed of 3 measurements (or *fiducial tags*). As shown in Fig. 5.16, the content of *DATA FIFO* can be accessed through the VME interface. The VME interface that we implemented follows the 2eVME64x standard and allows access in the following modes:

- VME A32/D32 in single shot mode;
- 2eVME64x A32/D64 in block transfer mode.

Status and control registers can only be accessed in single shot mode, while the *DATA FIFO* can be accessed in both modes. Details on the VME64 protocol specifications are beyond the scope of this thesis, but can be found on references [34, 35]. All addresses are 32 bit: the first 8 bit are the board main address and are set through 2 hexadecimal switches (see Fig. 5.17).

### 5.2.3 The HET data acquisition board

The HET main acquisition (HET-DACQ) is a VME 6U board with dimensions: 160 mm × 233 mm. As previously said, the tasks handled by this board are to measure the timing of the signals coming from discriminators (see Sec. 5.1.2) with respect to DAΦNE fiducial signal (see Sec. 1.2.1), store them only if KLOE trigger signals (see Sec. 1.2.3) are asserted, and transmit data to the KLOE acquisition system through the VME bus. To this end, the HET-DACQ board is equipped with:

- Xilinx Virtex 5 FPGA, in which the TDC and the VME interface are implemented;
- fast VME transceivers;
- 6 discriminating channels to handle DAΦNE fiducial signal, $T1$ and $T2$ trigger signals and KLOE signals;

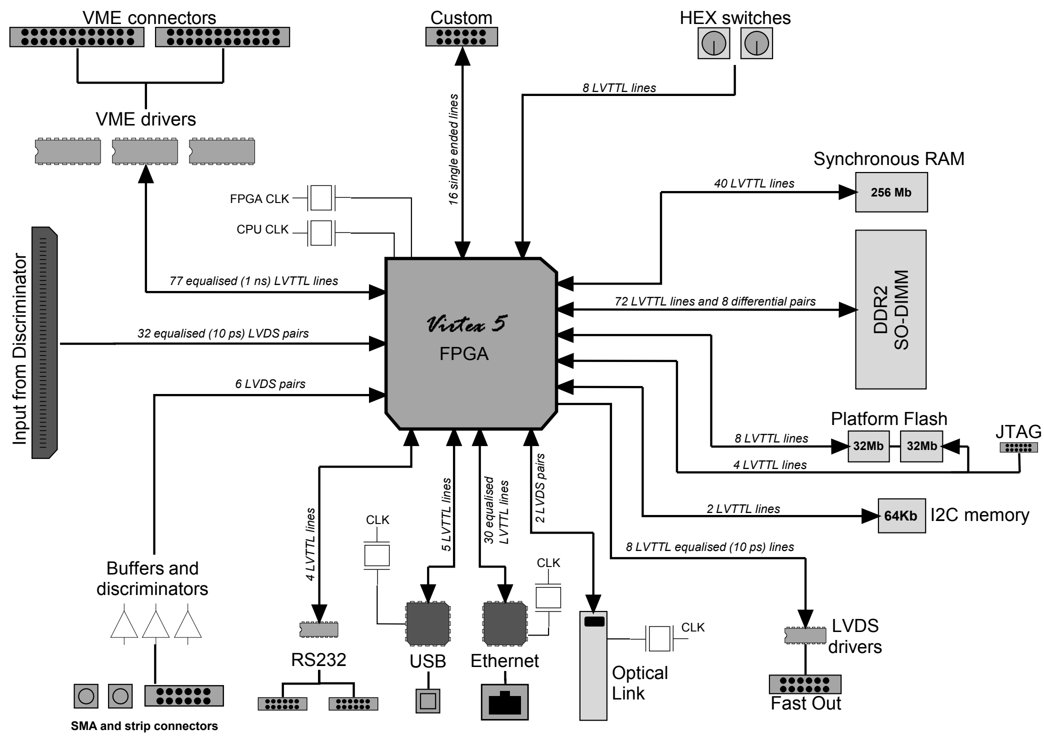


*Figure 5.17: A block diagram of the HET data acquisition board, referred t as HET-DACQ.*

- 32 LVDS input channels.

The Virtex 5 XC5VFX70T is definitely the main component of the board, handling all the on-board devices (see Fig. 5.17). It is worth to spend some words on the main features of this FPGA. The highest nominal working frequency of the V5 is 550 MHz, nevertheless the actual working frequency can be sensitively lower, according to the complexity of the implemented logic. In Tab. 5.3 a list of the main devices embedded in the FPGA is reported. Let us briefly explain the items in the table.
The Configurable Logic Block (CLB) are the main "bricks", out of which the logic inside the FPGA is implemented. Programming an FPGA means to enable or disable interconnections among these blocks.
The V5 FPGA contains 6 Clock Management Tiles (CMT). These devices are used to handle clock signals with high precision. In particular, inside each

| Device | Quantity |
| --- | --- |
| Filp/Flop CLB | 44800 |
| DCM | 12 |
| DSP | 128 |
| I/O pin | 640 |

***Table 5.3:*** *A list of the main devices embedded in the Virtex 5 XC5VFX70T FPGA.*

of them, there are 2 DCMs, which we made use of in the TDC logic (see Sec. 5.2.1). These devices can generate several clock signals with different phases.
The FPGA embeds a PowerPC 440 microprocessor. This CPU can operate at a frequency up to 550 MHz, although it is not used for the HET data acquisition, the board is perfectly equipped to handle it for future developments.
The 12 digital signal processors (DSP) compute complex mathematical operation. The 640 input/output (I/O) pins are grouped into blocks called IOB (Input/Output Block). These devices allow a great variety of standards for I/O signals, both single-ended and differential. Among these standards, we mainly used LVDS and LVTTL. Moreover, thanks to the DCI[12] technology, the IOBs provide the capability of terminating all the transmission lines internally to the FPGA, thus eliminating undesired reflections and drastically reducing the number of needed resistors on the PCB.

In order to enable the FPGA to acquire and receive signals over the VME bus, a set of line drivers is needed. We made use of 11 `SN74VMEH22501A` transceivers. Thanks to these fast devices, and to the interface implemented onto the FPGA, the HET-DACQ board is perfectly suited to handle *slave* communication mode on the VME bus, also using the double-edge VME64x (2eVME64x) standard [35]. Moreover, we routed all the needed connections to be able to implement a *master* VME interface on the FPGA as future development.

[12]DCI stands for Digitally Controlled Impedance.

KLOE signals and DAΦNE fiducial signal are connected to the HET-DACQ board through 90-degree SMA connectors available on the front panel. Signal discrimination is performed by means of the same comparators used in the HET discrimination and shaping board: the LMH7322. The LVDS outputs of these devices are routed directly to the V5 FPGA.

In order to acquire signals coming from discriminators, the HET-DACQ board is provided with a SAMTEC QTS90 high speed socket. This connector is perfectly suited to receive the 32 LVDS signals coming from a pair of discriminators (see the end of Sec. 5.1.2). From this connector, 32 equalised (10 ps) differential pairs are routed up to the FPGA. All these wires have a uniform and controlled differential impedance of 100 Ω and of 50 Ω with respect to the ground level.

The HET-DACQ board is equipped with 5 low-jitter oscillators. One of these devices provides the system clock, a differential LVDS signal, with a frequency of 100 MHz. The remaining oscillators have been installed for future developments: CPU (200 MHz), USB interface (12 MHz), Ethernet interface (25 MHz), and Multi-Gigabit Transceiver (100 MHz).

The V5 FPGA needs to be programmed when the board powers up. To this end, the HET-DACQ is equipped with two 32 Mbit Xilinx programmable configuration PROMs. These PROMs provide reprogrammable method for storing large Xilinx FPGA configuration bit-streams. Furthermore, a 64 Kbit serial (I2C) memory (24AA64) is mounted on-board. This device can be used by the FPGA to store sensitive data that need to be retrieved also in case of board power down.

The HET-DACQ board gets the 5 V power supply from the VME crate. The external pins of the V5 FPGA are divided into 27 *banks*. Each bank is set to a specific voltage standard (in our case mostly LVTTL or LVDS) and needs an independent power supply depending on the chosen standard. For example: 3.3 V for LVTTL banks, 2.5 V for LVDS banks and 1.8 V for banks used for DDR2 connection. In order to generate all the voltages needed by the FPGA and by all the hardware on-board, 11 power regulators are used. Two switching regulators `PTH08T240` are used to generate 3.3 V and 1.8 V. An independent `PTH08T220W` regulator is used to power with 1.8 V the internal circuitry of the Virtex. A negative voltage of $-5$ V is needed by the analogue circuitry used to handle DAΦNE fiducial and KLOE signals: `LMH6559` buffers and `LMH7322` comparators (same components as in the discrimination board see Sec. 5.1.2). This regulation is handled by the `PTN04050A` switching voltage regulator. In order to handle the remaining voltages ($2 \times 2.5$ V, $2 \times 1.2$ V, 1.0 V), 5 `TPS74401` low-drop power regulators are used. Two `TPS51100DGQ` regulators, specially designed for DDR2 handling, are used to precisely divide by 2 the 1.8 V generating the 0.9 V needed for handling RAM signals.

### CPU and other features

A power-PC can be implemented onto the Virtex 5 FPGA. We planned to use this feature for future developments within the KLOE-2 experiment (modification in the trigger system see Sec. 3.6) or for general purposes. Operative System and software needed by the power-PC can be stored on the additional 256 Mbit synchronous RAM installed on-board. Furthermore, in designing such a complex board, we chose to add some other features that can be useful, especially in combination with the CPU implemented on the V5. These features are:

- $2 \times$ RS232 interfaces;
- slave USB interface;
- Ethernet interface with RJ-45 connector;
- Optical link;
- SO-DIMM connector, capable to host one DDR2 ram module (up to 2 GB);

- 8 custom fast LVDS outputs;
- 16 general input/output.

In order to make the board as much versatile as possible, it has been equipped with the most typical communication interfaces. Two RS232 serial ports are connected to the FPGA through the MAX202 transceiver. The MAX3420E integrated circuit contains the digital logic and analogue circuitry necessary to implement a full-speed USB peripheral compliant to USB specification rev 2.0. The Alaska Ultra 88E1111 Gigabit Ethernet Transceiver is a physical layer device for Ethernet 1000BASE-T, 100BASE-TX, and 10BASE-T applications. It contains all the active circuitry required to implement the physical layer functions to transmit and receive data on standard unshielded twisted pair.

The board is provided with two additional features: an optical link is connected to a Multi-Gigabit Transceiver (MGT)[13] embedded in the FPGA and 2 fast (SN45LVDS047) LVDS drivers used to shape 8 fast output signals. These communication devices are going to be used respectively during the integration of the HET into the main KLOE trigger system and during the stand-alone data acquisition mode (both these novel trigger strategies are described in Sec. 3.6).
Let us now describe the basic principles of the implementation of these strategies. We will make use of a third HET-DACQ board with a new logic implemented onto the V5 FPGA. This board will be able to receive signals coming from the two HET-DACQs installed in positron and electron tagging stations and quickly elaborate information. In trigger integration strategy, the MGT will be used to transmit a signal, on optical fibre, if any of the scintillators has fired. The third board will elaborate the coincidence and send the resulting signal to the KLOE trigger system.

[13]This device is a serial transceiver capable of transmitting and receiving data with a rate going from 100 Mb/s up to 6.5 Gb/s.

On the other hand, in the stand-alone mode, signals coming from the 28 scintillators will be divided into 8 groups. The logical OR operation will be performed for all the members of each group so to obtain 8 signals[14]. The 8 fast LVDS outputs will be used to deliver these "OR signals" to the third HET-DACQ board. This time, instead of sending a signal to the KLOE trigger system, the third board will be receiving one from it. In fact, as we have previously explained in Sec. 3.6, in case of a single energy deposit in the KLOE calorimeter (EmC) the $T1$ signal is not asserted and we may loose many physics events. For this reason, KLOE will provide the third board with a signal indicating a single energy deposit. In this way the board has information about the presence and the energy of the leptons in the final state plus the fact that a photon has been detected in the EmC. Thanks to this information the board can acquire significant physics data without any interference with KLOE trigger system.

### The HET-DACQ printed circuit board

The design of the PCB of the HET-DACQ has been a complex task. A detailed description of this work would risk to be tedious and goes far beyond the scope of this thesis. In this paragraph a brief description of the PCB is given.

The V5 FPGA is connected to all the peripherals on the board. To this end wires are routed from the FPGA to the outside. The complexity of the routing lies in the tiny pitch between the more than 1000 vias[15] below the FPGA and in the great number of connections needed. More specifically, the pitch of the vias is only 39 mils[16]. Vias have a diameter of 10 mils, leaving a gap available for routing of 29 mils. Due to the big number of wires that need to be routed to the outside, among which many differential pairs, we

[14] Groups will be formed taking into account which zone of the detector is more sensitive to interesting physics channels, such as $\pi^0$production (see for example Fig. 3.15 on Pag. 58).

[15] A via is a vertical electrical connection between different layers of conductors in a PCB. It consists of two pads, in corresponding positions on different layers of the board, that are electrically connected by a hole through the board.

[16] The "mil" is the thousandth part of an inch, equal to 0.0254 mm.

did need to route at list two wires within this gap. For these reasons, the width of the wires and the minimum distance between them has to be set to the value of 4 mils (0.1 mm), making the design and the realisation of the PCB very critical.

| | | |
|---|---|---|
| 1 | Component soldering and routing layer | Green |
| 2 | Digital and analogue ground plane | |
| 3 | Power plane | |
| 4 | Routing layer: input and DDR lines | Pink |
| 5 | Routing layer: VME, DDR, Ethernet, and RS232 lines | Cyan |
| 6 | Power plane | |
| 7 | Power plane | |
| 8 | Routing layer: Optical link, DDR, and flash memory lines | Yellow |
| 9 | Routing layer: KLOE signals, DDR, VME, USB | Gray |
| 10 | Power plane | |
| 11 | Digital ground | |
| 12 | Component soldering and routing layer | Red |

***Table 5.4:*** *Description of the 12 layers of the* HET-DACQ *board. In the third column, the colour of the layer drawn in Fig. 5.18 is indicated.*

Moreover, several lines need to be time-equalised, such as the input signals, the DDR2 lines, and some of the Ethernet lines. The most demanding interfaces are:

- RAM connector: 72 single-ended + 8 differential pairs (equalised);
- Synchronous RAM connection: 40 single ended lines;
- Input signals: 32 differential pairs (equalised $\sim 10$ ps);
- DAΦNE fiducial and KLOE signals: 6 differential pairs;
- VME interface: 77 single ended lines (poorly equalised $\sim 1$ ns).

In order to equalise the transmission lines and to guarantee a controlled and uniform impedance along them, the CADENCE *Allegro PCB design* software was used. This advanced tool, allowed us to set all the constraints we needed (impedance, timing, etc.) and to check if they were fulfilled. Allegro also provides an automatic routing tool, but it could not handle the complexity of this board.

In order to route such a big amount of wires, the HET-DACQ board has got 4 internal routing layers, on which all the routing is carried out in order to shield conductors from noise coming from external electromagnetic fields. Wires on every layer are transmission lines and we must guarantee a specified and uniform impedance for each of them. For this reason routing layers are interspersed with 6 ground or power planes. Therefore the HET-DACQ board is composed of a stack of 12 layers reported in Tab. 5.4. In Fig. 5.18 the PCB layout of the board is depicted, different colours stand for different layers. The Power and ground planes are not shown in order to make the drawing readable. In Fig. 5.19 a picture of the board is shown.

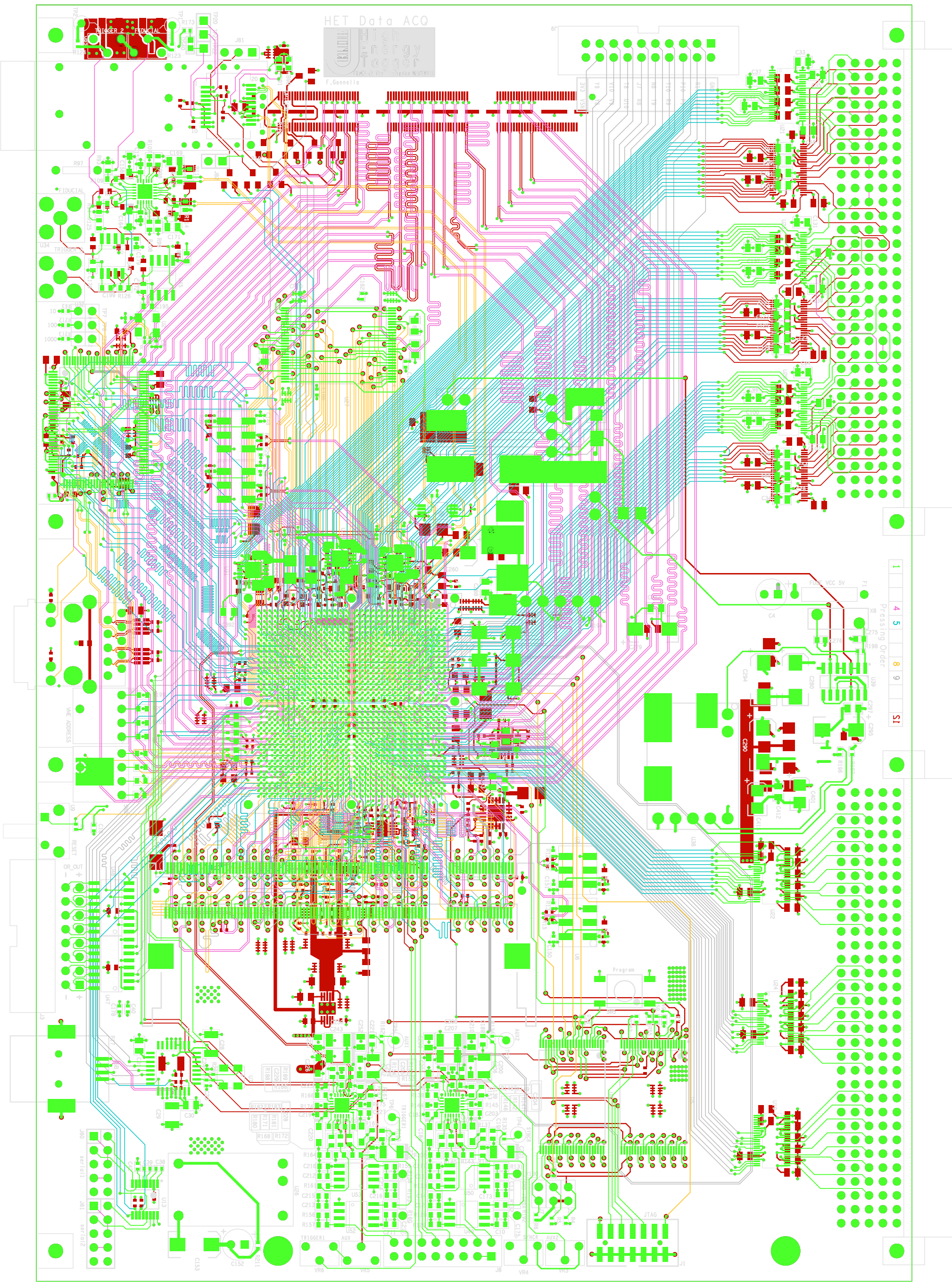

***Figure 5.18:*** *Routing layout of the* HET *data acquisition board. In order to make the layout readable, only the 6 routing layers are shown.*

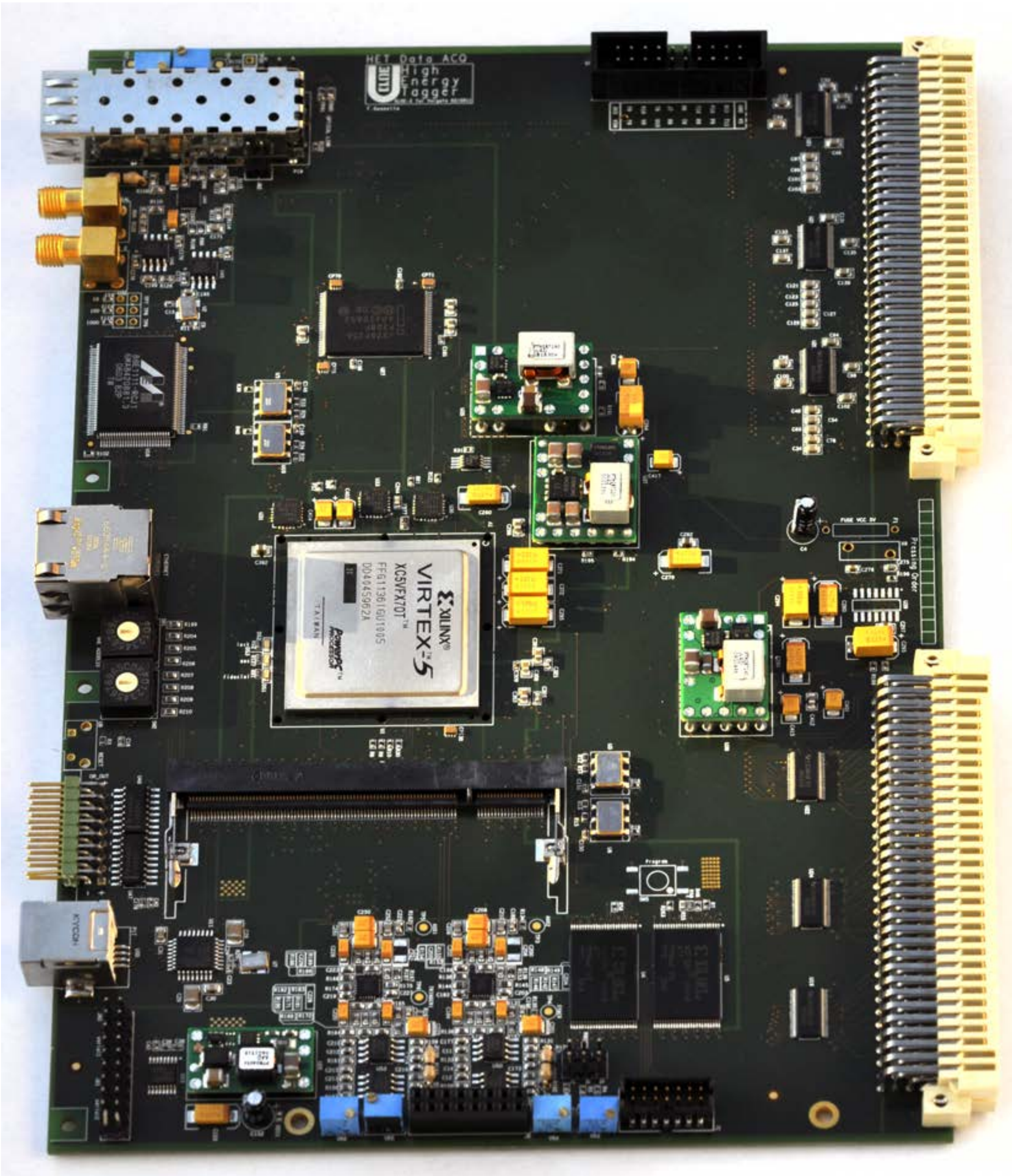


*Figure 5.19: A picture of the HET data acquisition board.*

## 5.3 Slow control system

In order to guarantee the proper functioning of the HET detector and its acquisition system, a set of parameters must be set and monitored or simply kept under control. These parameters are:

- distance between the detector and the beam line;
- High Voltages supplied to photomultipliers;
- proper functioning of photomultipliers (gain, quantum efficiency);
- environment temperature next to front-end boards;
- threshold voltages supplied to the discrimination and shaping boards.

All the hardware dedicated to handle this kind of tasks is usually referred to as *slow control*. We designed and built a single board which manages these tasks, called *Slow Environment Control System* (SECS) board. The SECS board communicates with the KLOE slow control system, through the Ethernet interface. In this way, all HET parameters can be read out and set through the KLOE slow control system web page. In this section a brief description of this board is given. The SECS board is a 6U VME board (dimensions: 160 mm × 233 mm) but as the discrimination board, it only takes power supply from VME crate and does not use the communication bus. It is equipped with a PIC 18F97J60 microprocessor together with all the hardware needed for communication with the external devices such as:

- HET detector step motors;
- Temperature sensors mounted on every HET front-end boards;
- DACs mounted on the mezzanine boards;
- Motorola MVME 6100 board, controlling all the VME crate;
- current generator used to drive a led during PMTs calibration;
- High Voltage system controller.

The SECS board communicates with the HET step motors (see Sec. 4.3) via the SPI interface. Therefore, it is possible to move the HET detectors and monitor their position remotely, through the KLOE slow control web page.

All the temperature sensors mounted on the front-end boards (see Sec. 5.1.1) are connected to the ADCs mounted on the SECS board. The PIC microprocessor periodically monitors these devices and communicates the read out values to the KLOE slow control system, for a continuous temperature monitoring.

The SECS board can communicate with DACs mounted on the mezzanines via the SPI interface, that is directly handled by the PIC microprocessor. Thanks to a custom flat cable one SECS board is connected to both the mezzanines in the HET station. One board can program two DACs for a total of 32 electronics channels i.e. 64 threshold values, high and low for each channel. Connections with MVME 6100 board and LED driver (trough serial interface) and with High Voltage system (through Ethernet interface) are useful for the photomultiplier calibration described in the following section.

### 5.3.1 Photomultipliers calibration

In order to keep the PMTs performances under control, a PMT calibration procedure has been established. This procedure will take place during the KLOE calibration, when no data is being recorded. Before the procedure starts, the SECS board connects to the Motorola MVME 6100 board[17], via Ethernet interface, and takes control of the VME bus. The SECS board can now access the QDC (CAEN `V792AC`) module, installed in the VME crate, into which the amplified outputs of the HET front-end boards are connected

[17] The MVME 6100 board controls the VME bus. Normally it is used to download data from the data acquisition board (see sec. 5.2.3) and it is handled by the KLOE acquisition program. Nevertheless, during KLOE calibration, the board is idle and it is available to be controlled by the SECS board.

(see sec. 5.1.1).

At the beginning of the calibration procedure, the SECS board arms the QDC module then triggers the current pulse generator, driving the Light Emitting Diode (LED), installed in the HET detector. This device emits a set of light pulses, channelled into optical fibres. Each one of these fibres ends onto a light guide, just in front of the photomultiplier (see sec. 4.3). Thanks to these controlled light pulses, PMTs are stimulated with a known amount of light and the charge values of their output signals, amplified by the front-end boards, are recorded by the QDC module. The charge distributions carry important information about the performances of all the PMTs in the detector. There are many ways to exploit this information in order to calibrate these devices and, on top of that, check if any of the PMTs is damaged and prevent the corruption of physics data. In the following, we will briefly describe an example of calibration procedure that resulted from a preliminary study of the photomultipliers.

Performing a Gaussian fit of the QDC spectrum, we extract the mean $\bar{x}$ value and the standard deviation $\sigma$. The charge of the output signal is proportional to the number of photoelectrons $N_e$ emitted by the cathode:

$$\bar{x} = kN_e \tag{5.4}$$

The electron emission process inside a photomultiplier follows the Poisson distribution, so we can write:

$$\sigma = k\sqrt{N_e} \tag{5.5}$$

where $k$ is clearly the same as in Eq. 5.4. From equations 5.4 and 5.5, it is straightforward that the number of photoelectrons can be evaluated with the following:

$$N_e = \left(\frac{\bar{x}}{\sigma}\right)^2 \tag{5.6}$$

Acquiring QDC distribution for various light intensities, it is possible to realise the plot in figure 5.20. Please note that the current $I_{out}$, supplied to the LED, is generated by a voltage controlled driver circuit. This circuit is perfectly linear, so if we call $V_{in}$ the voltage provided to the driver and $N_\gamma$ the number of photons emitted by the LED, we obtain:

$$V_{in} \propto I_{out} \propto N_\gamma. \tag{5.7}$$

Without loss of generality, in figure 5.20 we reported $V_{in}$ instead of $N_\gamma$. Performing a linear fit is now possible to extract the $p1$ parameter, i.e. the slope of the line, for each one of the PMTs. This parameter characterises each

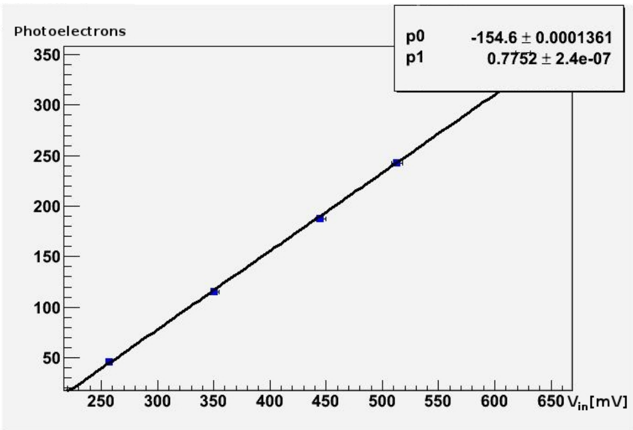


***Figure 5.20:*** *Plot of number of photoelectrons vs voltage applied to LED driver. The LED driver is perfectly linear, thus the number of photons emitted by the LED is directly proportional to* $V_{in}$.

photomultiplier. Knowing the $p1$ parameter characterising all the PMTs, it is enough to properly set the High Voltage to equalise them. Moreover, by periodically checking the variation of this parameter, it is possible to monitor the ageing or the damaging of the photo-cathodes and compensate this effect by slightly increasing the HV, when possible or, in the worst case, replacing the damaged photomultiplier.

## 5.4 Electronics tests

In this section all the tests carried out on the boards of the HET front-end and acquisition system are discussed in detail.

### 5.4.1 HET front-end test

A test of the HET front-end board has been performed. We delivered a sinusoidal signal of known amplitude (abot 50 mV) to the board by means of a high frequency (up to 2 GHz) function generator (Agilent 4420B).
We acquired with an oscilloscope (Tektronix DPO7254, having 2.5 GHz of

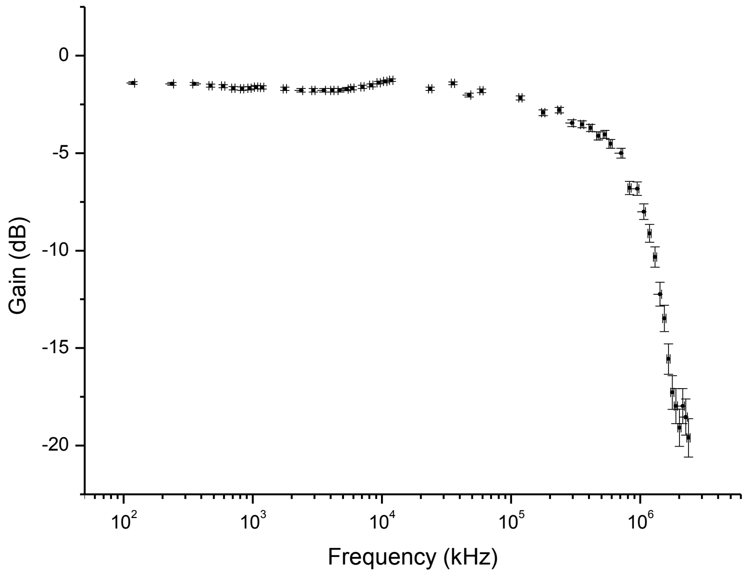


***Figure 5.21:*** *Results of characterisation study carried out on the HET front-end board connected with a 5-meter* 50 Ω *cable.*

bandwidth and a sample rate of 40 GS/s) the fast output signal $V_{out}$ from the front-end board, i.e. the output of the (LMH6559) buffer, as well as the input signal $V_{in}$. We measured the ratio $\frac{V_{out}}{V_{in}}$ as a function of the frequency $\nu$ in the range $100\,\text{kHz} \leq \nu \leq 2\,\text{GHz}$. In order to perform a realistic test, we connected the output of the front-end board to the oscilloscope by means of the same 50 Ω cable used in the HET detector having a length of about 5 m. The results of these measurements are shown in Fig. 5.21.

### 5.4.2 HET discrimination and shaping board efficiency test

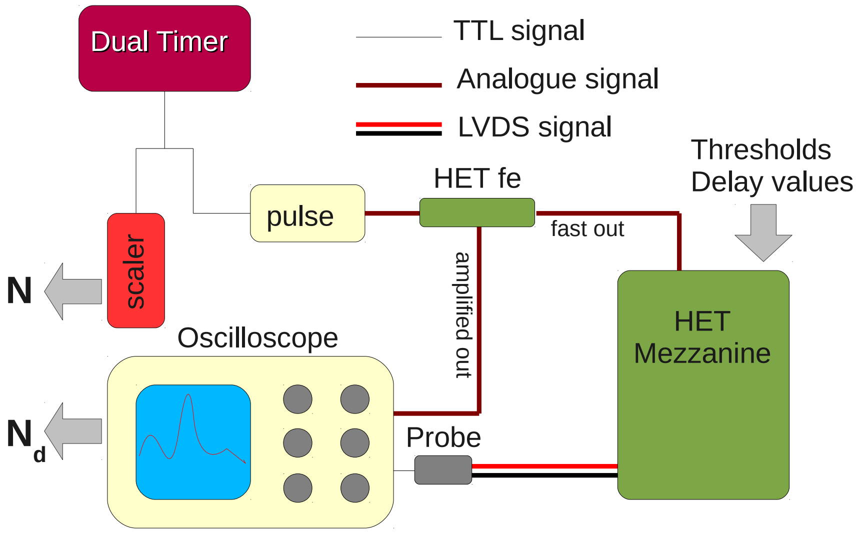


***Figure 5.22:*** *Scheme of the experimental setup for the efficiency test of the mezzanine.*

The main task of this test is to find the best tuning for the delay lines $\Delta t_t$ and $\Delta t_g$ (see Sec. 5.1.2). For doing this, we measure the efficiency of a channel of the discrimination and shaping board (also called mezzanine) for several input signals, high and low threshold values, and delay configurations.

#### Experimental setup

The procedure of this test is basically to deliver a number $N$ of pulses to a given channel of the mezzanine and to count the number of the discriminated pulses $N_d$. The ratio between these numbers is the efficiency of the channel:

$$\epsilon = \frac{N_d}{N} \tag{5.8}$$

Let us describe the experimental setup, shown in Fig. 5.22.
The input signal is generated by a pulse generator, triggered by a TTL signal, and delivered to a HET front-end board. The TTL signal is also connected to

a scaler which counts out the number $N$ of delivered pulses.
The fast output of the front-end board is connected to a channel of the mezzanine, while the amplified output is connected to the oscilloscope (Tektronix DPO7254).

The signal at the fast output of the front-end board, i.e. the input signal for the mezzanine channel, has he following characteristics:

- a rise time of about 1 ns;
- a total duration of about 2 ns;
- an amplitude of about −100 mV.

Let $-V_{in}$ be the amplitude of the input signal, so that we can refer to it as a positive value.
The LVDS output signal of the mezzanine is connected, through a differential probe, to the oscilloscope that is used as a scaler to count $N_d$.
In addition, the oscilloscope allows us to measure the value of the delay between the input signal and the output. We measured this delay for each threshold configuration, in order to keep under control the jitter due to the variation of the low threshold value, also called *time walk*.
Finally, we measure the root mean square for every set of measure of the time walk, in order to control the electronic jitter.

### Experimental results

As we said in section 5.1.2, the optimal configuration of the delay lines in the discrimination channels cannot be found only with theoretical calculations. In fact, the durations $\Delta t_t$ and $\Delta t_g$ can be widely tuned within the bound described in equation 5.1 on Pag. 90. In order to achieve the optimal delay configuration, several configurations had to be set up and tested. In the following, we report the results obtained with the optimal configuration and an example of what the efficiency plot looks like, if delay durations are not properly tuned.

In Fig. 5.23 the result of a non-optimal choice of delays is reported for a high threshold value of 40 mV. One can see that the efficiency reaches

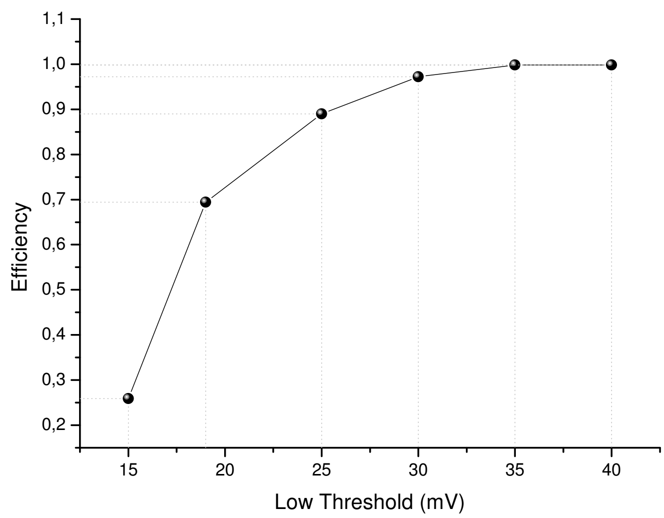


***Figure 5.23:*** *Efficiency test with a wrong tuning of delay lines. The high threshold value is set to* 40 mV *and* $V_{in}$ *is* 100 mV

100% only for low threshold values very similar to high threshold one. This is trivial because if the two thresholds are alike, each *timing* and *gate* choice leads to a correct timing of flip-flops and to the shaping of the output signal. Nevertheless the low threshold must be as low as possible in order to reduce the jitter; otherwise it would not make any sense to perform a dou-

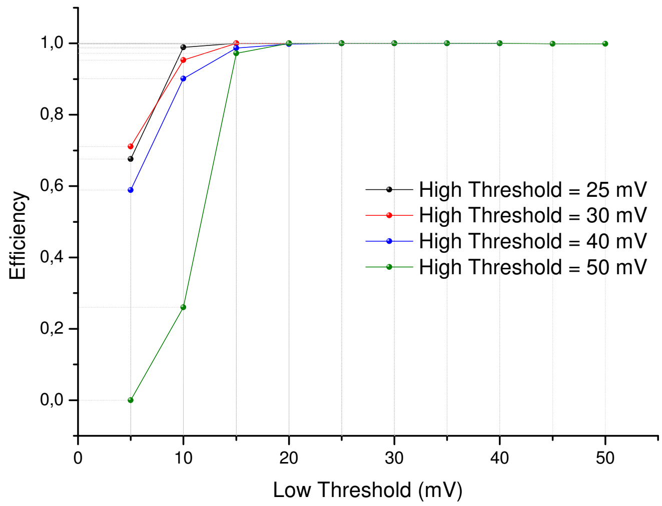


***Figure 5.24:*** *Efficiency test of a discrimination channel with* $\Delta t_t = 480\,\mathrm{ps}$ *and* $\Delta t_g = 620\,\mathrm{ps}$ *for varous values of high and low thresholds. The input signal amplitude is* $V_{in} = 100\,\mathrm{mV}$.

ble threshold discrimination.

In Fig. 5.24 the efficiency of the discrimination channel is reported for the optimal choice of the delay values: $\Delta t_t = 480\,\mathrm{ps}$ and $\Delta t_g = 620\,\mathrm{ps}$.

The total number $N$ of pulses delivered for each point in fig 5.24 is about 1000. So the relative error results about 3%.

For this delay configuration also the electronic jitter and time walk as a function of the low threshold value have been measured and are reported in figure 5.25.

One can see that the time walk increases almost linearly with the low threshold value, while it remains constant at various values of the high threshold. This result is the expected one, because the output signal starts as soon as the input signal exceeds the low threshold value, independently on the high threshold one. On the other hand, the electronic jitter, that is not necessarily due completely to our electronics, is always smaller than 100 ps. The jitter is root mean square of the over-all variation of the starting time of the output signal. This time is measured with respect to the TTL signal that triggers all the system. Every device in the experimental setup (dual timer,

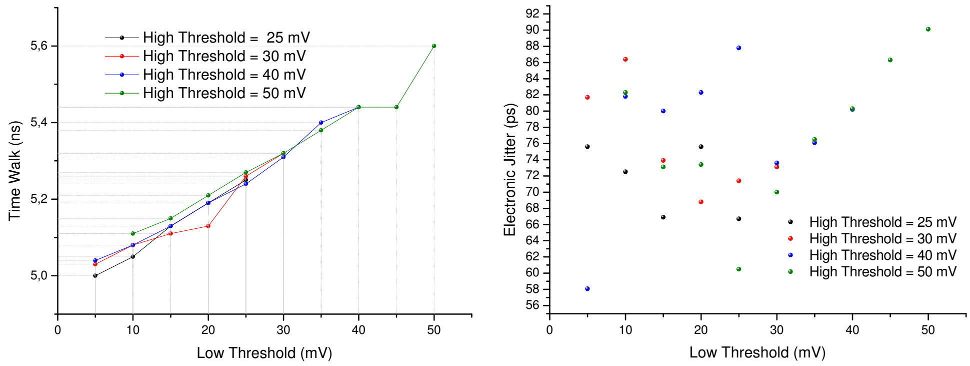


***Figure 5.25:*** *Results of a test of a channel of the discrimination and shaping board. On the left panel the time walk of the discriminated signal is plotted as a function of the low threshold value. On the right panel the electronic jitter is reported.*

pulse generator, oscilloscope) contributes to this jitter, thus we are confident that the jitter due to our electronics is less than 100 ps, which is the maximum reported in figure 5.25.

### 5.4.3 HET data acquisition board test

In this section all tests performed on the HET data acquisition board are described. First of all we characterised the Time to Digital Converter (TDC) implemented onto the Virtex 5 FPGA on the HET-DACQ board. During this test, all the LVDS input signals were generated with a digital pulse generator, implemented on a prototyping board equipped with another V5 FPGA. Then we analysed the VME communication capability of the board plugged into a Wiener VME64x crate.

### V5 TDC performances

Several tests have been carried out, in order to characterise the TDC implemented on the Virtex 5 (V5) FPGA embedded in the HET data acquisition board. The parameters taken into account are:

- Resolution;
- Precision;
- Linearity.

The resolution of a TDC is the smallest time interval which can be resolved by a single measurement. In our case, thanks to the 4x-oversampling technique, the time resolution is $\frac{1}{4}T_{clk}$. The crystal, we chose to clock the V5 FPGA with, has a frequency of 100 MHz which is internally multiplied by a factor 4, so we obtain a $T_{clk} = 2.5\,\text{ns}$. The time resolution of one single TDC measurement is 625 ps. Because of the linear interpolation technique, the uncertainty of a global TDC measurement is the sum of the uncertainties of the three measurements (from Eq. 5.3 on page 97): $\Delta t_1$, $\Delta t_2$, and $\Delta t_{12}$. The uncertainty of $\Delta t_{12}$ is only due to the clock jitter and can be neglected. So the resulting uncertainty for a global TDC measurement is 1.25 ns, or ±625 ps.

The TDC precision is the capability of the instrument of giving always the same result, when measuring the same quantity. Quantitatively it can be expressed by the standard deviation of the distribution of a series of measures of the same quantity. It is due to two contributions added in quadrature:

$$\sigma_{TDC} = \sqrt{\sigma_Q^2 + \sigma_R^2} \tag{5.9}$$

where $\sigma_Q$ is the contribution due to the quantisation uncertainty and $\sigma_R^2$ is the contribution due to intrinsic parameters of the TDC such as non-linearity, internal clock jitter or temperature-related effects. The quantisation uncertainty can be theoretically evaluated. For a set measurements

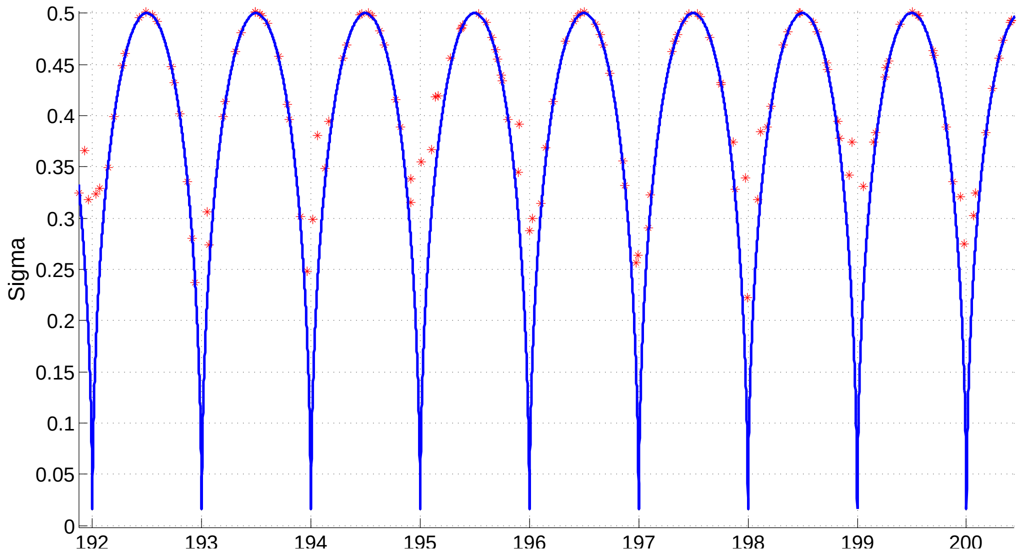


***Figure 5.26:*** *Time precision of the TDC implemented onto the Virtex 5 FPGA as a function of the measured value.*

performed we can write:

$$\sigma_Q = \sqrt{c(1-c)} \tag{5.10}$$

where $c$ is the decimal part of the value we are measuring in TDC channels. A good estimation of this value is the decimal part of the mean value of the distribution of the set of performed measurements. In figure 5.26, results of measurements made on the data acquisition board are reported. The red asterisks are the measured values of $\sigma_{TDC}$ and solid blue line is the theoretical quantisation contribution. When $c = 0$, i.e. at integer values on the horizontal axis, the quantisation contribution vanishes and the value of $\sigma_{TDC}$ is due only to $\sigma_R$. On the other hand, when the quantisation uncertainty is maximum, there is no apparent contribution from $\sigma_R$. From these results, we can conclude that the precision of the TDC is only due to the quantisation uncertainty.

In order to check the linearity of the TDC, we carried out several sets of measurements of known time intervals. In figure 5.27a the results of these measurements are shown. The mean values of series of ∼1000 measurements are reported against the respective real values. For an ideal TDC, the plot in figure, referred to as the *input-output characteristics*, would be a perfect straight line. We reported the deviations from the linearity in Fig. 5.27b. From the results obtained we can conclude that the non-linearity of the TDC is less than 50 ps.

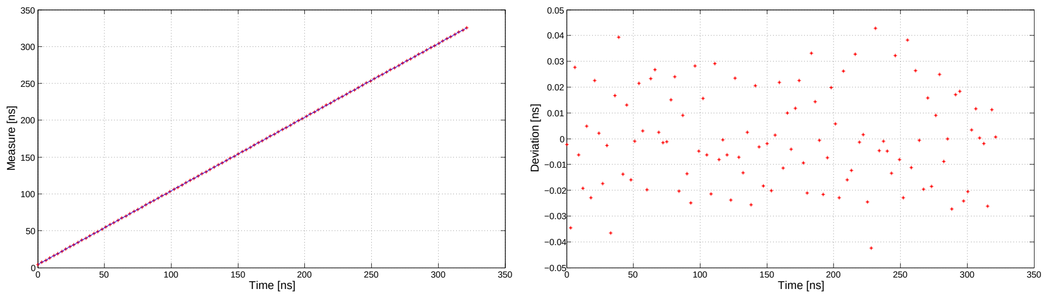


**(a)** Measured versus real time intervals. **(b)** Deviation of the input-output characteristics from the linearity.

***Figure 5.27:*** *Results of the linearity test of the TDC implemented onto the Virtex 5 FPGA.*

### VME block data transfer test

The VME communication capability of the HET data acquisition board was analysed. The communication standard followed by the board is the “double-edge” VME with 32bit address words and 64bit data words (2eVME64x in A32/D64 mode) [34, 35]. According to this standard, 64bit-words are transferred on both the rising and falling edges of the VME hand-shaking signals.

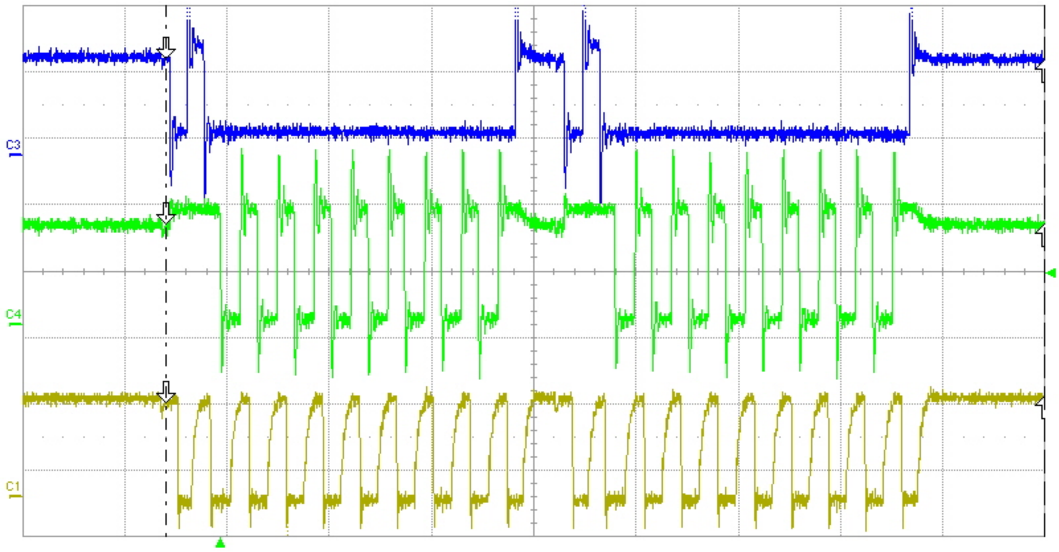


*Figure 5.28:* *VME communication test result. The blue and the green signals are data strobe generated by the MVME 6100 board controlling the bus. The yellow signal is the data acknowledge generated by the* HET *data acquisition board. The time scale, on the horizontal axis, is* 500 ns/div. *During the data transfer, thirty-two* 8 Byte-*words were transferred in* 3.5 μs.

To this end, the board under test was plugged into a VME64x crate, controlled by a Motorola MVME 6100 (the same board controlling the VME bus in the crate used for real data acquisition). A VME block transfer (MBLT)[18] was started while an oscilloscope was connected to the VME bus and some signals were acquired: 2 data strobe signals, generated by the MVME 6100, and 1 data acknowledge signal, generated by the HET acquisition board. From the figure, one can see that a total of 32 edges (rising of falling) are present in the data strobe signal, after the addressing phase. This means that 32 8 Byte-words were transferred in 3.5 μs, thus the transfer rate results of about 70 MB/s.

[18] A VMEbus BLock Transfer (BLT) consists of a single Address cycle followed by up to a 256 Byte Data transfer (in ether 8, 16, or 32 bit segments). VME64 added the Multiplexed BLock Transfer (MBLT). The HET acquisition board, performs MBLT which uses all 32 data bits and all 32 address bits to transfer 64 data bits at once over the bus.

### 5.4.4 Acquisition chain test

A test of the complete acquisition chain was carried out. A digital signal with a period of about 324 ns (the same as the DAΦNE fiducial signal, see Sec. 1.2.1) was generated by means of a dual timer. One copy of the signal was delivered to the HET-DACQ board and another copy was used to trigger a pulse generator. The delay between the rising edge of the fiducial signal and the pulse was fixed by the length of the cables used to set up the test. The generated pulse, having the same characteristics as PMT signals (see Fig. 4.10 on Pag. 71), was sent to several channels, one at a time, of the HET discrimination and shaping board. The latter was connected to the HET-DACQ board which measured the time of arrival of the discriminated signals with respect to the rising edge of the dual timer signal. The low threshold value of the discriminator was set to the value of 20 mV during this whole test.

#### Variation of the input signal amplitude

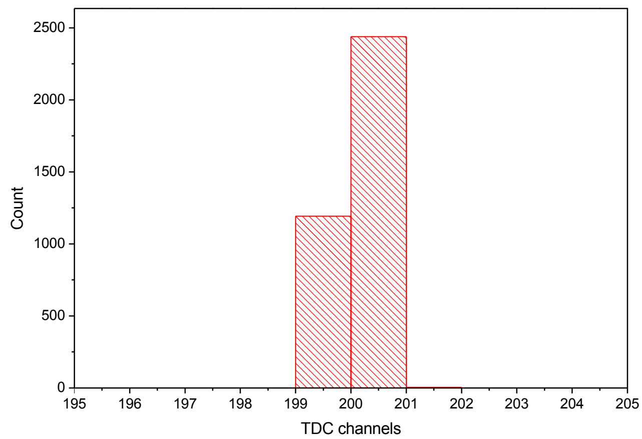


***Figure 5.29:*** *Time distribution acquired with an input signal amplitude varying from* 300 mV *to* 700 mV*. The moments of the distributions are:* $\bar{t} = 199.67$, $\sigma = 0.47$*. One TDC channel is equal to* 625 ps.

The amplitude of the signals coming from PMTs can vary for several reasons: particle hitting on the edge of the scintillator and releasing a smaller amount of energy, photo-cathode degradation, statistical fluctuations in the electronic cascade, etc. In order to check if this would affect the precision of our measurement, we acquired time distributions varying the amplitude of the signal between 300 mV and 700 mV. Figure 5.29 shows the obtained results, all values are in TDC channels. The mean of the distribution is $\bar{t} = 199.67$ and its standard deviation (s.d.) $\sigma = 0.47$. If we compute the theoretical quantisation s.d. described in Eq. 5.10 (on Pag. 123), we obtain: $\sigma_Q = \sqrt{.67(1-.67)} \simeq 0.47$. We can therefore conclude that nor the discriminator nor the variation of the amplitude of the input signal, introduce any considerable jitter.

### Variation of the high threshold voltage

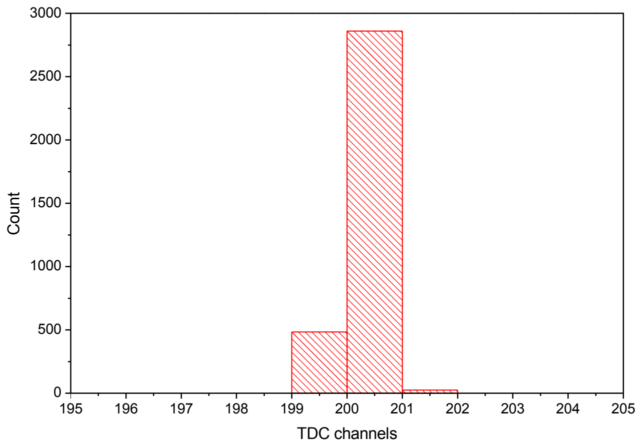


***Figure 5.30:*** *Time distribution acquired with high threshold assuming three values:* 124 mV, 93 mV, *and* 78 mV. *The moments of the distributions are:* $\bar{t} = 199.86$, $\sigma = 0.36$. *One TDC channel is equal to* 625 ps.

During KLOE data taking, we might need to increase the value of the high threshold because of noise. In order to ensure that this procedure does not worsen the precision of our measurements, we acquired time distributions at various values of the high threshold, see Fig. 5.30. The mean value and standard deviation of the distribution are (in TDC units): $\bar{t} = 199.86$,

$\sigma = 0.36$. In this case, if we compute the theoretical s.d. we obtain $\sigma_Q \simeq 0.35$. As we have already seen in the TDC test (see Sec. 5.4.3), the measured value is slightly greater. This is probably due to the value of $\bar{t}$ being so next to its integer part: in this case the quantisation uncertainty gets smaller and the theoretical prediction does not longer hold.

### Variation of the time interval under measurement

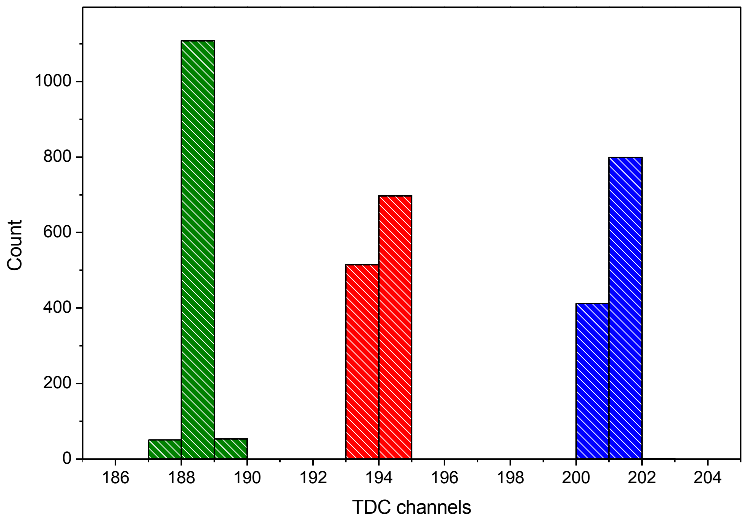


***Figure 5.31:*** *Time distributions acquired for three values of the time interval under measure. The moments of the distributions are:* $\bar{t}_1 = 188.00$, $\sigma_1 = 0.29$; $\bar{t}_2 = 193.58$, $\sigma_2 = 0.49$; *and* $\bar{t}_3 = 200.65$, $\sigma_3 = 0.48$. *One TDC channel is equal to* 625 ps.

As we have seen, the precision of the TDC (and, in general, of any measuring instrument) is a function of the real value the instrument is measuring. For this reason, measuring always the same time interval could be misleading. In order not to do so, we varied the length of the cable going from the dual timer to the pulse generator. The time distributions, shown in Fig. 5.31, have been acquired for three cable lengths. By looking at the histograms and at the distribution moments reported in the caption, we can notice that they reproduce the results obtained before, during the TDC test (see Fig. 5.26 on Pag. 123). Let us consider the decimal part of the 3 mean values: $c_1 = .00$, $c_2 = .58$, and $c_3 = .65$ and compute the expected quantisation standard deviations: $\sigma_{Q1} = .00$, $\sigma_{Q2} = .49$, and $\sigma_{Q3} = .48$. The values of $\sigma_{Q2}$ and $\sigma_{Q3}$ are in perfect agreement with the quantisation s.d. Since $\bar{t}_1$ is an integer $\sigma_{Q1} = 0$ but, as it happened in the TDC test, the global s.d. is dominated by the systematic uncertainties intrinsic in the TDC (see Eq. 5.9 on Pag. 122) and its value rarely goes below 0.3. Again we can be sure that the whole electronic chain does not worsen the time precision.

### Global test of the acquisition channels

At last, we carried out a global test delivering a given number of pulses to each channel of the discriminator, having fixed values of high (80 mV) and low (20 mV) threshold. In Fig. 5.32 the time distributions obtained for a sample of 3 channels are shown by way of illustration. In this case

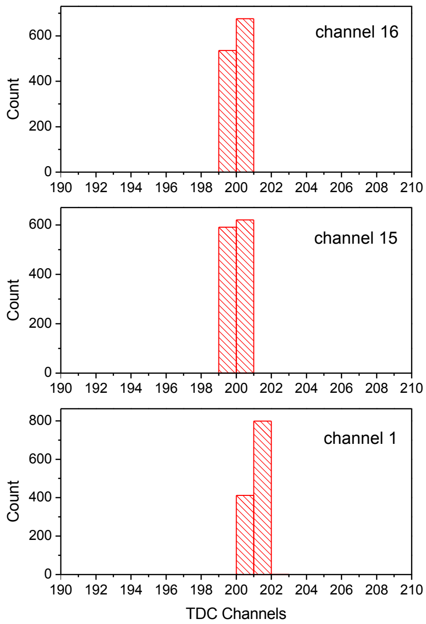


***Figure 5.32:*** *Time distributions obtained for three different channels of the acquisition system. The moments of the distributions are:* $\bar{t}_{16} = 199.56$, $\sigma_{16} = 0.50$; $\bar{t}_{15} = 199.51$, $\sigma_{15} = 0.50$; *and* $\bar{t}_1 = 200.65$, $\sigma_1 = 0.48$. *One TDC channel is equal to* 625 ps. *One can notice that channel 1 is slightly delayed with respect to channel 15 and 16.*

as well, all the measured standard deviations are in perfect agreement with the quantisation uncertainty.

One more thing is worth to be pointed out: it is apparent that the channel 1 distribution is peaked around a slightly higher value. The reason for this lies in the way the discrimination channels are connected to the front panel.

While channels from 9 to 16 are directly soldered to the SMA connectors on the panel, channels from 1 to 8 are connected to the SMAs through hard copper-shielded cables (visible in Fig. 5.11 on Pag. 95), having a length of about 15 cm. This difference among the channels is not a big issue, because it can be compensated internally to the FPGA.

### Final considerations

We can be satisfied with the obtained results. Indeed, as long as the measured standard deviations do not exceed the value of 0.5 TDC channels, we are quite sure that the acquisition chain is not affecting the precision of our TDC measurement. Taking, as well, into account the uncertainty of about 250 ps due to the scintillators and photomultipliers previously tested (see the results obtained in Sec. 4.5.2), we obtain the global value of

$$\sigma_{TOT} = \sqrt{(625\,\text{ps})^2 + (250\,\text{ps})^2} \simeq 700\,\text{ps}.$$

We can therefore conclude that the HET front-end and the acquisition system perfectly fulfil their requirements since the needed resolution to distinguish leptons belonging to consecutive bunches at DAΦNE is 2.7 ns.

# Conclusions

The High Energy Tagger detector has been designed and built. It will allow the KLOE-2 collaboration to study $\gamma\gamma$ physics, within the framework of DAΦNE, recently upgraded in luminosity.

The whole electronic chain has been realised and all the performed test confirmed that the three boards fulfil their requirements. The measured bandwidth of the front-end board resulted compatible with the typical signals coming from photomultipliers.
The discrimination and shaping board, equipped with our self-made delay lines, operates with high efficiency and low jitter.
The VME interface of the data acquisition board works with a satisfactory transmission rate. This rate is compatible with the requirements imposed by the KLOE acquisition system.
At last, the time precision of the TDC, implemented into the Virtex 5 FPGA, has been proven to be due to the sole quantisation uncertainty, yielding a precision of 625 ps. Moreover, we have shown that the jitter introduced by the front-end boards and discriminators does not affect the global precision of the whole electronic chain.

The results of the test beam, performed on scintillators and photomultipliers, revealed an uncertainty of less than 250 ps. Therefore the overall time resolution of the detector does not exceed the value of 700 ps. This is a satisfactory achievement, considering that the most critical task of the High Energy Tagger is to disentangle events coming from two consecutive DAΦNE bunches, which are 2.7 ns apart.

The $5\,\mathrm{fb}^{-1}$ of data that are going to be acquired during the upcoming STEP-0 phase, will give us the possibility to perform two novel measurements: the $\pi^0 \to \gamma\gamma$ decay width and the $\gamma^*\gamma \to \pi^0$ transition form factor. The former will be performed reaching an accuracy of the 1% level, the latter will shed new light onto the unexplored low-momentum region.
Furthermore, these two measurements will have an impact on the uncertainty on the value of the anomalous magnetic moment of the muon by a factor $\sim 2$.

As future development, thanks to the great capability of the data acquisition board, we will be able to implement novel trigger strategies. These strategies will allow the High Energy Tagger to acquire data independently from the KLOE data acquisition system. This new data acquisition mode will further increase the efficiency of the previously mentioned measurements.

# Acknowledgements

First of all, I would like to thank Roberto Messi and Dario Moricciani because, during these three years, they behaved more like friends (parents sometimes) than bosses.
Roberto taught me that when you do something, whatever it is, you have to be careful to all the details and think of what may happen before it does."Those are all inductances!", he told me many times.
On the opposite, Dario showed me that, most of the times, complicated things are not that complicated after all.

I wish to deeply thank Danilo Babusci, because he has done a lot for me, much more than he was supposed to. Every time I left his office, I was somehow richer. I knew something more, not only about physics, but also about life, LNF inside-gossip, and ageing-related issues.

I wish to express my sincere gratitude to Rachele Di Salvo, who helped me far beyond her duty to start this Ph.D. and to conclude it.

I wish to thank Alessandro Balla and Maurizio Gatta for putting up with me and patiently helping me with all my electronic boards, in exchange for a few coffees.

I would like to thank Ennio Turri for his availability and his expertise. During the long conversations with him, I happened to learn things on the most diverse topics. I also happened to learn what a good listener I am.

I wish to thank very much Mauro Iannarelli for the help he gave me during these three years, for his patience, his calmness, and for his wisdom. Speaking with Mauro is an infallible cure for anxiety.

I want to thank Antonello Volpi, my high school physics teacher. If I have come this far, it is because of him.

Thanking my friends Matteo Mascolo, Lorenzo Iafolla, Roberto Di Nardo, Flavio Archilli and Manuele Martini goes beyond the scope of this thesis and would risk to be boring and mawkish.

I wish to thank Cristina for being with me and making me happy, because "Physics isn't the most important thing. Love is."

At last, I wish to thank my family, also referred to as: Peppe, Patrizia, Emanuela and Alessandra.

# List of Figures

# List of Tables

# Bibliography


[1] Johannes C Sens. *Critical issues and prospects for future work: in photon-photon collisions.* CERN-EP, 88-99:34, Aug 1988.

[2] M. Zobov, D. Alesini, M. E. Biagini et al. *Test of "crab-waist" collisions at the da$\phi$ne $\phi$ factory.* Phys. Rev. Lett., 104(17):174801, Apr 2010. doi:10.1103/PhysRevLett.104.174801.

[3] G. Amelino-Camelia, F. Archilli, D. Babusci et al. *Physics with the kloe-2 experiment at the upgraded da$\phi$ne.* The European Physical Journal C - Particles and Fields, 68:619–681, 2010. ISSN 1434-6044. 10.1140/epjc/s10052-010-1351-1.

[4] D. Babusci et al. *The Low Energy Tagger for the KLOE-2 experiment.* Nucl. Instrum. Meth., A617:81–84, 2010. doi:10.1016/j.nima.2009.09.110.

[5] M. R. Pennington. *Exclusively exclusive final states in two photon collisions.* Acta Phys. Polon., B37:857–866, 2006.

[6] H. Marsiske, D. Antreasyan, H. W. Bartels et al. *Measurement of $\pi^0\pi^0$ production in two-photon collisions.* Phys. Rev. D, 41(11):3324–3335, Jun 1990. doi:10.1103/PhysRevD.41.3324.

[7] Irinel Caprini, Gilberto Colangelo, and Heinrich Leutwyler. *Mass and width of the lowest resonance in QCD.* Phys. Rev. Lett., 96:132001, 2006. doi:10.1103/PhysRevLett.96.132001.

[8] E. M. Aitala, S. Amato, J. C. Anjos et al. *Experimental evidence for a light and broad scalar resonance in $d^+ \to \pi^-\pi^+\pi^+$ decay*. Phys. Rev. Lett., 86(5):770–774, Jan 2001. doi:10.1103/PhysRevLett.86.770.

[9] M. Ablikim et al. *The $\sigma$ pole in $J/\psi \to \omega\pi^+\pi^-$*. Phys. Lett., B598:149–158, 2004. doi:10.1016/j.physletb.2004.07.052.

[10] J. Gasser, M.A. Ivanov, and M.E. Sainio. *Low-energy photon-photon collisions to two loops revisited*. Nuclear Physics B, 728(1-3):31 – 54, 2005. ISSN 0550-3213. doi:DOI:10.1016/j.nuclphysb.2005.09.010.

[11] S. Bellucci, J. Gasser, and M. E. Sainio. *Low-energy photon-photon collisions to two-loop order*. Nuclear Physics B, 423(1):80 – 122, 1994. ISSN 0550-3213. doi:DOI:10.1016/0550-3213(94)90566-5.

[12] Luciano Maiani, Giulia Pancheri, and Nello Paver. *The second DA$\phi$NE physics handbook*. Frascati Naz. Lab. INFN, Frascati, 1995.

[13] F. Nguyen, F. Piccinini, and A.D. Polosa. *$e^+e^- \to e^+e^-\pi^0\pi^0$ at da$\phi$ne*. The European Physical Journal C - Particles and Fields, 47:65–70, 2006. ISSN 1434-6044. 10.1140/epjc/s2006-02567-9.

[14] T. Oest et al. *Measurement of resonance productions in the reactions $\gamma\gamma \to \pi^0\pi^0$ and $\gamma\gamma \to \pi^0\eta$*. Z. Phys., C47:343–352, 1990. doi:10.1007/BF01565857.

[15] D. Babusci, H. Czyz, F. Gonnella et al. *On the possibility to measure the $\pi^0 \to \gamma\gamma$ decay width and the $\gamma * \gamma \to \pi^0$ transition form factor with the KLOE-2 experiment*. arXiv:1109.2461 Submitted to Physics Letters B, 2011.

[16] D. A. Williams, D. Antreasyan, H. W. Bartels et al. *Formation of the pseudoscalars $\pi^0$, $\eta$, and $\eta$' in the reaction $\gamma\gamma \to \gamma\gamma$*. Phys. Rev. D, 38:1365–1376, Sep 1988. doi:10.1103/PhysRevD.38.1365.

[17] Henryk Czyz and Sergiy Ivashyn. *Ekhara: A monte carlo generator for $e^+e^- \to e^+e^-\pi^0$ and $e^+e^- \to e^+e^-\pi^+\pi^-$ processes*. Computer Physics

Communications, 182(6):1338 – 1349, 2011. ISSN 0010-4655. doi: DOI:10.1016/j.cpc.2011.01.029.

[18] F. Ambrosino, A. Antonelli, M. Antonelli et al. *Data handling, reconstruction, and simulation for the kloe experiment.* Nuclear Instruments and Methods in Physics Research Section A: Accelerators, Spectrometers, Detectors and Associated Equipment, 534(3):403 – 433, 2004. ISSN 0168-9002. doi:10.1016/j.nima.2004.06.155.

[19] K Nakamura and Particle Data Group. *Review of particle physics.* Journal of Physics G: Nuclear and Particle Physics, 37(7A):075021, 2010.

[20] H.-J. Behrend, L. Criegee, J. H. Field et al. *A measurement of the $\pi^0$ $\eta$ and $\eta'$ electromagnetic form factors.* Zeitschrift f ur Physik C Particles and Fields, 49:401–409, 1991. ISSN 0170-9739. 10.1007/BF01549692.

[21] M. Knecht and A. Nyffeler. *Resonance estimates of $\mathcal{O}(p^6)$ low-energy constants and qcd short-distance constraints.* The European Physical Journal C - Particles and Fields, 21:659–678, 2001. ISSN 1434-6044. 10.1007/s100520100755.

[22] J. Gronberg, T. S. Hill, R. Kutschke et al. *Measurements of the meson-photon transition form factors of light pseudoscalar mesons at large momentum transfer.* Phys. Rev. D, 57:33–54, Jan 1998. doi:10.1103/PhysRevD.57.33.

[23] B. Aubert, Y. Karyotakis, J. P. Lees et al. *Measurement of the $\gamma\gamma^* \to \pi^0$ transition form factor.* Phys. Rev. D, 80:052002, Sep 2009. doi:10.1103/PhysRevD.80.052002.

[24] Christoph Iselin. *The mad program.* In Winfried Busse and Roman Zelazny, editors, *Computing in Accelerator Design and Operation*, volume 215 of *Lecture Notes in Physics*, pages 146–151. Springer Berlin - Heidelberg, 1984. ISBN 978-3-540-13909-6.

[25] I. Agapov, G. A. Blair, S. Malton et al. *BDSIM: A particle tracking code for accelerator beam-line simulations including particle-matter inter-*

*actions*. Nucl. Instrum. Meth., A606:708–712, 2009. doi:10.1016/j.nima.2009.04.040.

[26] J. Carter, I. Agapov, G. A. Blair et al. *International linear collider simulations using bdsim*. Pramana-Journal of Physics, 69(6):1133–1136, 2007. ISSN 0304-4289.

[27] A. Courau. *A fast monte carlo generator for $e^+e^- \to e^+e^-x$ untagged experiments*. SLAC Pubblications, 3363, 1984. SLAC-PUB-3363.

[28] S. Uehara. *Treps: A monte-carlo event generator for two-photon processes at $e^+e^-$ colliders using an equivalent photon approximation*. KEK Report, 96-11, July 1996.

[29] Giovanni Balossini, Carlo M. Carloni Calame, Guido Montagna et al. *Matching perturbative and parton shower corrections to bhabha process at flavour factories*. Nuclear Physics B, 758(1-2):227 – 253, 2006. ISSN 0550-3213. doi:10.1016/j.nuclphysb.2006.09.022.

[30] G. Balossini, C. Bignamini, C.M. Carloni Calame et al. *Photon pair production at flavour factories with per mille accuracy*. Physics Letters B, 663(3):209 – 213, 2008. ISSN 0370-2693. doi:10.1016/j.physletb.2008.04.007.

[31] C.M. Carloni Calame. *An improved parton shower algorithm in qed*. Physics Letters B, 520(1-2):16 – 24, 2001. ISSN 0370-2693. doi:10.1016/S0370-2693(01)01108-X.

[32] C.M. Carloni Calame, C. Lunardini, G. Montagna et al. *Large-angle bhabha scattering and luminosity at flavour factories*. Nuclear Physics B, 584(1-2):459 – 479, 2000. ISSN 0550-3213. doi:10.1016/S0550-3213(00)00356-4.

[33] C.M. Carloni Calame, G. Montagna, O. Nicrosini et al. *The babayaga event generator*. Nuclear Physics B - Proceedings Supplements, 131(0):48 – 55, 2004. ISSN 0920-5632. doi:10.1016/j.

nuclphysbps.2004.02.008. SIGHADO3 Proceedings of the Workshop on Hadronic Cross Section at Low Energy.

[34] VMEbus International Trade Association. *American National Standard for VME64*, volume ANSI/VITA 1-1994 (R2002). American National Standard Institute, Approved 1994 - Reaffirmed 2002.

[35] VMEbus International Trade Association. *American National Standard for VME64 Extensions*, volume ANSI/VITA 1.1-1998. American National Standard Institute, 1998.

[36] Ronald Nutt. *Digital time intervalometer*. 39(9):1342–1345, 1968. ISSN 00346748. doi:DOI:10.1063/1.1683667.